Sede Amministrativa: Università degli Studi di Padova

Dipartimento di Ingegneria Industriale

SCUOLA DI DOTTORATO DI RICERCA IN: Scienze Tecnologie e Misure Spaziali

INDIRIZZO: Scienze e Tecnologie per Applicazioni Satellitari e Aeronautiche

CICLO XXVII

Structural Reliability Analysis of Complex Systems: Applications to Offshore and Composite Structures

Direttore della Scuola: Ch.mo Prof. Giampiero Naletto

Coordinatore d'indirizzo: Ch.mo Prof. Giampiero Naletto

Supervisore: Ch.mo Prof. Ugo Galvanetto

Dottorando: Marco Nicolò Coccon

Summary

This thesis aims at developing new methodologies for the reliability analysis of structural systems with applications to offshore and aeronautical fields. In general, sructures of practical interest are complex redundant systems, in which more than one element is required to fail in order to have catastrophic failure. Moreover, ramdomness inherently exists in both material properties and external loads. As a result, complex structural systems are typically characterised by a huge number of possible failure sequences, of which only some are most likely to occour. Therefore, for an efficient risk analysis, only the dominant failure modes need to be considered, so as to minimise the number of failure paths as well as the computational costs associated to their enumeration and evaluation. However, although several techniques have been developed for the identification of the critical failure sequences, these methods are still either time-demanding or prone to miss potential failure modes.

These challenges motivated the first part of the thesis, in which the merits of a risk assessment framework recently developed for truss and frame structures are here investigated in view of its extensive application to the offshore field. To this end, the case study of a jacket-type platform under an extreme sea state is considered. First, the dominant failure modes of the structure are rapidly identified by a multi-point parallel search employing a genetic algorithm. Then, a multi-scale system reliability analysis is performed, in which the statistical dependence among both structural elements and failure modes is fully considered through simple matrix operations. Finally, the accuracy and the efficiency of the proposed approach are successfully validated against crude Monte Carlo simulation.

In the second part of the thesis, system reliability theory is applied to the uncertainty quantification of the longitudinal tensile strength of UniDirectional (UD) composites, a structural component very common in aircraft structures. Predictive models for size effects in this class of materials are paramount for scaling small-coupon experimental results to the design of large composite structures. In this respect, a Monte Carlo progressive failure analysis is proposed to calculate the strength distributions of hierarchical fibre bundles, which are formed by grouping a predefined number of smaller-order bundles into a larger-order one. The present approach is firstly validated against a recent analytical model to be later applied to more complex load-sharing configurations. The resulting distributions are finally used to analyse the damage accumulation process and the formation of clusters of broken fibres during progressive failure.

Sommario

Lo scopo principale di questa tesi è lo sviluppo di nuove metodologie per determinare l'affidabilità dei sistemi strutturali con applicazioni sia in campo offshore che aeronautico. In generale, strutture di interesse pratico sono caratterizzate da un elevato grado di ridondanza, per cui il collasso globale richiede la rottura simulatanea e/o progressiva di più elementi. Inoltre, i sistemi fisici sono influenzati da diverse fonti di incertezza, quali le prorietà dei materiali e le condizioni ambientali e operative. Pertanto, il collasso strutturale può avvenire con diverse modalità (modi di guasto), di cui solo alcune possiedono una probabilità di accadimento significativa (modi di guasto dominanti). Per una valutazione efficiente del rischio risulta dunque indispensabile limitare l'analisi ai soli modi dominanti, così da ridurre il costo computazionale associato alle fasi di identificazione e di valutazione dei modi stessi. Tuttavia, nonostante in letteratura vi siano numerose soluzioni per l'analisi del rischio, tali metodi richiedono ancora tempi di calcolo notevoli e sono inclini a tralasciare potenziali modi di guasto.

Queste motivazioni conducono alla prima parte delle tesi, in cui si ripropone un metodo recentemente sviluppato per l'analisi del rischio di strutture discrete (reticolari e telai) in previsione di una sua applicazione al campo offshore. A tale scopo si considera il caso di studio di una piattaforma di tipo jacket in condizioni di mare estremo. Dapprima, i modi di guasto dominanti vengono rapidamente identificati per mezzo di un algoritmo genetico. In seguito, l'affidabilità del sistema viene calcolata mediante un approccio multi-scala che fa uso di semplici operazioni matriciali, in cui la dipendenza statistica viene considerata sia tra le componenti strutturali che tra i modi di guasto dominanti. Infine, l'accuratezza e l'efficienza del metodo vengono testate con successo tramite comparazione con Monte Carlo.

Nella seconda parte della tesi, la teoria dell'affidabilità dei sistemi viene applicata per la quantificazione dell'incertezza nella resistenza a trazione di compositi UniDirezionali (UD), problema di notevole interesse per l'ambito aeronautico e non solo. Infatti, il comportamento aletorio di questi materiali è fortemente influenzato da effetti di scala, che limitano la progettazione di strutture in composito di grandi dimensioni sulla base dei dati sperimentali ricavati da provini. In quest'ottica, si propone di modellare fasci di fibre secondo una legge di scala gerarchica, ossia raggruppando un numero prestabilito di fasci più piccoli in un fascio di ordine superiore. La distribuzione di resistenza di tali fasci viene quindi simulata attraverso un'analisi di collasso progressivo. Questo approccio, dapprima validato rispetto ad un modello analitico recentemente sviluppato per disposizioni semplici di fasci, viene poi esteso a configurazioni più realistiche. I risultati così ottenuti sono infine processati per l'analisi statistica del danno.

Acknowledgements

The research work in this thesis was mainly supported by EnginSoft S.p.A under a cooperative agreement with the University of Padova (protocol number 42035, 09 Aug 2011). Additional support was provided by Fondazione Ing. Aldo Gini and by the Italian Ministry of Education, University and Research (MIUR) by the PRIN program 2010/11N.2010MBJK5B.

Firstly, I wish to express my sincere gratitude to my supervisor, Professor Ugo Galvanetto. Since I started my Ph.D., he has given me passionate advice, continuous support and encouragement. I am indebted to him for giving me the extraordinary opportunity to develop my research at the University of Illinois at Urbana-Champaign and at Imperial College London. Such experiences have been paramount in my professional and personal growth, and I believe it was one of the best decisions of my life to join Professor Galvanetto's research group as a doctoral student.

I would like to thank Professor Junho Song for giving me the possibility to work in the Department of Civil and Environmental Engineering at the University of Illinois at Urbana-Champaign. I have learned so many things from him, and his guidance has been invaluable in completing my research. I hope that we will be working on a joint project again.

Similarly, I would like to thank Dr. Soraia Pimenta for giving me the possibility to work in the Department of Mechanical Engineering at Imperial College London. She has been the perfect role model as a researcher, teacher, and person. I am also grateful to her for always pushing me and giving me the critiques and the instructions I needed to make this work something I am proud of.

I would also like to thank the former and current members of Professor Song's Structural System Reliability Group, Junho Chun, Nolan Kurtz, and Derya Deniz, as well as the members of Dr. Pimenta's research group, Gianmaria Bullegas, Cihan Kaboglu, and Gael Grail. It was my great pleasure to share this time and have research discussions with them.

For all the moments of leisure and relaxation during the everyday difficulties of a Ph.D. life, I would like to thank my officemates of "Room-308", Tasnuva, Sherry, Farnaz, Tom, Mitesh, James, Rodolfo, Christos, and, last but not least, my friend Michele. I would also like to thank my colleagues from "CISAS", Marco Thiene, Marco Menegozzo, Teo, Daniele, Giulia, Arman, Siamak, and Lorenzo. To those I may have forgotten to mention, it is pure lack of memory, and I send a great thank you to all of them.

A special thanks goes to Louis and Hannah for their great friendship. During my stay at Urbana-Champaign, they have been like a second family to me. I will always remember the happy moments we spent together with their adorable child, Johan.

I owe my loving thanks to my girlfriend Marta. She has been my world for nearly half of my life, filling my days and supporting me throughout all the ups and downs during my studies.

Finally, my deepest gratitude goes to my parents Francesco and Paola, who have devoted their life to my sister Isabella and me. There are simply no words to express my appreciation for all the love and support they have given us, and that I would never be able to repay. To them I dedicate this thesis.

Table of contents

List of figures

List of tables

1 Introduction

1.1 Motivation and scope of this thesis

Since the late 1960s, structural reliability theory has been extensively applied to the analysis, design and maintenance of structural systems in civil, nuclear, offshore and aerospace fields (Frangopol & Maute, 2003; Haldar, 2006; Moan, 1994, 2005; Thoft-Cristensen, 1998). In particular, most of the reliability applications have been primarily aimed at developing limit state design formats, e.g., the North American codes for steel structures (AISC), movable highway bridges (AASHTO), and offshore platforms (API RP2A). Such specifications are mainly component-based with the underlying hypothesis that a structural system will be safe as long as all its members are safe according to the corresponding limit state equations. Hence, most research has been focusing on component reliability analysis over the years, where a single limit state function is used to describe the failure event of interest (e.g., overload, buckling or fatigue failure of a member). As a consequence, ensuring pre-established target reliabilities to structural components became a part of everyday common practice, but the calculation of the probability of a system-level failure (e.g., sequence of member failures leading to structural collapse) still poses very difficult theoretical and practical challenges.

However, it has been increasingly recognized over the last few decades that system reliability analysis is a matter of primary importance in the field of structural engineering. First of all, it should be noted that the overall reliability of real structures is typically different from the calibrated component reliabilities provided by present day design codes. In fact, structures of practical interest are generally complex redundant systems, in which more than one element is required to fail in order to have system-level failure. This is due to the residual strength provided by non-failed elements, which resist the external loads by redistribution of the internal load effects. Some effort has been made in present day design codes to account for such system reserve strength. For instance, a simplified system approach has been developed by the Joint Industry Project (JIP) (Bomel Ltd., 2002) to derive environmental load factors for fixed steel offshore structures. Here, the calibration process is carried out on a global failure function defined by the difference between the structural reserve strength and the environmental load, in which the reserve strength is evaluated by deterministic

progressive failure analyses. Nevertheless, from a reliability viewpoint this approach is still component-based, since a single limit state equation is involved in the definition of the system failure. In a similar way, a single-function event is often used to model the system failure of offshore structures under extreme sea loading, where both the load and resistance terms in the limit state equation are referred to as the overall base shear. Although this approach is computationally efficient and particularly attractive for planning of inspection, maintenance and repair strategies (Ayala-Uraga & Moan, 2002), it has been validated only for cases where the load uncertainties are dominant and the resulting stresses in the components are highly correlated (Wu & Moan, 1989). Such an assumption may not be true, as in the case of fatigue failure, where the uncertainties related to resistance properties are higher and the correlation among components is lower. Thus, it is clear that a more general and rigorous risk assessment framework employing system-based reliability analysis is needed, in which the reliability of a structural system is estimated with respect to all its potential (or dominant) failure modes and their statistical dependence.

In general, complex structural systems are characterised by a huge number of critical sequences of component failures leading to a system failure, of which only some (i.e., the dominant failure modes) are most likely to contribute to the overall failure. Therefore, for an efficient risk analysis, only the dominant failure modes need to be considered so as to minimise the number of failure paths as well as the computational costs associated to their enumeration and evaluation. Although several techniques have been developed for the identification of the critical failure sequences (see review from Karamchandani, Dalane & Bjerager, 1992), these methods are still either time-demanding or likely to miss potential failure modes. In the latter case, the risk is underestimated due to heuristic rules that are often introduced to improve the efficiency of the enumeration process. Concerning the evaluation of the system failure probability, various approximate techniques have been proposed such as the first-order system reliability method (Hohenbichler & Rackwitz, 1983) that applies component reliability analyses to series and parallel systems directly, while it involves theoretical bounding formulas (Ditlevsen, 1979) in the case of more complex systems. These approaches are not flexible in incorporating various types and amount of available information on components and their statistical dependence (Song & Kang, 2009). Moreover, the complexity of a system event complicates the reliability computations and may require overwhelming time costs.

These challenges motivated the first part of the present research, which aims to investigate and develop new methodologies for the system reliability analysis of offshore structures. A powerful risk assessment methodology has been recently developed for truss and frame structures (Kim et al., 2013; Kurtz et al., 2010). Differently from standard probabilistic approaches (Karamchandani, 1987; Lee & Song 2011, 2012; Murotsu et al., 1984; Thoft-Christensen & Murotsu, 1986), the proposed method offers the main advantage that the identification process of dominant failure modes is decoupled from the evaluation process of their probabilities. In this way, the approach avoids performing reliability analyses repeatedly

during the identification process, which otherwise may lead to huge computational costs especially for large and highly-redundant structures. Here, the dominant failure modes are rapidly identified in the decreasing order of their likelihood by means of a multi-point parallel search employing a genetic algorithm. Once the identification phase is completed, the system failure probability is evaluated by a multi-scale analysis employing the matrix-based system reliability method (MSR) (Kang et al., 2012; Kang, Song & Gardoni, 2008; Lee et al., 2011; Nguyen, Song & Paulino, 2010, 2011; Song and Kang 2009; Song and Ok, 2010), which has been recently developed for accurate and efficient system reliability analysis through simple matrix operations.

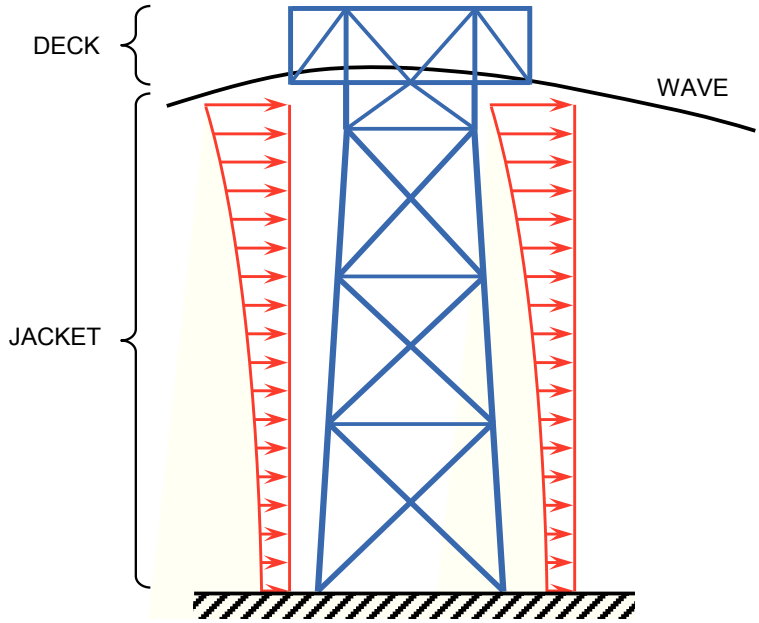

Figure 1.1: Jacket-type platform under an extreme sea loading.

In order to investigate the applicability of the proposed method to the risk assessment of offshore structures, the case study of a jacket-type platform under an extreme sea loading is considered (see Figure 1.1). Following the procedure adopted in (Thoft-Christensen & Murotsu, 1986), the probabilistic model of the extreme sea loading is derived from a short-term design storm, in which uncertainties are assumed both in the wave model (i.e., in the wave height and the current speed) and the hydrodynamic model (i.e., in the drag and mass coefficients of the tubular members). The structure is analysed as a truss and a further source of uncertainty affects the yield stress of the members, which are assumed to fail either in tension or compression. Nonlinearities on the structural response are mainly due to the top side of the structure (the deck), which causes a sharp increase in wave-current forces as soon as the wave height exceeds a certain value. Further nonlinear contributions arise from the hydrodynamic model and the post-failure behaviour of the members, which is assumed purely ductile in tension and brittle-ductile in compression. In particular, the effect of the post-buckling factor on the redundancy of the structure is also investigated.

In the second part of this thesis, system reliability theory is applied to the uncertainty quantification of the longitudinal tensile strength of UniDirectional (UD) composites, a structural component very common in aircraft structures. The damage accumulation and failure of this class of materials is governed by statistical size effects, which pose a challenge to use coupon-based experimental data for the design of large structures. Although most authors agree that the statistics of fibre strength are essential for establishing the relationship between composite longitudinal tensile strength and size effects, a widely accepted strategy for the stochastic analysis of Fibre-Reinforced Polymers (FRPs) is still to be developed (Wisnom, 1999).

Pimenta and Pinho (2013) recently proposed a hierarchical scaling law for the strength of composite fibre bundles, which has been extensively validated against experimental results and predicts full strength distributions for bundles of any size. As illustrated in Figure 1.2a, the model assumes that hierarchical bundles are formed by grouping two smaller-order bundles into a larger-order bundle (i.e., a coordination number $c = 2$ is used). Once a sub-bundle fails, stresses are recovered according to a plastic shear-lag model, so that linear stress concentrations apply in the surrounding intact sub-bundle. Although this approach leads to an efficient computation of bundle strength distributions, imposing a coordination number equal to two results in very high stress concentrations in the proximity of fibre breaks.

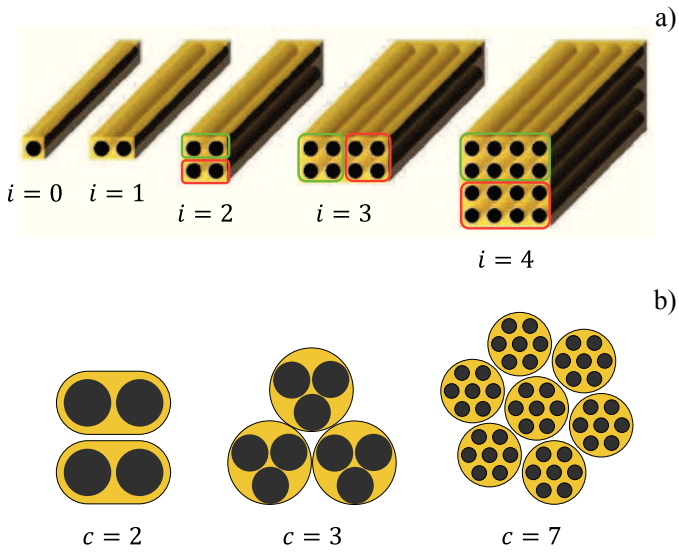

Figure 1.2: a) First 4 bundle levels with coordination number $c = 2$; b) Fibre arrangements for different coordination numbers.

The objective of the present work is therefore to extend Pimenta and Pinho's (2013) model to more realistic load-sharing configurations, generalising the hierarchical approach to higher coordination numbers (Figure 1.2b) and, consequently, reducing stress concentration factors in the neighbourhood of fibre breaks. However, at higher coordination numbers, the increasing number of possible sequences of failure events in a bundle complicates the

analytical evaluation of its strength distribution and, thus, a new numerical approach is needed. In this work, a Monte Carlo progressive failure analysis is proposed to calculate the bundle strength distributions, where the failure events are simulated through a discrete representation of hierarchical bundles. The damage accumulation into clusters of fibre breaks is also investigated.

1.2 Outline of this thesis

This thesis is divided into five chapters, which can be summarised as follows:

- Chapter 2 serves as an introduction to the system reliability theory. The probabilistic concept of reliability is first introduced at the component level. First, a closed-form solution is derived for the failure probability associated to linear limit state functions and normal random variables. Second, the general case of non-linear limit state functions and arbitrary distributions is addressed by means of approximate techniques, such as first- and second-order reliability methods (FORM and SORM), and Monte Carlo simulation (MCS). Lastly, the concept of reliability is extended to the system level, providing the basic mathematical tools for the applications in Chapters 3 and 4.

- Chapter 3 proposes a novel strategy for the risk assessment of offshore structures. The genetic algorithm developed by Kim et al. (2013) is here combined with the MSR method (Song & Kang, 2009) and applied to the analysis of a jacket platform under an extreme sea state. First, the structural model and the loading conditions are derived, providing the input random variables for the multi-point parallel search. Second, the main steps of the failure mode identification process are summarised, followed by a detailed explanation of the MSR method. Lastly, results and discussion are presented, and the main conclusions are drawn.

- Chapter 4 proposes a numerical approach to model size effects on the stochastic longitudinal tensile strength of composite fibre bundles. First, the hierarchical scaling law developed by Pimenta and Pinho (2013) is briefly introduced. Second, a Monte Carlo progressive failure analysis is implemented extending the analysis to more realistic load-sharing configurations. Lastly, results are verified against the hierarchical scaling law, pros and cons of the present method are discussed, and the main conclusions are finally drawn.

- Chapter 5 summarises the major findings of this work and presents possible related future research topics.

2 Structural reliability theory

The main aim of this chapter is to provide the necessary background on the system reliability theory as well as on the numerical methods that are at the base of the present work. In Section 2.1, the probabilistic concept of reliability is introduced at the *component* level. Here, the safe state of a structural element (or system) is expressed by a single functional relationship between a vector of input random variables and a design performance (such as the maximum stress or displacement). First, a closed-form solution for the probability of failure is presented for the simple case of normally distributed random variables and linear performance function. Then, approximate techniques for the general case of arbitrary distributions and non-linear performance function are discussed, and particular attention is focused on first-order approaches. Furthermore, a brief introduction to second-order approaches and Monte Carlo simulation is presented, and their accuracy and efficiency are investigated through a simple example. Finally, in Section 2.2, the reliability problem is extended to the *system* level, where the failure event is defined by a logical function consisting of multiple component events, each one expressing the failure of a structural member or the occurrence of a failure mode.

2.1 Component reliability analysis

2.1.1 Fundamental concepts of reliability theory

Reliability-based analyses can be used in different applications, such as code checking for structural design, uncertainty analysis and design optimisation. In all these contexts, the common thread is represented by the need to evaluate the *performance function,* $Y = g(\boldsymbol{X})$, which specifies the relationship between a performance Y and the input variables $\boldsymbol{X} = (X_1, X_2, \dots, X_n)$. Generally, the performance function is defined such that

$$\begin{aligned} \{\boldsymbol{X} \in \mathbb{R}^n \mid g(\boldsymbol{X}) > 0\} &= \text{safe region} \\ \{\boldsymbol{X} \in \mathbb{R}^n \mid g(\boldsymbol{X}) \leq 0\} &= \text{failure region} \end{aligned} \tag{2.1}$$

In other words, a threshold equal to zero is chosen as the limit state: when the performance reaches this value, the state of the structural system or component switches from safety to failure.

Within the framework of the reliability theory, $\boldsymbol{X}$ is defined by a random vector containing the uncertain input quantities, such as material properties, geometry, and both load and environmental conditions. Thus, even the performance Y is a random variable, and the probability that its value reaches the limit state is called *probability of failure*, i.e.

$$P_f = P[g(\boldsymbol{X}) \leq 0] = F_Y(0) = \int_{g(\boldsymbol{X})\leq 0} f_{\boldsymbol{X}}(\boldsymbol{x})\, d\boldsymbol{x} \tag{2.2}$$

where F_Y is the *cumulative distribution function* (CDF) of Y, and $f_{\boldsymbol{X}}$ is the joint *probability density function* (PDF) of $\boldsymbol{X}$. The complement of the probability of failure is called *reliability*, i.e.

$$\mathcal{R} = P[g(\boldsymbol{X}) > 0] = 1 - P_f \tag{2.3}$$

Now, refer to the performance function $g(\cdot)$ as the difference between the strength R of a structural component and the load effect S acting on the member itself, i.e. $g(\boldsymbol{X}) = R - S$, being $\boldsymbol{X} = (R, S)$. If all the random variables are independent,

$$f_{\boldsymbol{X}}(\boldsymbol{x}) = \prod_{i=1}^{n} f_{X_i}(x_i) \implies f_{R,S}(r,s) = f_R(r) f_S(s) \tag{2.4}$$

where $f_{R,S}$ is the joint PDF of R and S, and f_R and f_S are their marginal PDFs, respectively. The following well known expression for the probability of failure is then derived,

$$P_f = \iint_{R-S\leq 0} f_R(r) f_S(s) dr ds = \int_0^{\infty} \left[\int_0^{s} f_R(r) dr\right] f_S(s)\, ds = \int_0^{\infty} F_R(s) f_S(s) ds \tag{2.5}$$

In this case, P_f is given by the convolution integral between f_S and the CDF of R, i.e. F_R. The geometrical interpretation of this formula is shown in Figure 2.1.

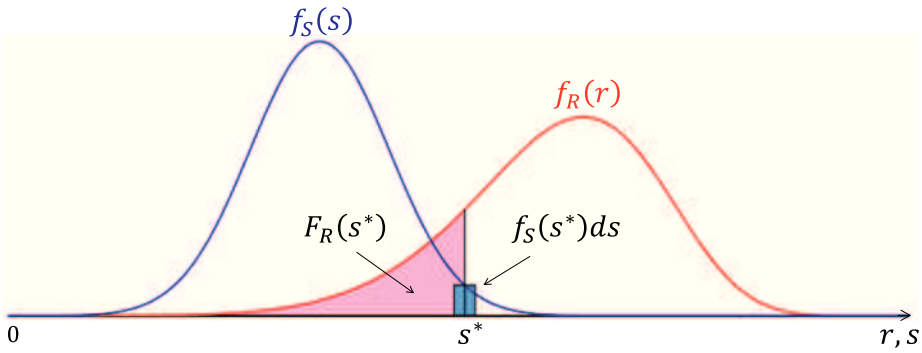

Figure 2.1: Geometrical interpretation of the convolution integral in Eq. (2.5).

The red area under the left tail of f_R is the probability that R is less than $S = s^*$, i.e. $F_R(s^*) = P(R \leq s^*)$; and the blue rectangle is the probability that S is equal to s^*, i.e. $f_S(s^*)ds = P(S = s^*)$. Therefore, the probability of the failure event relative to $S = s^*$ is simply given by the product of the two terms above. Finally, the total failure probability, P_f, is the sum of the event failure probabilities associated to all the possible outcomes of S, i.e.

$$\int_0^\infty F_R(s) f_S(s) ds = \sum_{s_i=0}^{\infty} P(R \leq s_i) P(S = s_i) \tag{2.6}$$

It should be noted that Eqs. (2.5) and (2.6) are only valid in the case of statistical independence between R and S. Indeed, the right-hand side of Eq. (2.6) is a particular case of the total probability theorem (Zwillinger & Kokoska, 2000), which will prove very useful in the next chapter. The theorem states that if the events B_i $(i = 1, 2, \dots, n)$ are mutually exclusive and collectively exhaustive, and each event B_i is measurable, then for any event A is

$$P(A) = \sum_{i=1}^{n} P(A|B_i) P(B_i) \tag{2.7}$$

where $P(A|B_i)$ is the conditional probability of A given B_i. The analogy with the previous case can be found by letting $B_i = (S = s_i)$ and $A = (Y \leq 0)$, where $Y = R - S$. Thus,

$$P_f = F_Y(0) = \sum_{s_i=0}^{\infty} F_Y(0|s_i) P(S = s_i) = \int_0^\infty F_Y(0|s) f_S(s) ds \tag{2.8}$$

where $F_Y(0|s) = P(R - S \leq 0 | S = s)$ is equal to $F_R(s)$ if R and S are independent. In this case, Eq. (2.8) reduces to the convolution integral in Eq. (2.5).

The general situation with statistical dependence between R and S is illustrated in Figure 2.2, which shows the joint PDF $f_{R,S}(r, s)$ and the failure domain $g(R, S) \leq 0$. The

missing volume of the joint PDF cut by the negative region represents the probability of failure, P_f, which is quantified by the integral in Eq. (2.2). However, the number of random variables in many engineering applications is usually high. Thus, both the performance function $g(\boldsymbol{X})$ and the joint PDF $f_{\boldsymbol{X}}$ are defined in a hyperspace, where the evaluation of P_f may become a very computationally expensive task. The geometry is further complicated when the integration boundary $g(\boldsymbol{X}) = 0$ is a nonlinear function of $\boldsymbol{X}$. Finally, the exact expression of $g(\boldsymbol{X})$ may not be known as it often comes with the output of complex FE analyses.

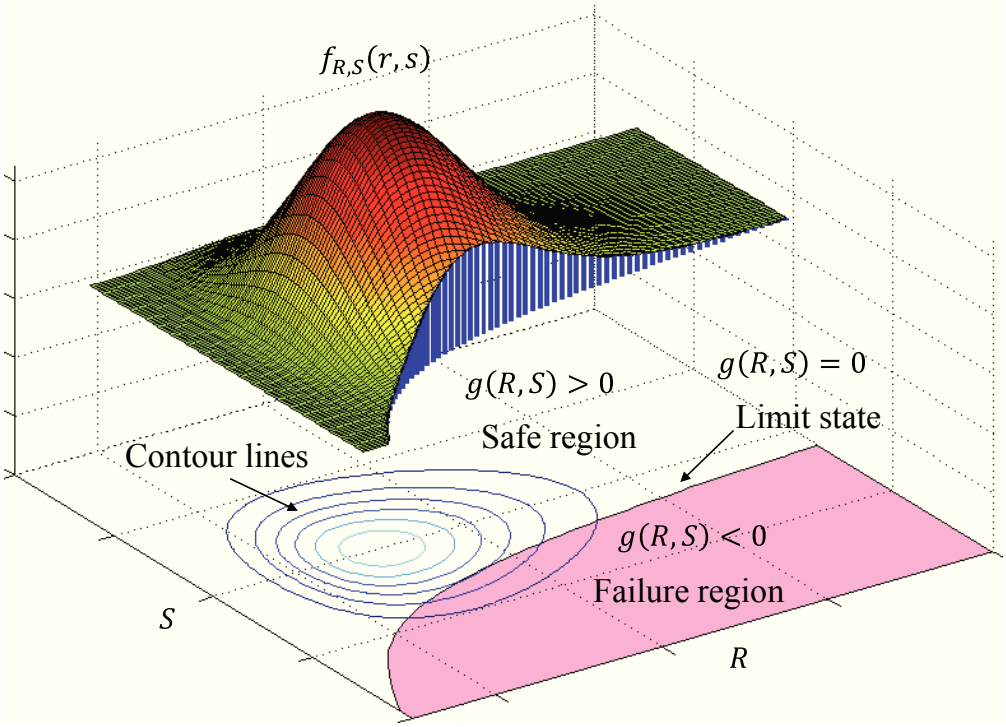

Figure 2.2: Geometrical interpretation of the probability of failure for a 2D problem (Du, 2015).

Because of the difficulties mentioned above, analytical solutions to the integral in Eq. (2.2) are only limited to very special cases. For this reason, starting from the seventies many authors proposed an alternative way to look at the reliability problem. The main idea was to avoid the direct integration in Eq. (2.2) and, instead, to calculate the distance from the failure region to the mean value of the random vector $\boldsymbol{X}$. Such a distance is called *reliability index*, and it is indicated with β (Ditlevsen & Madsen, 2007). As the name suggests, a higher β corresponds to a more reliable system (or component). Indeed, a higher value of β means that the failure region is closer to the tail of $f_{\boldsymbol{X}}(\boldsymbol{x})$, where the subtended volume is smaller. This concept is further developed in the next section, which illustrates a very special case admitting exact analytical solution.

2.1.2 Closed-form solution of the probability integral

Consider the performance function $g(R,S) = R - S$, where R and S are independent normal random variables, being μ_R, μ_S the means and σ_R, σ_S the standard deviations. The following transformation can be introduced,

$$U_1 = \frac{R - \mu_R}{\sigma_R} \quad , \qquad U_2 = \frac{S - \mu_S}{\sigma_S} \tag{2.9}$$

which maps the mean vector (μ_R, μ_S) into the origin of the independent standard normal variable space (U_1, U_2). By transforming $g(R,S)$ into $g(U_1, U_2)$, it is found that

$$g(R,S) = R - S \iff g(U_1, U_2) = \sigma_R U_1 - \sigma_S U_2 + \mu_R - \mu_S \tag{2.10}$$

As shown in Figure 2.3, the limit state equation $g(U_1, U_2) = 0$ is the expression of a line in the space (U_1, U_2), whose distance from the origin provides the analytical expression of the reliability index β,

$$\beta = \frac{\mu_R - \mu_s}{\sqrt{{\sigma_R}^2 + {\sigma_S}^2}} \tag{2.11}$$

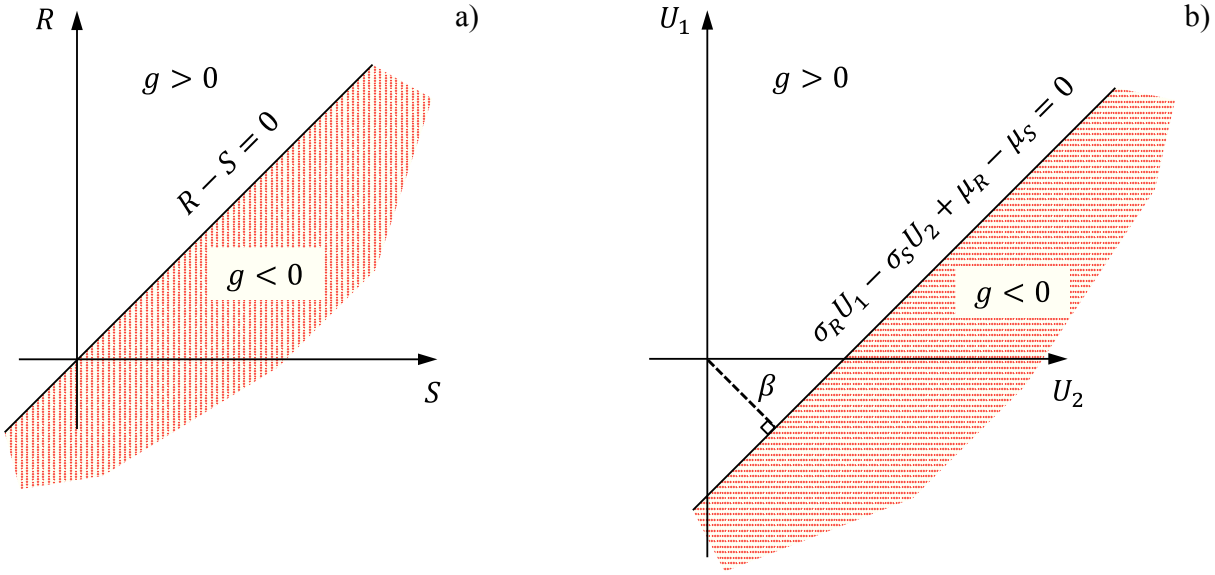

Figure 2.3: Limit state equation and failure domain before (a) and after (b) transformation.

In order to further investigate the meaning of the index β, let Y be a linear combination of the random variables $\boldsymbol{X} = (X_1, X_2, \dots, X_n)$, such that $Y = \boldsymbol{a}^T \boldsymbol{X} + b$. The mean μ_Y and the standard deviation σ_Y of Y are calculated as follows,

$$\mu_Y = E[Y] = \boldsymbol{a}^T \boldsymbol{\mu_X} + b \tag{2.12}$$

$$\sigma_Y^2 = E[(Y - \mu_Y)^2] = \boldsymbol{a}^T \sum_{\boldsymbol{X}} \boldsymbol{a} \tag{2.13}$$

where $E[\cdot]$ is the expectation operator (Sheldon, 2007), and $\boldsymbol{\mu_X} = \left(\mu_{X_1}, \mu_{X_2}, \dots, \mu_{X_n}\right)^T$ and $\sum_{\boldsymbol{X}}$ are the mean vector and the covariance matrix of $\boldsymbol{X}$ respectively. By applying these rules to Eq. (2.10), the reliability index in Eq. (2.11) can be rewritten as

$$\beta = \frac{\mu_g}{\sigma_g} \tag{2.14}$$

Both Eqs. (2.11) and (2.14) are true under the following hypotheses:

i) the failure surface $g(\boldsymbol{X}) = 0$ is a linear function of $\boldsymbol{X}$;

ii) the random vector $\boldsymbol{X}$ is normally distributed.

Under such circumstances, the reliability index β can also be interpreted as the number of standard deviations σ_g that the mean value μ_g of the performance function falls in the safe region $g(R,S) > 0$ (i.e., $\mu_g = \beta\sigma_g$, as shown in Figure 2.4).

Furthermore, since any linear combination of a normal random vector $\boldsymbol{X}$ is normally distributed, hypotheses *i)* and *ii)* also imply $g(\boldsymbol{X})$ to be normally distributed, so that

$$P_f = F_g(0) = \Phi\left(\frac{0 - \mu_g}{\sigma_g}\right) = \Phi(-\beta) \tag{2.15}$$

where Φ is the CDF of the standard normal distribution. The identities in Eq. (2.15) are illustrated in Figure 2.4. A one-one relationship is then provided between the probability of failure P_f and the reliability index β,

$$P_f = \Phi(-\beta) \iff \beta = -\Phi^{-1}\left(P_f\right) \tag{2.16}$$

Next, these expressions will be used to estimate the reliability in a general situation where *i)* and *ii)* are not verified, as in the case of non-normal random variables and/or non-linear performance function.

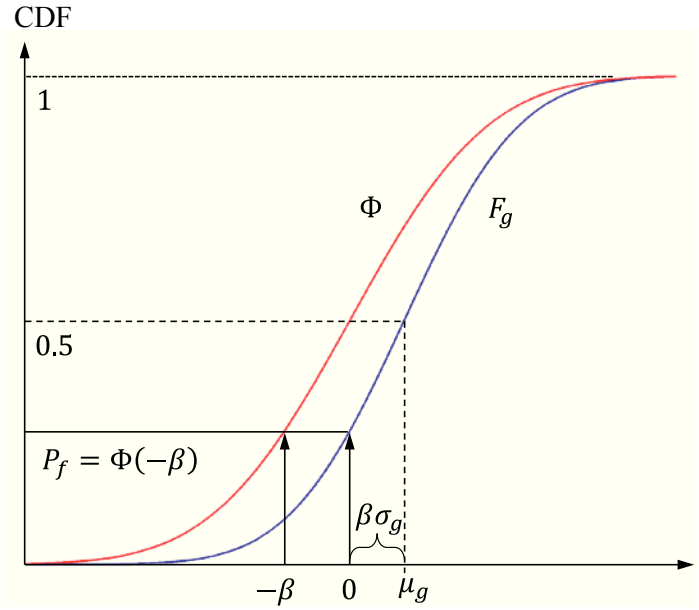

Figure 2.4: Closed-form solution of the probability integral.

2.1.3 Random variable transformations

Consider now the case where $\boldsymbol{X} = (X_1, X_2, \dots, X_n)$ is a vector of non-normal random variables. The reliability problem can be solved through a nonlinear transformation of the joint PDF $f_{\boldsymbol{X}}$ from the original space $\boldsymbol{X}$ to a space of independent standard normal variables $\boldsymbol{U} = (U_1, U_2, \dots, U_n)$, where the contour lines of $f_{\boldsymbol{X}}$ become circular and concentric (Figure 2.5).

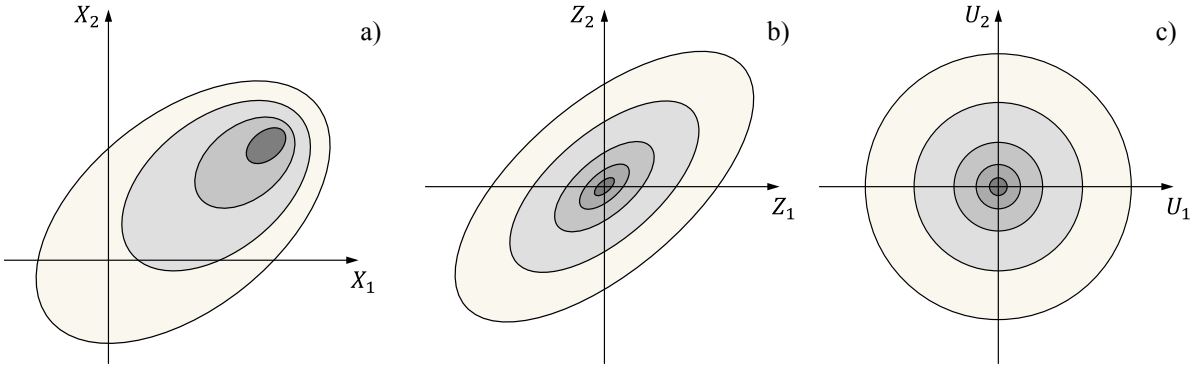

Figure 2.5: Contour lines of a 2D joint PDF $f_{\boldsymbol{X}}$ in the original space $\boldsymbol{X}$ (a), in the correlated standard normal space $\boldsymbol{Z}$ (b), and in the independent standard normal space $\boldsymbol{U}$ (c).

An intermediate step is generally needed, transforming $\boldsymbol{X}$ into a vector of correlated standard normal variables, $\boldsymbol{Z} = (Z_1, Z_2, \dots, Z_n)$. To this end, transformations like Rosenblatt (Rosenblatt, 1952) or Nataf (Der Kiureghian, 2005; Liu & Der Kiureghian, 1986a) are usually performed. This thesis will focus on the latter, which is expressed by

$$z_i = \Phi^{-1}\left[F_{X_i}(x_i)\right], \qquad i = 1, 2, \dots, n \tag{2.17}$$

being F_{X_i} the marginal CDF of X_i. The correlation matrix $R_{\boldsymbol{Z}} = \{\rho_{Zij}\}$ of $\boldsymbol{Z}$ is defined in terms of the correlation matrix $R_{\boldsymbol{X}} = \{\rho_{Xij}\}$ of $\boldsymbol{X}$ through the integral relation

$$\rho_{Xij} = \int_{-\infty}^{\infty}\int_{-\infty}^{\infty}\left(\frac{x_i - \mu_i}{\sigma_i}\right)\left(\frac{x_j - \mu_j}{\sigma_j}\right)\varphi_2(z_i, z_j, \rho_{Zij})dz_i dz_j \tag{2.18}$$

where φ_2 is the 2D standard normal PDF with correlation coefficient ρ_{Zij}. For each pair (X_i, X_j) with known correlation ρ_{Xij}, Eq. (2.18) should be solved to determine correlation ρ_{Zij} between (Z_i, Z_j). In general, 2D numerical Gauss integration is needed, and the number of integration points must be carefully selected in the case of strong correlation (Bourinet, 2010; Bourinet, Mattrand, & Dubourg, 2009). Approximate solutions of Eq. (2.18) are provided in (Liu & Der Kiureghian, 1986a) for most common statistical distributions.

Independent standard normal variables **U** are then obtained from **Z** variables by means of a linear transformation,

$$\boldsymbol{U} = A\boldsymbol{Z} + \boldsymbol{b} \tag{2.19}$$

where matrix A and vector $\boldsymbol{b}$ are determined from Eqs. (2.12) and (2.13) imposing $\boldsymbol{\mu_U} = \boldsymbol{\mu_Z} = \boldsymbol{0}$ (null vector) and $\sum_{\boldsymbol{Z}} = R_{\boldsymbol{Z}}$,

$$\boldsymbol{\mu_U} = A\boldsymbol{\mu_Z} + \boldsymbol{b} \implies \boldsymbol{b} = \boldsymbol{0} \tag{2.20}$$

$$\sum_{\boldsymbol{U}} = AR_{\boldsymbol{Z}}A^T \implies AR_{\boldsymbol{Z}}A^T = I_n \tag{2.21}$$

Eq. (2.21) can then be solved for A using the Cholesky decomposition of R_Z

$$AR_{\boldsymbol{Z}}A^T = A(LL^T)A^T = I_n \implies A = L^{-1} \tag{2.22}$$

where L is a lower triangular matrix. In this way, Eq. (2.19) can be combined with Eq. (2.17) providing the final relation between $\boldsymbol{X}$ and $\boldsymbol{U}$

$$\begin{Bmatrix} u_1 \\ \vdots \\ u_n \end{Bmatrix} = L^{-1}\begin{Bmatrix} \Phi^{-1}\left[F_{X_1}(x_1)\right] \\ \vdots \\ \Phi^{-1}\left[F_{X_n}(x_n)\right] \end{Bmatrix} \tag{2.23}$$

EXAMPLE 2.1

To give an example of variable transformation using Eq. (2.23), the analysis of the previous section is extended to the case of a linear performance function $g(\boldsymbol{X}) = R - S$, where $\boldsymbol{X} = (R, S)$ is a vector of normally distributed and correlated random variables. Then, let the covariance matrix be defined as

$$\sum_{\boldsymbol{X}} = \begin{bmatrix} \sigma_R^2 & \rho\sigma_R\sigma_S \\ \rho\sigma_S\sigma_R & \sigma_S^2 \end{bmatrix} \tag{2.24}$$

where ρ is the correlation coefficient between R and S. For this simple case Eq. (2.18) admits closed-form solution and the following expressions for $R_{\boldsymbol{Z}}$ and L can be found,

$$R_{\boldsymbol{Z}} = \begin{bmatrix} 1 & \rho \\ \rho & 1 \end{bmatrix} \implies L = \begin{bmatrix} 1 & 0 \\ \rho & \sqrt{1-\rho^2} \end{bmatrix} \tag{2.25}$$

Since R and S are normally distributed, Eq. (2.23) reduces to

$$\begin{Bmatrix} u_1 \\ u_2 \end{Bmatrix} = L^{-1} \begin{Bmatrix} (r-\mu_R)/\sigma_R \\ (s-\mu_S)/\sigma_S \end{Bmatrix} \tag{2.26}$$

By transforming $g(R, S)$ into $g(U_1, U_2)$, one gets

$$g(R,S) = R - S \iff g(U_1, U_2) = (\sigma_R - \rho\sigma_S)U_1 - \sqrt{1-\rho^2}\sigma_S U_2 + \mu_R - \mu_S \tag{2.27}$$

whose distance from the origin of the standard normal space is

$$\beta = \frac{\mu_R - \mu_s}{\sqrt{{\sigma_R}^2 + {\sigma_S}^2 - 2\rho\sigma_R\sigma_S}} \tag{2.28}$$

This expression generalises Eq. (2.11) for $\rho \neq 0$. The same result could have been easily found by substituting Eq. (2.24) into Eq. (2.13) so as to provide the expression of σ_g to be used in Eq. (2.14).

2.1.4 Toward an approximate calculation of the reliability index

This Section moves a step closer to the solution of a general reliability problem, where $g(\boldsymbol{X})$ is a nonlinear performance function, and $\boldsymbol{X}$ is a vector of random variables with arbitrary distributions. An approximate evaluation of the reliability index is here obtained in two steps:

Step 1: the performance function $g(\boldsymbol{X})$ is expanded in a Taylor series about the linearisation point $\boldsymbol{x}^*$ and higher order terms are neglected,

$$g(\boldsymbol{X}) \cong g(\boldsymbol{x}^*) + \nabla g^T \cdot (\boldsymbol{X} - \boldsymbol{x}^*) \tag{2.29}$$

where the gradient ∇g is evaluated at $\boldsymbol{x}^*$. Approximate values for μ_g and σ_g are then obtained from Eqs. (2.12) and (2.13),

$$\mu_g \cong g(\boldsymbol{x}^*) + \nabla g^T \cdot (\boldsymbol{\mu_X} - \boldsymbol{x}^*) \tag{2.30}$$

$$\sigma_g^2 \cong \nabla g^T \sum_{\boldsymbol{X}} \nabla g \tag{2.31}$$

Step 2: the vector $\boldsymbol{X}$ is simply treated as a vector of normal random variables (Nataf or Rosenblatt transforms could be used instead, without introducing any further approximation), so that the expressions above can be substituted into Eq. (2.14) to provide an approximate expression of the reliability index,

$$\beta \cong \frac{g(\boldsymbol{x}^*) + \nabla g^T \cdot (\boldsymbol{\mu_X} - \boldsymbol{x}^*)}{\sqrt{\nabla g^T \sum_{\boldsymbol{X}} \nabla g}} \tag{2.32}$$

Clearly, the value of β depends on the choice of the linearization point; in the particular case of $\boldsymbol{x}^* = \boldsymbol{\mu_X}$, Eq. (2.32) only involves the second moment of the input random vector $\boldsymbol{X}$, thus leading to the so called *Mean-Value-First-Order-Second-Moment* (MVFOSM) reliability index (Haldar & Mahadevan, 2000). Despite MVFOSM allows a straightforward evaluation of the reliability, significant error can be introduced by retaining only the linear terms. Furthermore, the value of β is not invariant under different but equivalent formulations of the same performance function.

EXAMPLE 2.2

This concept is here illustrated through the case of an axially loaded tension member, indicating with Y the yield strength, A the cross-sectional area, and F the external axial force. Let Y and A be independent normal variables ($\mu_Y = 100$ MPa, $\sigma_Y = 10$ MPa, $\mu_A = 75\ \text{mm}^2$, $\sigma_A = 5\ \text{mm}^2$), and let F be a deterministic parameter equal to 5000 N. The reliability

problem can then be formulated based on two different performance functions, here referred to as the strength formulation,

$$g_1(Y,A) = YA - F \implies \beta_{MVFOSM} = \frac{\mu_Y \mu_A - F}{\sqrt{\mu_A^2 \sigma_Y^2 + \mu_Y^2 \sigma_A^2}} = 2.774 \tag{2.33}$$

and the stress formulation,

$$g_2(Y,A) = Y - \frac{F}{A} \implies \beta_{MVFOSM} = \frac{\mu_Y \mu_A - F}{\sqrt{\mu_A^2 \sigma_Y^2 + \frac{F^2}{\mu_A^2} \sigma_A^2}} = 3.046 \tag{2.34}$$

Such expressions of $g(Y,A)$ are "mechanically" equivalent in that they lead to the same limit state equation, $g_1(Y,A) = g_2(Y,A) = 0$. This is not true for the linearised performance functions, which depend on what formulation is considered during MVFOSM (see Figure 2.6), thus leading to different estimates of the reliability index (see Eqs. (2.33) and (2.34)).

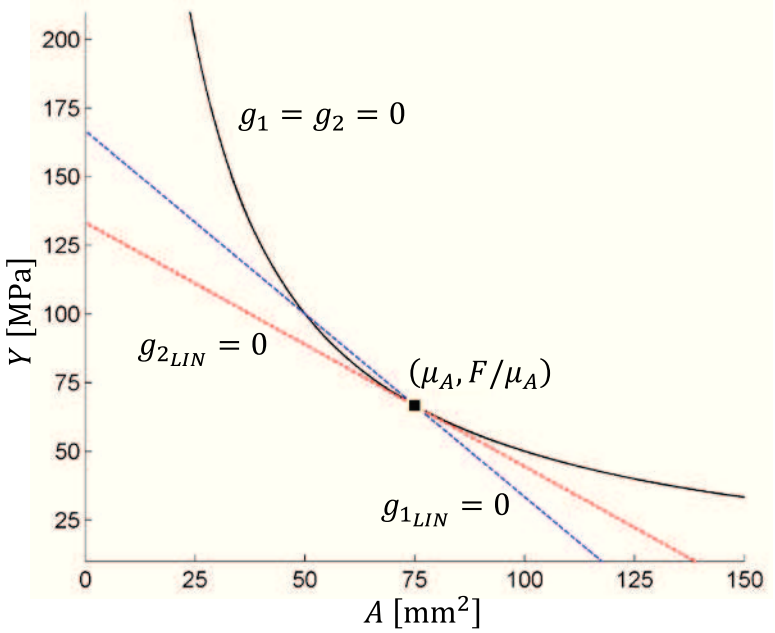

Figure 2.6: Actual limit state equation and linearised limit state equations.

The arbitrariness in the reliability index is circumvented if the linearisation point is chosen within the failure surface $g(\boldsymbol{X}) = 0$, which is invariant to equivalent formulations of the performance function. However, there are infinite points of the limit state that can be used for Taylor expansion, and the right point must be carefully selected, as described in the next section.

2.1.5 First-Order Reliability Method (FORM)

An invariant formulation of the reliability index is provided by the First-Order Reliability Method (FORM), which represents the most common technique of structural reliability analysis. Differently from the approximation methods seen before, the optimal point about which to linearise the failure surface is found in the space of the standard normal variables $\boldsymbol{U}$. In this way, the probability integral in Eq. (2.2) becomes

$$P_f = P[g(\boldsymbol{U}) \leq 0] = \int_{g(\boldsymbol{U})\leq 0} \varphi_n(\boldsymbol{u}; I_n)\, d\boldsymbol{u} \tag{2.35}$$

where $\varphi_n(\cdot)$ is the joint PDF of $\boldsymbol{U}$, whose contour lines have been shown in Figure 2.5c for the 2D problem. The expression for a multivariate normal PDF with zero mean and identity covariance matrix I_n is given by

$$\varphi_n(\boldsymbol{u}; I_n) = \frac{1}{\sqrt{2\pi}} exp\left(-\frac{1}{2}\sum_{i=1}^{n} u_i^2\right) \tag{2.36}$$

The optimal point for the linearization of the failure surface $g(\boldsymbol{U}) = 0$ has to be searched among the points with the highest contribution to the probability integral in Eq. 2.35. This is equivalent to finding the point of $g(\boldsymbol{U}) = 0$ with the minimum norm $\|\boldsymbol{u}\| = \sum_{i=1}^{n} u_i^2$ (corresponding to highest value of the integrand φ_n),

$$\begin{cases} \min\limits_{\boldsymbol{u}} \|\boldsymbol{u}\| \\ \text{subject to } g(\boldsymbol{U}) = 0 \end{cases} \tag{2.37}$$

The solution of this optimization problem goes under the name of *most probable point* (MPP) and it is indicated by $\boldsymbol{u}^* = (u_1^*, u_2^*, \cdots, u_n^*)$. As illustrated in Figure 2.7 and Figure 2.8, the MPP is the shortest distance point from the failure surface $g(\boldsymbol{U}) = 0$ to the origin of the standard normal space. Such a distance leads to the so-called Hasofer-Lind reliability index (Hasofer & Lind, 1974), which is denoted by $\beta_{HL} = \|\boldsymbol{u}^*\|$ (it is worth noticing that the closed-form solutions in Eq.s (2.11) and (2.28) are special cases of the Hasofer-Lind reliability index).

The failure surface $g(\boldsymbol{U}) = 0$ is then expanded in a Taylor series about the linearisation point $\boldsymbol{u}^*$ defined by the MPP,

$$g(\boldsymbol{U}) \cong g(\boldsymbol{u}^*) + \nabla g^T \cdot (\boldsymbol{U} - \boldsymbol{u}^*) \tag{2.38}$$

where the gradient ∇g is evaluated at $\boldsymbol{u}^*$. Analogously to the procedure reported in the previous section, the following expression of the reliability index is recovered,

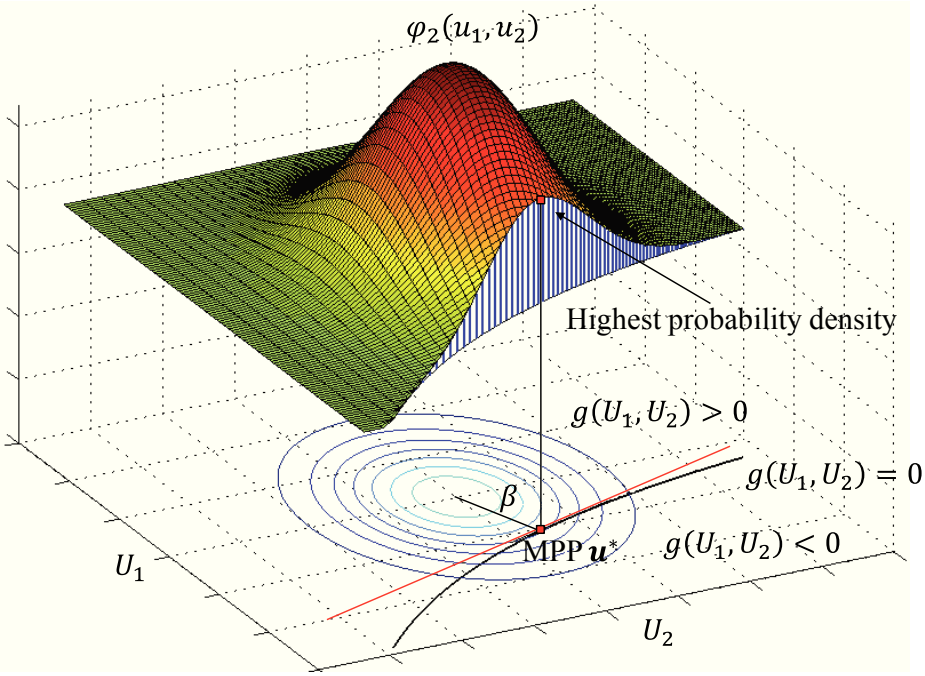

Figure 2.7: Highest value of the joint PDF at the MPP (Du, 2015).

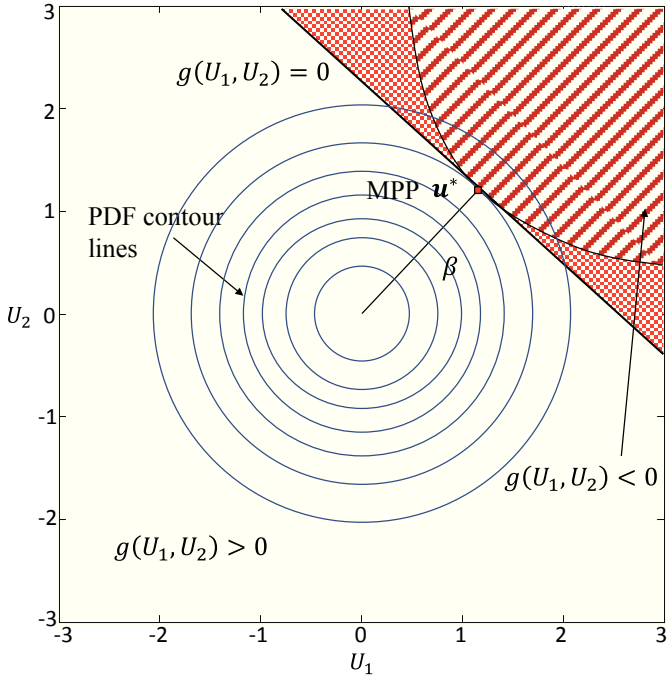

Figure 2.8: Plan view of the integration domain in FORM (Du, 2015).

$$\beta_{HL} = \frac{g(\boldsymbol{u}^*) + \nabla g^T \cdot (\boldsymbol{\mu_U} - \boldsymbol{u}^*)}{\sqrt{\nabla g^T \sum_{\boldsymbol{U}} \nabla g}} \tag{2.39}$$

Since $g(\boldsymbol{u}^*) = 0$ (the MPP is a point of the failure surface) and $\boldsymbol{U}$ has zero mean and identity covariance matrix, Eq. (2.39) is simplified to

$$\beta_{HL} = -\frac{\nabla g^T}{\sqrt{\nabla g^T \nabla g}} \cdot \boldsymbol{u}^* = \boldsymbol{\alpha}^T \boldsymbol{u}^* \tag{2.40}$$

where $\boldsymbol{\alpha} = -\nabla g / \|\nabla g\|$ is the negative normalised gradient vector. As shown in Figure 2.9, the MPP is the tangent point between the limit state $g(\boldsymbol{U}) = 0$ and the circular contour line with radius β_{HL}. Therefore, both the unit vector $\boldsymbol{\alpha}$ and the MPP vector $\boldsymbol{u}^*$ have the same direction perpendicular to the curve $g(\boldsymbol{U}) = 0$. Since $\beta_{HL} = \|\boldsymbol{u}^*\|$, the following equivalence can then be established,

$$\beta_{HL} = \boldsymbol{\alpha}^T \boldsymbol{u}^* \iff \boldsymbol{u}^* = \beta_{HL} \boldsymbol{\alpha} \tag{2.41}$$

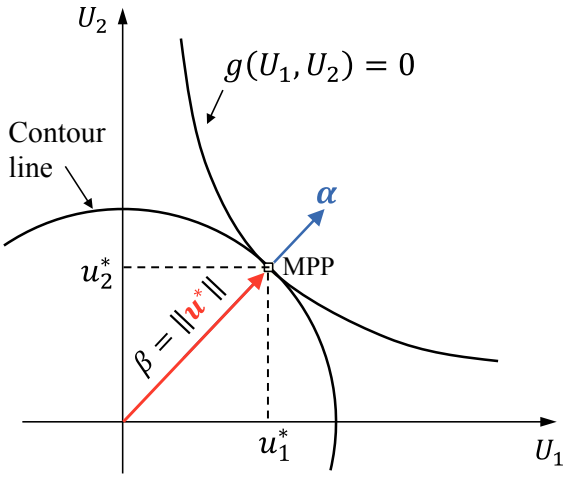

Figure 2.9: Relation among β_{HL}, the unit vector $\boldsymbol{\alpha}$ and the MPP vector $\boldsymbol{u}^*$.

Finally, the probability of failure is derived by replacing Eq. (2.40) into Eq. (2.15), so that

$$P_f \cong \Phi(-\beta_{HL}) = \Phi(-\boldsymbol{\alpha}^T \boldsymbol{u}^*) \tag{2.42}$$

The expression above provides an approximate evaluation of the failure probability, and it matches with the exact solution if the performance function $g(\boldsymbol{U})$ is linear (i.e., if both hypotheses *i)* and *ii)* in Section 2.2 are verified).

2.1.6 The MPP search algorithm

The solution of the optimization problem (2.37) has motivated development of dedicated algorithms, as the Hasofer and Lind (1974) and Rackwitz and Fiessler (1978) algorithm (HLRF). This algorithm consists on a recursive approach, where a linear approximation to the limit state is operated at every search point.

Let the MPP in the *k*-th iteration be $\boldsymbol{u}^k$. The performance function $g(\boldsymbol{U})$ is then expanded in a Taylor series about $\boldsymbol{u}^k$ providing the following recursive formula,

$$g(\boldsymbol{u}^{k+1}) = g(\boldsymbol{u}^k) + (\nabla g^k)^T \cdot (\boldsymbol{u}^{k+1} - \boldsymbol{u}^k) \tag{2.43}$$

being ∇g^k the gradient vector at $\boldsymbol{u}^k$. At converge, $\boldsymbol{u}^{k+1}$ is the shortest distance point of the limit state to the origin of the space $\boldsymbol{U}$, so that the second of Eqs. (2.41) applies,

$$\boldsymbol{u}^{k+1} = \beta^{k+1}\boldsymbol{\alpha}^k \quad , \qquad \boldsymbol{\alpha}^k = -\nabla g^k / \|\nabla g^k\| \tag{2.44}$$

where the subscript of β_{HL} has been omitted for readability. Eq. (2.43) can then be solved by letting $g(\boldsymbol{u}^{k+1}) = 0$ and approximating $\boldsymbol{u}^k = \beta^k\boldsymbol{\alpha}^k$,

$$g(\boldsymbol{u}^k) + (\nabla g^k)^T\boldsymbol{\alpha}^k \cdot (\beta^{k+1} - \beta^k) = g(\boldsymbol{u}^k) + \|\nabla g^k\| \cdot (\beta^{k+1} - \beta^k) \tag{2.45}$$

Rearranging Eq. (2.45) leads to the recursive formula

$$\beta^{k+1} = \beta^k + \frac{g(\boldsymbol{u}^k)}{\|\nabla g^k\|} \tag{2.46}$$

Finally, Eq. (2.46) is substituted into Eq. (2.44) leading to the following explicit scheme,

$$\boldsymbol{u}^{k+1} = \left[(\boldsymbol{\alpha}^k)^T\boldsymbol{u}^k + \frac{g(\boldsymbol{u}^k)}{\|\nabla g^k\|}\right]\boldsymbol{\alpha}^k \tag{2.47}$$

Two convergence criteria may be used to terminate the MPP search process. First, the design point should be located on the failure surface, so that

$$\left|\frac{g(\boldsymbol{u}^k)}{g(\boldsymbol{u}^0)}\right| < e_1 \tag{2.48}$$

where $\boldsymbol{u}^0$ is the starting point and e_1 is a user-defined acceptance tolerance. A common choice is to set $\boldsymbol{u}^0 = \boldsymbol{0}$ (at the origin) and $e_1 = 10^{-3}$. Second, the design point should be parallel to the gradient vector, therefore the vector difference between $\boldsymbol{u}^k$ and the component of $\boldsymbol{u}^k$ in the direction of $\boldsymbol{\alpha}^k$ must satisfy the following criterion,

$$\|\boldsymbol{u}^k - (\boldsymbol{\alpha}^k)^T \boldsymbol{u}^k \boldsymbol{\alpha}^k\| < e_2 \tag{2.49}$$

where e_2 is also commonly selected as 10^{-3} (Liu, Lin, & Der Kiureghian, 1989).

However, despite HLRF method has been shown to be very efficient, there is no mathematical proof for its convergence and it fails to converge for a considerable number of problems (Liu & Der Kiureghian, 1986b, 1992). Zhang and Der Kiureghian (1997) developed an improved HLRF algorithm (iHLRF), by introducing a non-differentiable merit function and using the Armijo rule (Polak, 1997) for the step size. In other words, the search direction $\boldsymbol{d}^k$ yielded by HLRF,

$$\boldsymbol{d}^k = \left[(\boldsymbol{\alpha}^k)^T \boldsymbol{u}^k + \frac{g(\boldsymbol{u}^k)}{\|\nabla g^k\|}\right] \boldsymbol{\alpha}^k - \boldsymbol{u}^k \tag{2.50}$$

is used to define a so-called *linear search* scheme,

$$\boldsymbol{u}^{k+1} = \boldsymbol{u}^k + \lambda^k \boldsymbol{d}^k \tag{2.51}$$

where the step size λ^k is selected along the pre-selected search direction $\boldsymbol{d}^k$ (note that the recursive formula in Eq. (2.47) is recovered when a full step is used, i.e. $\lambda^k = 1$). The ideal step size is found using the Armijo rule (e.g., dividing λ^k in half) each time a trial step size does not satisfy a condition of sufficient decrease in the merit function

$$m(\boldsymbol{u}) = \frac{1}{2}\boldsymbol{u}^T\boldsymbol{u} + c \cdot |g(\boldsymbol{u})| \quad , \qquad c > \frac{\|\boldsymbol{u}\|}{\|\nabla g(\boldsymbol{u})\|} \tag{2.52}$$

where the inequality establishes the conditions for $\boldsymbol{d}^k$ in Eq. (2.50) to be a descent direction for the merit function $m(\boldsymbol{u})$. The flowchart of the iHLRF algorithm is shown in Figure 2.10.

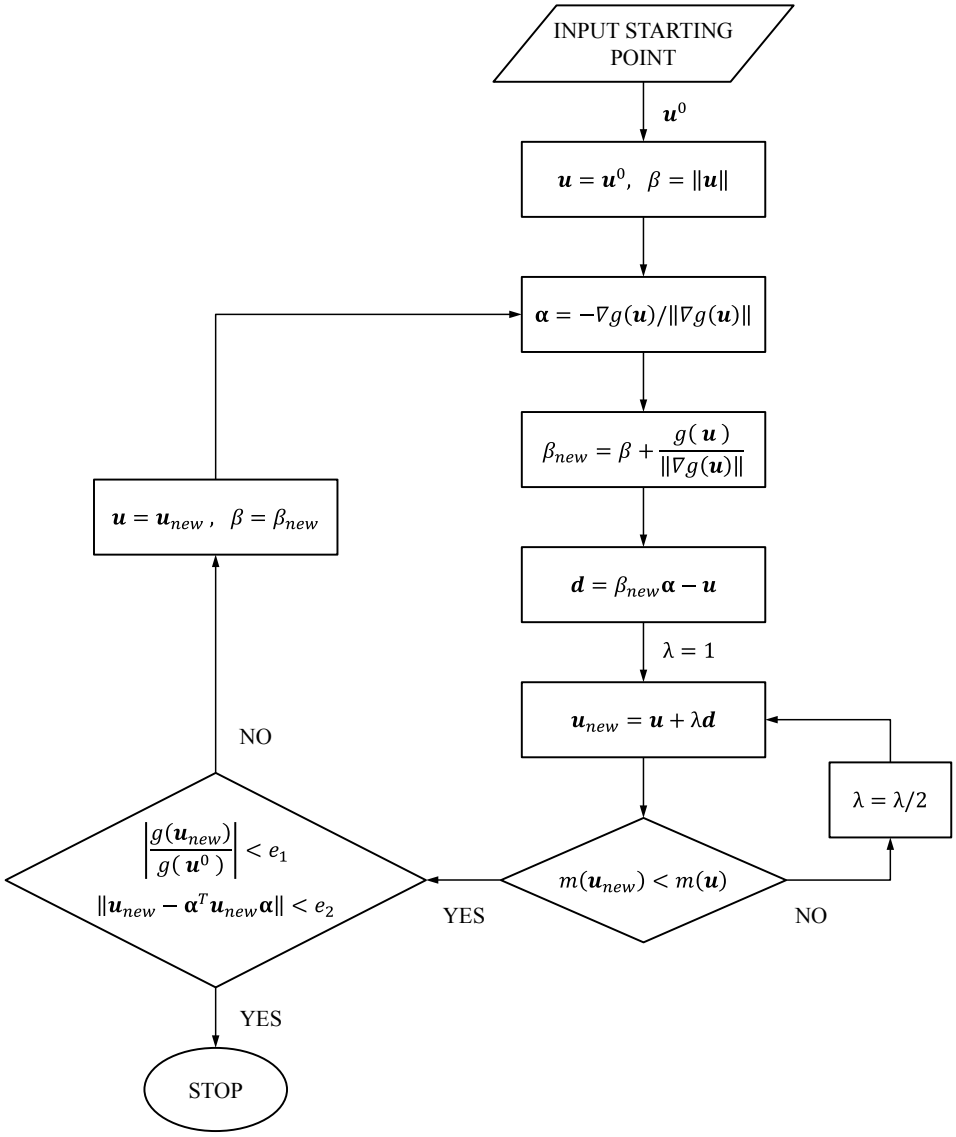

Figure 2.10: The flowchart of the iHLRF algorithm.

2.1.7 Second-Order Reliability Method (SORM)

Despite FORM requires a very small computational effort, a first order approximation can significantly depart from the true solution when dealing with highly nonlinear limit states. Nonlinearities are due to nonlinear relationship between the random variables, or because some variables are non-normal (even a linear limit state in the original space becomes nonlinear after the transformation to the standard normal space). In such instances, a better accuracy can be achieved by the Second-Order-Reliability-Method (SORM), which takes into account the curvature of the failure surface around the MMP $\boldsymbol{u}^*$,

$$g(\boldsymbol{U}) \cong g(\boldsymbol{u}^*) + \nabla g^T \cdot (\boldsymbol{U} - \boldsymbol{u}^*) + \frac{1}{2}(\boldsymbol{U} - \boldsymbol{u}^*)^T H(\boldsymbol{U} - \boldsymbol{u}^*) \tag{2.53}$$

where H is the Hessian matrix evaluated at $\boldsymbol{u}^*$.

Several approximations of the failure probability based on a second-order approximation have been proposed (Der Kiureghian, Lin, & Hwang, 1987). Breitung (1984) suggested an exact asymptotic expression of the failure probability based on the reliability index β_{HL} estimated by FORM,

$$P_f = \Phi(-\beta_{HL}) \prod_{i=1}^{n-1} \frac{1}{\sqrt{1 + \beta\kappa_i}} \tag{2.54}$$

where κ_i denotes the principal curvature of the failuire surface at the MPP $\boldsymbol{u}^*$. It is worth noticing that Eq. (2.54) can be viewed as a correction of the FORM formula in Eq. (2.42).
An improved Breitung's model was provided by Hohenbichler and Rackwitz (1988), while Tvedt (1983) added two higher order terms to Breitung's formula. Exact results for a paraboloid were derived by Tvedt (1988) and further extended to all the quadratic forms of Gaussian variables (Tvedt, 1990). All these approaches are referred to as curvature fitting methods, in that they need the second derivative of the limit state function and the eigenvalues of the Hessian matrix (i.e., the curvatures). Conversely, a point fitting method was developed by Der Kiureghian et al. (1987), where the limit state is fitted at discrete points in the proximity of the design point and successively approximated by two semi-parabolas. Neither second derivatives nor eigen solution are needed in the latter approach. This method, however requires an iterative search to determine the fitting points.

An in-depth description of the second order reliability methods is beyond the scope of the present work, and SORM will only be used to verify the accuracy of the first-order estimates along with Monte Carlo analysis, which will be introduced in the next section.

2.1.8 Monte Carlo analysis

Monte Carlo methods are widely used for simulating systems with significant uncertainty in inputs and with a large number of coupled degrees of freedom. Areas of application range from the simulation of complex physical phenomena such as atom collisions to the analysis of portfolios in finance. Of particular interest is their capability of evaluating multidimensional definite integrals with complicated boundary conditions, which relies on a large number of realisations of the input random variables and on the statistical analysis of the outcomes.

Consider the general reliability problem in Eq. (2.2), which is here rewritten as

$$P_f = \int_{g(\boldsymbol{X})\leq 0} f_{\boldsymbol{X}}(\boldsymbol{x})\, d\boldsymbol{x} = \int_{-\infty}^{+\infty} I(\boldsymbol{x})\, f_{\boldsymbol{X}}(\boldsymbol{x}) d\boldsymbol{x} \tag{2.55}$$

where $I(\boldsymbol{x})$ is an indicator function, which is equal to 1 if $\boldsymbol{x}$ belongs to the failure domain $g(\boldsymbol{X}) \leq 0$, and 0 otherwise; as a consequence, the associated random variable $I(\boldsymbol{X})$ follows a binomial distribution. The last integral in Eq. (2.55) is simply the mean value of $I(\boldsymbol{X})$, i.e. $P_f = \mu_I$. Therefore, the main idea at the base of the Monte Carlo analysis is to estimate P_f by the empirical average of the indicator function

$$\bar{\mu}_I = \frac{1}{N}\sum_{i=1}^{N} I(\boldsymbol{x}_i) = \frac{n_f}{N} \tag{2.56}$$

where N is the number of deterministic analyses (simulations) run by Monte Carlo, and n_f is the number of times that the samples $\boldsymbol{x}_i$ fall into the negative region $g(\boldsymbol{X}) \leq 0$. The inverse transformation method (Devroye, 1986) is most commonly used for the generation of the input vector $\boldsymbol{x}_i$, however, other sampling methods can be used such as composition method, convolution method and acceptance-rejection method (Law & Kelton, 2000; Fishman, 1995).

The Monte Carlo simulation as expressed in Eq. (2.56) always converges to the exact value of P_f for $N \to \infty$. The main problem, therefore, is to determine the minimum number of analyses N satisfying the target accuracy and the confidence interval on the accuracy. This task is accomplished estimating the error as

$$\epsilon_N = \mu_I - \bar{M}_I \quad , \qquad \bar{M}_I = \frac{1}{N}(I_1 + \cdots + I_N) \tag{2.57}$$

where $\{I_i,\ i = 1, \ldots, N\}$ is a set of independent identically distributed random variables following the binomial distribution of $I(\boldsymbol{X})$, while $\bar{M}_I$ is the random variable associated to the sample $\bar{\mu}_I$. Indicating with σ_I^2 the variance of $I(\boldsymbol{X})$, for the Central Limit Theorem (Rice,

2007) the error ϵ_N converges to a Gaussian random variable with mean 0 and variance σ_I^2/N. It follows that for all $q_1 < q_2$

$$\lim_{N\to\infty} P\left(q_1\frac{\sigma_I}{\sqrt{N}} < \epsilon_N < q_2\frac{\sigma_I}{\sqrt{N}}\right) = \int_{q_1}^{q_2} e^{-\frac{t^2}{2}}\frac{dt}{\sqrt{2\pi}} \tag{2.58}$$

Eq. (2.58) can be used to calculate the accuracy with a given confidence interval α,

$$|\epsilon_N| \le \Phi^{-1}\left(\frac{1+\alpha}{2}\right)\frac{\sigma_I}{\sqrt{N}} \tag{2.59}$$

For instance, $|\epsilon_N| \le 1.96 \cdot \sigma_I/\sqrt{N}$ with a probability of 95% ($\alpha = 0.95$). However, the true variance σ_I^2 of $I(\boldsymbol{X})$ is not known, and the empirical variance can be used as an estimate,

$$\bar{\sigma}_I^2 = \frac{1}{N-1}\sum_{i=1}^{N}(I(\boldsymbol{x}_i) - \bar{\mu}_I)^2 \tag{2.60}$$

Since $\bar{\mu}_I = \mu_I$ and $\bar{\sigma}_I^2 = \sigma_I^2$ for $N \to \infty$, the coefficient of variation $\mathrm{CoV} = \bar{\sigma}_I/\bar{\mu}_I$ is often used to check for the convergence of the simulation. Furthermore, to increase the precision of the estimate, the ratio $\bar{\sigma}_I/\sqrt{N}$ needs to be small. This might be difficult to achieve if the single analysis requires too much computational effort, so that N cannot be too large. However, a directly proportional relationship is established by Eq. (2.59) between σ_I^2 and the minimum number of analyses N which guaranties a target accuracy $|\epsilon_N|$. As a result, variance-reduction techniques have been developed to limit the minimum number N of required analyses by decreasing the variability of the simulation output. Among these are antithetic variates, control variates, moment matching methods, stratified and Latin hypercube sampling, importance sampling, and conditional Monte Carlo (see review from Boyle et al., 1997). All these methods increase the efficiency of the simulation approach described above, which is normally referred to as crude Monte Carlo Simulation (MCS).

EXAMPLE 2.3

The efficiency and accuracy of FORM, SORM and crude MCS are here compared through the case of the axially loaded tension member introduced in Example 2.2, where $g(Y, A) = YA - F$, being Y and A independent normal variables (μ_Y=100 MPa, σ_Y = 10 MPa, μ_A = 75 mm^2, σ_A = 5 mm^2), and F a deterministic parameter equal to 5000 N.

A coefficient of variation $\mathrm{CoV} = 0.05$ is chosen as the target value for the convergence of MCS (full line in Figure 2.11). The simulation terminates after $N = 1.61 \cdot 10^6$ evaluations of the performance function $g(Y, A)$ (run in 46 s), of which only $n_f = 2503$ lead to failure (Figure 2.12). The probability of failure is then estimated as $P_f = n_f/\mathrm{N} \pm |\epsilon_N|$,

where a confidence interval of 99.99% is chosen for the absolute error. At convergence, $|\epsilon_N| \cong 2 \cdot 10^{-7}$ (dashed line in Figure 2.11), so that $P_f = 0.0015546 \pm 2 \cdot 10^{-7}$. Figure 2.12 illustrates the sample points generated by Monte Carlo mapped into the space of the standard normal variables (U_1, U_2), being $U_1 = (Y - \mu_Y)/\sigma_Y$ and $U_2 = (A - \mu_A)/\sigma_A$.

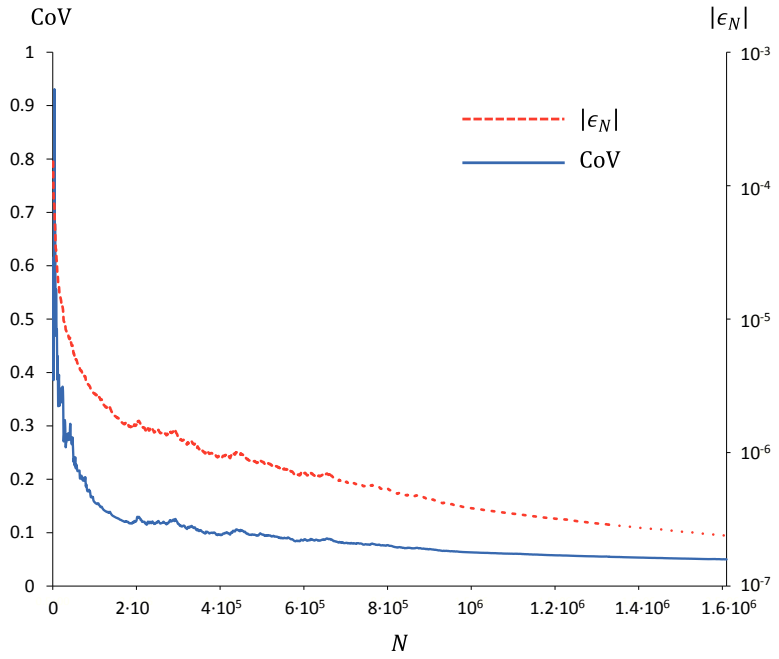

Figure 2.11: Converge of crude Monte Carlo: coefficient of variation (full line) and estimated error (dashed line).

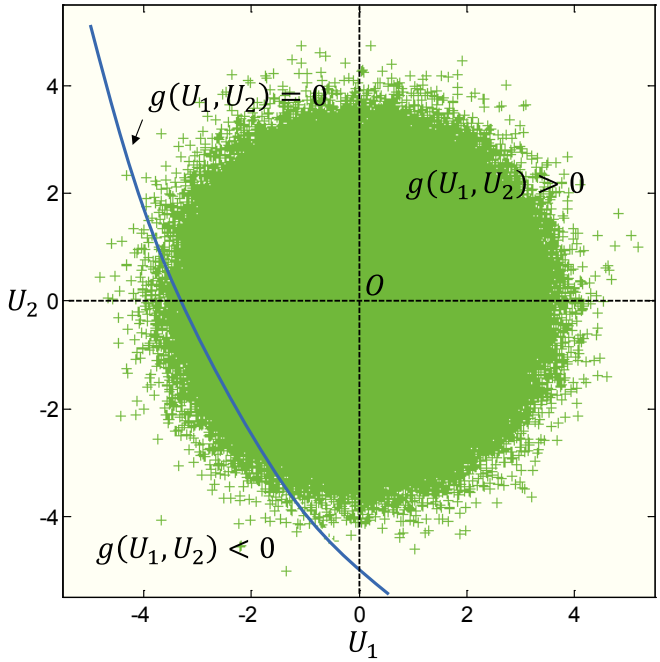

Figure 2.12: Random points generated by MCS mapped into the standard normal space.

FORM and SORM are implemented using the open-source Matlab® toolbox FERUM (Finite Element Reliability Using Matlab®) (Bourinet, 2010). FERUM output file is reported in Table 2.1, and the results are summarised in Table 2.2 along with the percentage errors calculated assuming MCS to provide the exact value of the reliability index.

Table 2.1: FERUM output file relative to FORM and SORM analyses.

```
        ###########################################################################
        #               RESULTS FROM RUNNING FORM RELIABILITY ANALYSIS            #
        ###########################################################################

Number of iterations: 6

Time to complete the analysis: 0.109

Reliability index beta1: 2.9943

Failure probability pf1: 1.37523e-003

SENSITIVITIES OF THE RELIABILITY INDEX WITH RESPECT TO DISTRIBUTION PARAMETERS
-------------------------------------------------------------------------------------------------
 var          mean        std dev           par1           par2           par3           par4
  1   8.78811e-002  -2.31245e-001   8.78811e-002  -2.31245e-001   0.00000e+000   0.00000e+000
  2   9.54338e-002  -1.36376e-001   9.54338e-002  -1.36376e-001   0.00000e+000   0.00000e+000
-------------------------------------------------------------------------------------------------

SENSITIVITIES of THE FAILURE PROBABILITY WITH RESPECT TO DISTRIBUTION PARAMETERS
-------------------------------------------------------------------------------------------------
 var          mean        std dev           par1           par2           par3           par4
  1  -3.96149e-004   1.04240e-003  -3.96149e-004   1.04240e-003  -0.00000e+000  -0.00000e+000
  2  -4.30195e-004   6.14751e-004  -4.30195e-004   6.14751e-004  -0.00000e+000  -0.00000e+000
-------------------------------------------------------------------------------------------------


        ###########################################################################
        #       RESULTS FROM RUNNING CURVATURE-FITTED SORM RELIABILITY ANALYSIS    #
        ###########################################################################

Time to complete the analysis:    0.078

Main curvatures in (n-1)x(n-1) space:    -5.43103e-002

                                          Breitung formula
Reliability index beta2 :                 2.9672
Failure probability  pf2:                 1.50285e-003

                                          Improved Breitung (Hohenbichler / Rackwitz)
Reliability index beta2 :                 2.9643
Failure probability  pf2:                 1.51686e-003

                                          Tvedt Exact Integral
Reliability index beta2 :                 2.9648
Failure probability  pf2:                 1.51458e-003
```

Table 2.2: Percentage errors with the respect to the reliability index provided by MCS.

	Failure Probability	Reliability Index	Error [%]
MCS	0.0015546	2.9567	0.00
FORM	0.0013752	2.9943	-1.27
SORM (Breitung's formula)	0.0015029	2.9672	-0.36
SORM (Hohenbichler / Rackwitz)	0.0015169	2.9643	-0.26
SORM (Tvedt Exact Integral)	0.0015146	2.9648	-0.27

As expected, SORM methods provide more accurate results than FORM. This can be explained by the almost quadratic shape of the failure surface $g(U_1, U_2) = 0$, which is better described by a second order approximation. Although SORM gives more accurate results, one has to pay the price of a higher CPU-time due to the additional calculation of the main curvatures. In general, the CPU-time depends on the time necessary to evaluate the performance function, and while the CPU-time for FORM is almost linear in the number of random variables n, the additional CPU-time for SORM grows approximately with n^2 (Bjerager, 1991). However, in this simple case, only 23 evaluations of the performance function $g(U_1, U_2)$ are required by FORM (run in 0.109 s) and just 8 more by SORM (run in $(0.109 + 0.078)$ s). The linear approximation operated by FORM is shown Figure 2.13, and the iterations for the MPP search are summarised in Table 2.3.

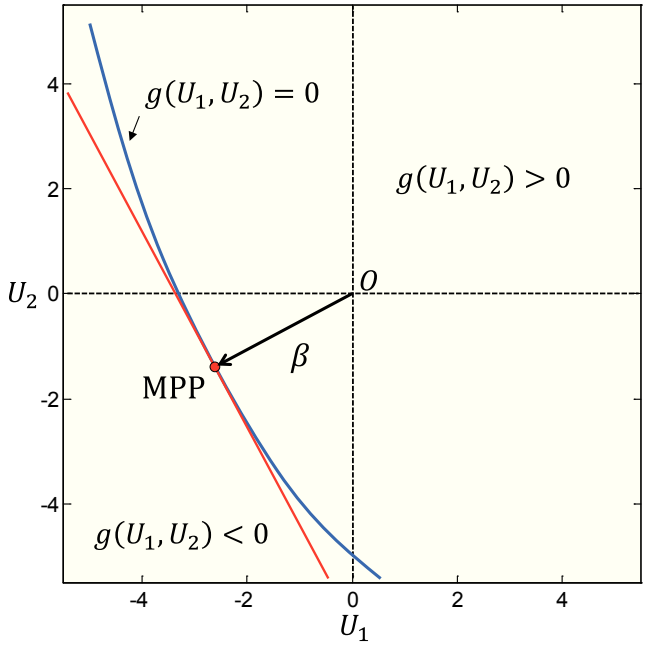

Figure 2.13: Linear approximation operated by FORM.

Table 2.3: Iteration points of the MPP search by iHLRF.

	iter. 1	iter. 2	iter. 3	iter. 4	iter. 5	iter. 6 (MPP)
U_1	0	-2.30769	-2.60118	-2.62652	-2.63066	-2.63134
U_2	0	-1.53846	-1.48639	-1.43804	-1.43026	-1.42901
$g(U_1, U_2)$	2500	177.515	-0.76412	-0.06125	-0.00161	-4.26E-05

2.2 System reliability analysis

2.2.1 Component and system failures

In structural reliability theory, the notions of component and system do not necessarily correspond to their structural counterparts. An event is called *component event* if it is defined by a single performance function or *system event* if more functions are involved. Take a beam as an example, if both yielding and buckling are considered as failure modes (i.e., two limit state equations are defined), the physical component is a system in a reliability analysis sense. Conversely, the two-element structure shown in Figure 2.14 is a component if a constraint on the displacement of node N2 is chosen as the unique failure criterion.

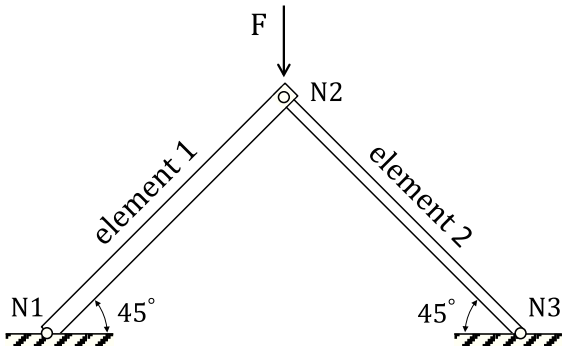

Figure 2.14: Statically determinate truss structure.

Consider the structural system shown in Figure 2.14 loaded by a single concentrated load F. Assume that system failure occurs if at least one element fails in compression. Let the compressive strength of the material be R and the cross-sectional areas of element 1 and 2 be A_1 and A_2. As it will be explained in the next section, this structure corresponds to a series system, whose failure is defined by the union of the component failure events

$$P_f = P[(g_1 < 0) \cup (g_2 < 0)] \qquad \text{where} \quad g_i = RA_i - \frac{F}{\sqrt{2}} \quad , \quad i = 1,2 \tag{2.61}$$

Assuming R and F normally distributed and A_i deterministic variables, the exact expressions of the component reliability indexes can be found from Eq. 2.14,

$$\beta_i = \frac{A_i\mu_R - \frac{\mu_F}{\sqrt{2}}}{\sqrt{A_i^2\sigma_R^2 + \frac{\sigma_F^2}{2}}} \quad , \qquad i = 1,2 \tag{2.62}$$

Figure 2.15 illustrates the system failure domain in the standard normal space, which is given by the union of the two linear half spaces $g_1(U_1, U_2) < 0$ and $g_2(U_1, U_2) < 0$, where $U_1 = (R - \mu_R)/\sigma_R$ and $U_2 = (F - \mu_F)/\sigma_F$.

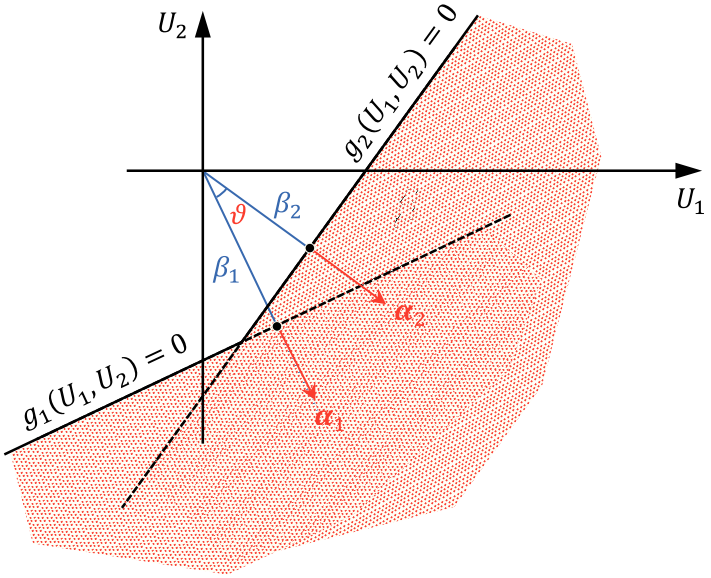

Figure 2.15: System failure domain $(g_1 < 0) \cup (g_2 < 0)$.

In order to calculate the integral over the dotted area, the component performance functions are expanded in a Taylor series about the MPP point $\boldsymbol{u}^*$ as in Eq. (2.38) (note that no approximations are made in this case, since the limit states are already linear). In this way, the performance functions can be rewritten as follows

$$g_i(\boldsymbol{U}) = g(\boldsymbol{u}_i^*) + \nabla g_i^T \cdot (\boldsymbol{U} - \boldsymbol{u}_i^*) \leq 0 \quad , \qquad i = 1,2$$

$$\nabla g_i^T \cdot (\boldsymbol{U} - \boldsymbol{u}_i^*) \leq 0$$

$$\boldsymbol{\alpha}_i^T \cdot (\boldsymbol{u}_i^* - \boldsymbol{U}) \leq 0 \quad , \qquad \boldsymbol{\alpha}_i = -\frac{\nabla g_i}{\|\nabla g_i\|}$$

$$\beta_i - Z_i \leq 0 \tag{2.63}$$

where Z_i is a standard normal variable defined by the inner product between the negative normalised gradient vector $\boldsymbol{\alpha}_i$ and the random vector $\boldsymbol{U}$. Therefore, the failure probability in Eq. (2.61) may be expressed as

$$P_f = P\left(\bigcup_{i=1}^{n}\{\beta_i - Z_i \leq 0\}\right) \quad , \qquad n = 2 \tag{2.64}$$

Applying the De Morgan's rule in set theory, $A \cup B = \overline{\bar{A} \cap \bar{B}}$ where the subscripts indicate the complementary events (Goodstein, 2007), one gets

$$
\begin{aligned}
P_f &= 1 - P\left(\bigcap_{i=1}^{n}\{\beta_i - Z_i > 0\}\right) \quad , \qquad n = 2 \\
&= 1 - P\left(\bigcap_{i=1}^{n}\{Z_i < \beta_i\}\right) \\
&= 1 - \Phi_n(\boldsymbol{\beta}, R_{\boldsymbol{Z}})
\end{aligned} \tag{2.65}
$$

where Φ_n is the n-dimensional standard normal CDF ($n = 2$ in this case), $\boldsymbol{\beta}$ is the vector of β_i's, and $R_{\boldsymbol{Z}}$ is the matrix of correlation coefficients ρ_{ij} defined by

$$
\begin{aligned}
\rho_{ij} &= \mathrm{corr}(Z_i, Z_j) \\
&= E[Z_i \cdot Z_j] = E\left[(\boldsymbol{\alpha}_i^T \boldsymbol{U}) \cdot (\boldsymbol{\alpha}_j^T \boldsymbol{U})\right] = \boldsymbol{\alpha}_i^T E[\boldsymbol{U}^T \cdot \boldsymbol{U}]\boldsymbol{\alpha}_j \\
&= \boldsymbol{\alpha}_i^T \cdot \boldsymbol{\alpha}_j
\end{aligned} \tag{2.66}
$$

The expression above also defines the correlation coefficient between the two performances $g_1 = \beta_1 - Z_1$ and $g_2 = \beta_2 - Z_2$, i.e. $\rho_{12} = \boldsymbol{\alpha}_1^T \cdot \boldsymbol{\alpha}_2 = \cos(\vartheta)$, where ϑ is the angle between the two linear limit states in the space of the standard normal variables (see Figure 2.15).

2.2.2 Series systems

A series system is generally used to model a statically determinate (non-redundant) structure, where the failure of any structural element results in a system failure (e.g., formation of a mechanism, as in the truss structure shown in Figure 2.16a).

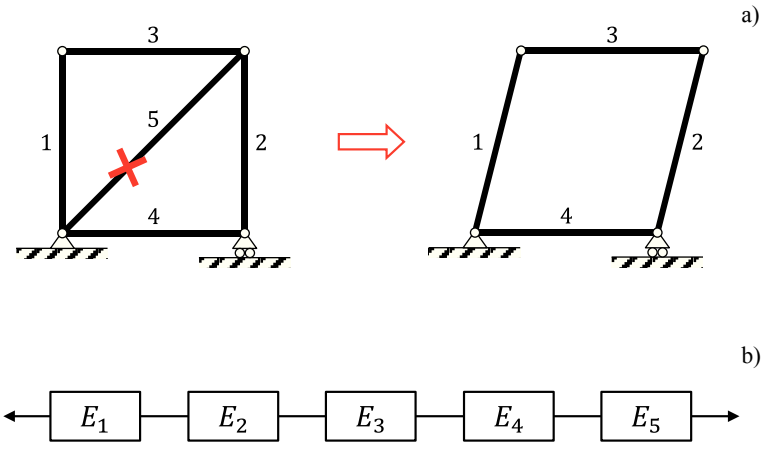

Figure 2.16: Formation of a mechanism in a statically determinate structure (a), and corresponding series system (b).

Such a system can then be represented by a chain of component events as illustrated in Figure 2.16b, where E_i indicates the i-th member failure. The chain is also called *weakest-link system*, as its strength corresponds to the strength of the weakest element. Equivalently, a chain withstands an external load only if all its elements survive the resulting stresses. From a reliability viewpoint, this can be expressed as

$$\mathcal{R} = P\left(\bigcap_{i=1}^{n}\{g_i > 0\}\right) \tag{2.67}$$

where $\mathcal{R}$ is the reliability of a series system composed by n failure elements. Hence, the probability of failure of a series system is given by

$$\begin{aligned} P_f &= 1 - P\left(\bigcap_{i=1}^{n}\{g_i > 0\}\right) \\ &= P\left(\bigcup_{i=1}^{n}\{g_i \leq 0\}\right) \end{aligned} \tag{2.68}$$

If the probabilities of the component events are estimated by FORM, then Eq. (2.68) reduces to Eq. (2.65). However, despite the latter equation simplifies the calculation of P_f, the numerical evaluation of Φ_n becomes intractable for n greater than 4. Therefore, approximate approaches must be used, as the reliability bounds originally proposed by Boole (1854), i.e.

$$\max_{1\leq i\leq n} P_i \leq P_f \leq 1 - \prod_{i=1}^{n}(1 - P_i) \leq \min\left(1, \sum_{i=1}^{n} P_i\right) \tag{2.69}$$

In this expression, the lower bound is the probability of the most likely failure event, and corresponds to the extreme case of perfect dependence ($\rho_{ij} = 1$ for all i and j) between component failure events. The opposite case of perfect independence ($\rho_{ij} = 0$, $i \neq j$) is expressed by the upper bounds, where the probability of the intersections (or unions) in Eq. (2.68) is replaced by the product (or sum) of the probabilities. These bounds are also called *simple bounds*, since they only involve unicomponent probabilities. Narrower bounds can be obtained if the bicomponent probabilities are taken into account (Ditlevsen, 1979; Hunter, 1976; Kounias, 1968)

$$P_1 + \sum_{i=1}^{n} \max\left(0, P_i - \sum_{j=1}^{i-1} P_{ij}\right) \leq P_f \leq P_1 + \sum_{i=2}^{n}\left(P_i - \max_{j<i} P_{ij}\right) \tag{2.70}$$

where P_{ij} is the probability of the joint component failure $E_i \cap E_j$. These bounds depend on the ordering of the component events, and an algorithm for optimal ordering has been

proposed by Ditlevsen (1979). Higher-order bounds have also been developed, including joint probabilities of larger sets of component events, such as tricomponent probabilities and multicomponent probabilities (Zhang Y. C., 1993).

2.2.3 Parallel systems

In the case of a statically indeterminate (redundant) structure, failure in a single element does not always result in a system failure. This is due to the residual strength provided by non-failed elements, which resist the external loads by redistribution of the internal load effects. As a consequence, more than one element is generally required to fail before leading to system failure.

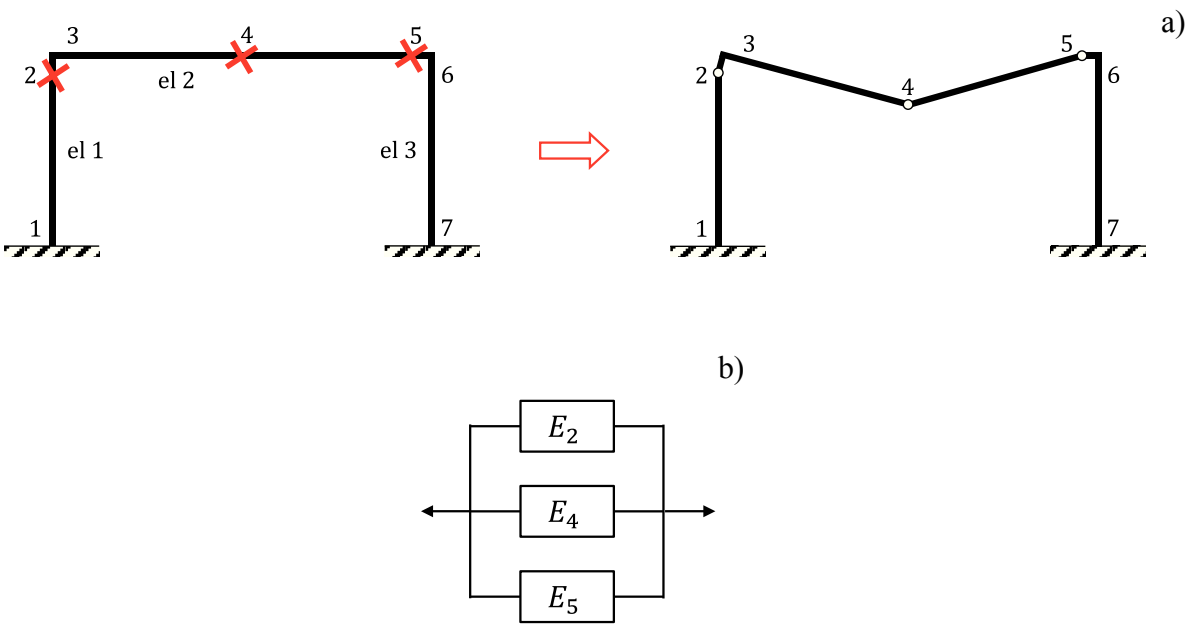

Figure 2.17: Formation of a mechanism in a statically indeterminate structure (a) and corresponding parallel system (b).

Figure 2.17a illustrates the formation of a mechanism in a frame structure due to simultaneous plastic hinging at nodes 2, 4 and 5. In a reliability analysis sense, such a mechanism is equivalent to the parallel system shown in Figure 2.17b, which represents the system event $E_2 \cap E_4 \cap E_5$. Therefore, the probability of failure of a general parallel system is defined as

$$P_f = P\left(\bigcap_{i=1}^{n}\{g_i \leq 0\}\right) \tag{2.71}$$

Analogously to series systems, simple bounds can be derived for the probability in Eq. (2.71) by considering the extreme cases of perfect independence (lower bound) and perfect dependence (upper bound) between the component failure events (Cornell, 1967)

$$\prod_{i=1}^{n} P_i \leq P_f \leq \min_{1\leq i\leq n} P_i \tag{2.72}$$

These bounds are generally too wide to be of practical use. Higher-order bounds considering bi- or tri-component probabilities do not exist for parallel systems. However, as suggested by Song and Der Kiureghian (2003), the De Morgan's rule can be applied to convert the complement of the parallel system to a series system involving the complementary component events, so that Eq. (2.69) or (2.70) can be used instead.

Alternatively, if FORM is used to estimate the probabilities of the component events, similarly to the procedure adopted for series systems (see Eqs. (2.65)), it is easily found that Eq. (2.71) reduces to

$$P_f = \Phi_n(-\boldsymbol{\beta}, R_{\boldsymbol{Z}}) \tag{2.73}$$

Of particular interest is the case of $n = 2$, for which Eq. (2.73) can be rewritten into a more useful expression that will be widely used in the next chapter. The main steps to take can be summarized as follows. First, by definition is

$$\Phi_2(-\beta_1, -\beta_2;\ \rho_{12}) = \int_{-\infty}^{-\beta_1}\int_{-\infty}^{-\beta_2} \varphi_2(t_1, t_2;\ \rho_{12})\, dt_1 dt_2 \tag{2.74a}$$

$$\varphi_2(t_1, t_2;\ \rho_{12}) = \frac{1}{2\pi\sqrt{1-\rho_{12}^2}} exp\left[-\frac{t_1^2 + t_2^2 - 2\rho_{12}t_1t_2}{2(1-\rho_{12}^2)}\right] \tag{2.74b}$$

It follows that (Ditlevsen & Madsen, 2007)

$$\frac{\partial\Phi_2(-\beta_1, -\beta_2;\ \rho_{12})}{\partial\rho_{12}} = \frac{\partial^2\Phi_2(-\beta_1, -\beta_2;\ \rho_{12})}{\partial(-\beta_1)\partial(-\beta_2)} \tag{2.75}$$

Therefore,

$$\begin{aligned}\Phi_2(-\beta_1, -\beta_2;\ \rho_{12}) &= \Phi_2(-\beta_1, -\beta_2;\ 0) + \int_0^{\rho_{12}} \left.\frac{\partial\Phi_2(-\beta_1, -\beta_2;\ \lambda)}{\partial\lambda}\right|_{\lambda=t} dt \\ &= \Phi(-\beta_1)\cdot\Phi(-\beta_2) + \int_0^{\rho_{12}} \varphi_2(-\beta_1, -\beta_2;\ t)dt\end{aligned} \tag{2.76}$$

From a numerical point of view, Eq. (2.76) is easier to calculate than Eq. (2.74a) because only a single integral is involved (Thoft-Christensen & Murotsu, 1986). Eq. (2.76) can also be used to calculate the correlation ρ_{12} between two events with known reliability indexes β_1 and β_2.

2.2.4 General systems

The number of failure modes in a redundant structure is usually very high, and system failure occurs when the weakest mode occurs. Therefore, a general structure can be represented as a chain (series) of failure modes (parallel systems), as shown in Figure 2.18.

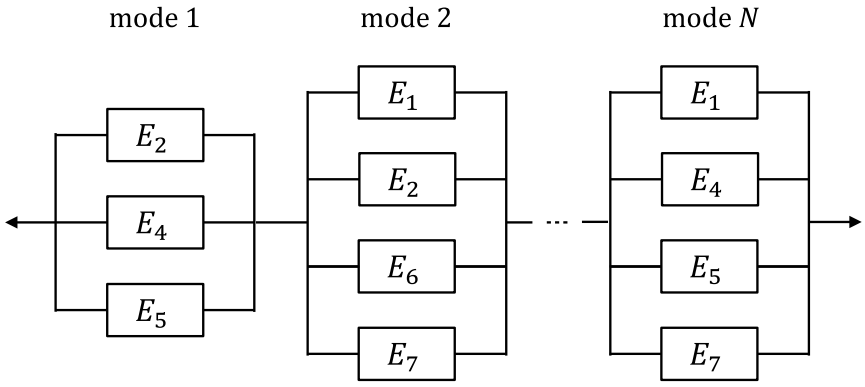

Figure 2.18: Failure modes with respect to the frame structure in Figure 2.17.

In order to better formalise such a representation of structural systems, consider a set of n component events, $E = \{E_1, \dots, E_n\}$, where n is the number of failure elements (e.g., $n = 7$ for the structure of Figure 2.17). Each component is assumed to be either in a failure or in a non-failure state. Therefore, the following Boolean variable e_i can be defined:

$$e_i = \begin{cases} 0 & i\text{-th component failed} \\ 1 & i\text{-th component safe} \end{cases} \tag{2.77}$$

A subset, $C = \{E_i \mid i \in I\}$, $I \subset \{1,2, \dots, n\}$, of E is called a *cut set* if the structure is in a failure state when all the elements in C are in a failure state and all the elements in the complement of set C are in a non-failure state, that is

$$\left.\begin{aligned} e_i &= 0\,, \quad i \in I \\ e_i &= 1\,, \quad i \notin I \end{aligned}\right\} \implies \text{system failed} \tag{2.78}$$

Finally, a cut set C is defined as a *minimal cut set* if the non-failure of any element in C results in the non-failure of the system. The difference between cut set and minimal cut set is illustrated in Figure 2.19 with reference to the failure modes of the frame structure shown in Figure 2.17.

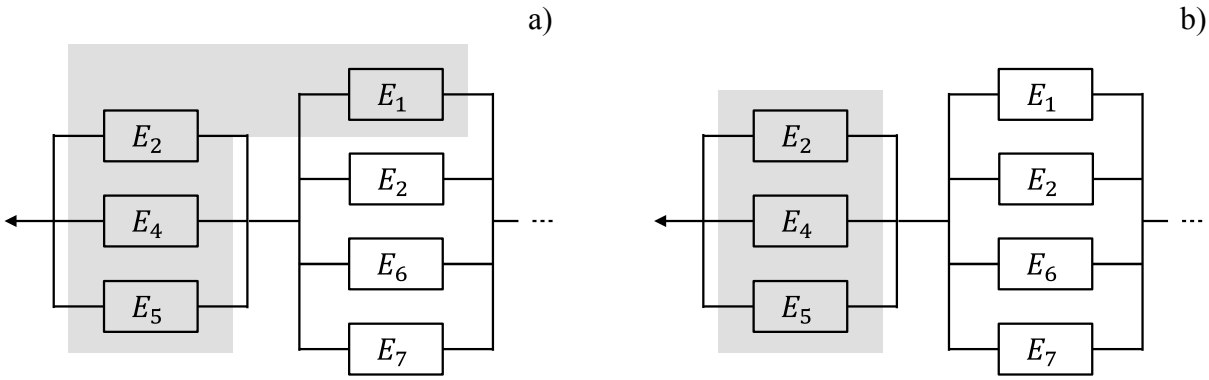

Figure 2.19: a) Cut set $C = \{E_2, E_4, E_5, E_1\}$: the system fails even if E_1 survives; b) Minimal cut set $C = \{E_2, E_4, E_5\}$: if any element in C survives, the system survives as well.

From Figure 2.19b, it is clear that any minimal cut set is defined as a subsystem in parallel. The occurrence of the system failure can, therefore, be due to element failures in any of these minimal cut sets. As a consequence, the system event can be described by the union of all the minimal cut sets of the system,

$$E_{sys} = \bigcup_{k=1}^{N_{cut}} C_k = \bigcup_{k=1}^{N_{cut}} \left[\bigcap_{i \in I_{C_k}} E_i \right] \tag{2.79}$$

where C_k is the k-th minimal cut set (failure mode), and E_i are component events of C_k.

It is noted that component events in Eq. (2.79) are generally statistically dependent on each other due to common or correlated random variables in the limit-state functions. At a higher level, failure modes C_k are also statistically dependent on each other due to common or correlated component events. Therefore, a system reliability analysis approach is needed to account for statistical dependence at both levels of the hierarchical problem, i.e. among component events (lower level) as well as among failure modes (higher level).

Several system reliability methods have been developed, such as theoretical bounding formulas (Ditlevsen, 1979; Feng, 1989; Park, 2001), sequentially conditioned importance sampling (SCIS) (Ambartzumian et al., 1998), the product of conditional marginal (PCM) method (Pandey 1998, Yuan & Pandey 2006), the multivariate normal integral method (Genz, 1992), and first-order approaches to multinormal integration (Hohenbichler & Rackwitz 1983, Tang & Melchers, 1987) that applies component reliability analyses to series and parallel systems directly, and to cut-set systems in conjunction with bounding formulas. However, these methods are not flexible in incorporating various types and amount of available information on the individual or joint component probabilities. Moreover, the complexity of a general system event can lead to more complicated and time-consuming reliability computations.

To solve these problems, a bounding approach was developed by Song and Der Kiureghian (2003) using linear programming (LP), and it was further extended to multi-scale analysis (Der Kiureghian & Song, 2008). Despite this method provides the narrowest possible bounds on the probability of any general systems, it is prone to numerical issues when the available information on the joint component probabilities is complete (which leads to an over-constrained LP problem). To preserve the main framework of the LP bounds method even in the case of complete information, Song and Kang (2007) proposed a matrix-based system reliability (MSR) method, in which the reliability is computed by simple matrix calculations instead of solving an LP problem. The MSR method is capable of solving general system events with a high degree of accuracy and efficiency (Kang et al., 2012; Kang, Song & Gardoni, 2008; Lee et al., 2011; Nguyen, Song & Paulino, 2010, 2011; Song and Kang 2009; Song and Ok, 2010).

Furthermore, several studies have focused on reducing the complexity of the system event in Eq. (2.79) by using only the dominant failure modes, i.e. failure modes that are most likely to contribute to the system failure. According to Karamchandani, Dalane and Bjerager (1992), three techniques are commonly used to identify critical failure sequences: deterministic search; locally most-likely-to-fail-based search; and branch-and-bound algorithm.

In the deterministic search (Gharaibeh, Frangopol & Onoufriou, 2002; Thoft-Christensen & Murotsu, 1986), a deterministic structural analysis is performed using the mean values of the random variables to identify the first failure sequence. To obtain additional sequences, the values of some variables are modified (e.g., strengthening some members of the identified sequence) and the deterministic analysis is repeated. However, such an approach is likely to miss important failure sequences since the identified modes may not have the largest probability of occurrence.

The locally most-likely-to-fail-based search performs a series of component reliability analyses, and the element with the largest failure probability (i.e., the "most-likely-to-fail" member) is assumed to fail first. The structural model is then updated according to the post-failure behaviour of the identified member, and a second series of component reliability analyses determines the successive most-likely-to-fail member. This process is repeated until collapse occurs and, analogously to the deterministic search, additional failure modes are identified by modifying some random variables. However, the failure modes identified by this approach may not be the most critical sequences overall. For instance, there may be a member whose failure probability is lower than that of the most-likely-to-fail member, but the conditional probability of structural collapse given its failure can be high.

Differently from the previous approaches, the branch-and-bound method (Guenard, 1984; Murotsu et al., 1984) compares the probabilities of all the partial failure sequences that have been investigated during the search process and further damage is assumed for the most

likely sequence until structural collapse is observed. In this way, system failure sequences are identified in the decreasing order of their likelihood, and the search process terminates without ignoring critical failure modes.

Despite the branch-and-bound method provides a valid alternative to the identification of the dominant failure modes, this method requires component and system reliability analyses to be performed repeatedly during the search process, which can be computationally too demanding for large structures with a high level of redundancy. Moreover, the branch-and-bound method employs theoretical bounding formulas, so that estimates of the failure mode probabilities may not be accurate. In order to overcome these challenges, a new risk assessment framework was proposed by Kim et al. (2013), where the identification process of dominant failure modes is decupled from the evaluation process of their probabilities. High accuracy and efficiency are achieved by means of a rapid multi-point parallel search employing a genetic algorithm, which is followed by a multi-scale system reliability analysis employing the MSR method (Song and Kang, 2007). In the next chapter, the applicability of this risk assessment framework to the offshore field will be investigated.

3 Reliability analysis of offshore structures

In this chapter, the merits of a new risk assessment framework, originally developed for truss and frame structures, are investigated in view of its extensive application to offshore structural systems. The main advantage of the proposed method is that the identification process of dominant failure modes is decoupled from the evaluation process of the probabilities of failure modes and the system failure event. The identification phase consists of a multi-point parallel search employing a genetic algorithm, and it is followed by the evaluation phase, which performs a multi-scale matrix-based system reliability analysis where the statistical dependence among both components and failure modes is fully considered. In order to demonstrate the applicability of the proposed method to the offshore field, the problem of a jacket platform under an extreme sea state is considered, in which the uncertainties are assumed both in the wave and hydrodynamic models and in the material properties of the structural members. The computational efficiency and accuracy of the proposed approach are successfully demonstrated through comparison with Monte Carlo simulations.

The chapter is organized as follows. Section 3.1 focuses on the probabilistic modelling of the extreme environment. In Section 3.2, the structural model of the jacket platform is introduced and the expression of the hydrodynamic forces is derived. The main steps of the failure mode identification process are then presented in Section 3.3, followed by a detailed explanation of the probability evaluation process in Section 3.4. Results, discussion and concluding remarks are presented in the last two sections.

3.1 Ocean environment

3.1.1 Design approaches

Several design procedures and codes have been developed to deal with uncertainties in the marine environment, which is primarily described in terms of wind, current and wave forces. These forces are major sources of loading on offshore structures, and various wave

and hydrodynamic models relate the forces on a particular member to the amplitude, period and water depth of a regular deterministic wave (Boccotti, 2000). Therefore, checking for structural safety requires time-dependent reliability analysis. With reference to a single component, the evaluation of P_f during a prescribed duration of time Δt is defined by

$$P_f(\Delta t) = P[R - S(t) \leq 0 \text{ in } \Delta t] \tag{3.1}$$

where R is the component random strength and $S(t)$ a time varying load. Eq. (3.1) can be solved through a standard time-independent reliability analysis by reformulating the problem as (Guenard, 1984)

$$P_f(\Delta t) = P\left[R - \max_{\Delta t} S(t) \leq 0\right] \tag{3.2}$$

where $\max_{\Delta t} S(t)$ is a random variable whose distribution is derived applying the theory of extremes of random variables. In particular, three main approaches can be distinguished for the design of offshore structures under extreme environmental loading, which are commonly referred to as *design wave*, *short-term design* and *long-term design* (Chakrabarti, 2005; Guenard, 1984).

The design wave provides a relatively simple approach to the design of those structures where the load effect is primarily of quasi-static nature. In the case of fixed platforms the design wave is related to the so-called 100-*year wave*, i.e. the height of which is exceeded only once every 100 years. According to the ISO 19902 Code and standard practices, the 100-year design load is subject to a bias of 9% and a coefficient of variation (CoV) of 16.5% relative to the actual 100-year value. Such variability arises from uncertainty in extrapolation of metocean data and from wave force model (Bomel Ltd., 2002).

A more accurate approach for the analysis of the extreme environment is provided by the short-term design, which can be applied to both quasi-static and dynamic problems. Here, "short-term" is related to the concept of *sea state*, i.e. a stationary situation in which the statistical properties of the sea remain the same. A sea state is typically assumed with a specified duration of 3 or 6 *hours*. Over this period, the sea is described by a constant-parameter wave spectrum, i.e. the power spectral density (PSD, see Lutes & Sarkani, 2004) of the sea surface elevation. This spectral description retains both the random nature and the frequency content of the sea, thus providing a realistic representation of the wave features.

Finally, the long-term design involves a succession of sea states over a season, a year or the design service life of the structure. The long-term design is the most accurate approach but it is not economical from the computational point of view. In fact, it may involve response calculations for sea states that do not contribute to the design loads.

In the following, a short-term analysis is presented for the probabilistic modelling of an extreme sea storm. The wave spectrum model is introduced in Section 3.1.2, and the distribution of the wave height is derived in Section 3.1.3, which provides the input for the calculation of the wave forces on a jacket-type platform, as described in Section 3.2. In the present analysis, only wave-current loads are considered. However, the proposed approach is general and can be easily applied to more complete models, both of the marine environment and of the loads applied to the platform.

3.1.2 Wave spectrum model

When dealing with the random ocean environment, the sea state is typically defined by the power spectral density of the sea surface elevation. The PSD describes how the variance of the sea surface elevation is distributed over the frequency domain. Therefore, since the variance of a signal has units which are the square of the signal units, the wave spectrum has dimensions m^2 per unit frequency (or $\mathrm{m}^2/[\mathrm{rad/s}]$). Several power spectrum models have been developed over the years, and the most commonly used ones in the design of offshore structures are the JONSWAP and Pierson-Moskowitz spectrum (Boccotti, 2000; Chakrabarti, 2005).

Wave spectra are defined by a set of parameters, which are constant over the sea state duration. Two of the most important parameters are the peak period T_p ($= 2\pi/\omega_p$, see Figure 3.1) and the significant wave height H_s, respectively defined as the period at which the spectrum peaks and the average height of the highest $(n/4)$ waves in the short-term record (n being the total number of waves forming during the sea state). Selecting appropriate values of T_p and H_s can result in a challenging task, especially if the sea state describes an extreme design storm. In this case, the environmental contour line approach (Chakrabarti, 2005) provides a rational way for choosing short-term design storm corresponding to a prescribed return period (or annual probability of exceedance). Here, the joint probability density function (PDF) for T_p and H_s is calibrated to fit the experimental data relative to an offshore site. A contour plot is then generated in the (T_p, H_s) domain, so that each contour line collects different combinations of T_p and H_s, each one leading to sea states with the same return period. The most unfavorable sea state along the selected contour line is finally identified by means of a limited number of structural analyses.

For the present analysis, the most unfavourable sea state is assumed to be given by a JONSWAP spectrum with peak period $T_p = 14\ \mathrm{s}$ and significant height $H_s = 10\ \mathrm{m}$. The spectrum is defined over the positive frequency domain (one-sided PSD), and it is given by the following expression

$$S(\omega) = \bar{\alpha} g^2 \omega^{-5} exp\left(-1.25\left[\omega/\omega_p\right]^{-4}\right) \cdot \gamma^{exp\left(-\left[\omega-\omega_p\right]^2/\left[2\sigma^2\omega_p^2\right]\right)} \tag{3.3}$$

where $\bar{\alpha} = 0.0081$ is the modified Phillips constant (function of T_p and H_s); $g = 9.81\ \mathrm{m/s^2}$ is the gravitational acceleration; ω_p is the peak frequency ($= 2\pi/T_p$); $\gamma = 3.3$ is the peakedness parameter; and σ is the spectral width parameter, i.e. $\sigma = 0.07$ for $\omega \leq \omega_p$, $\sigma = 0.09$ for $\omega > \omega_p$. The resulting power spectrum of the sea state is shown in Figure 3.1.

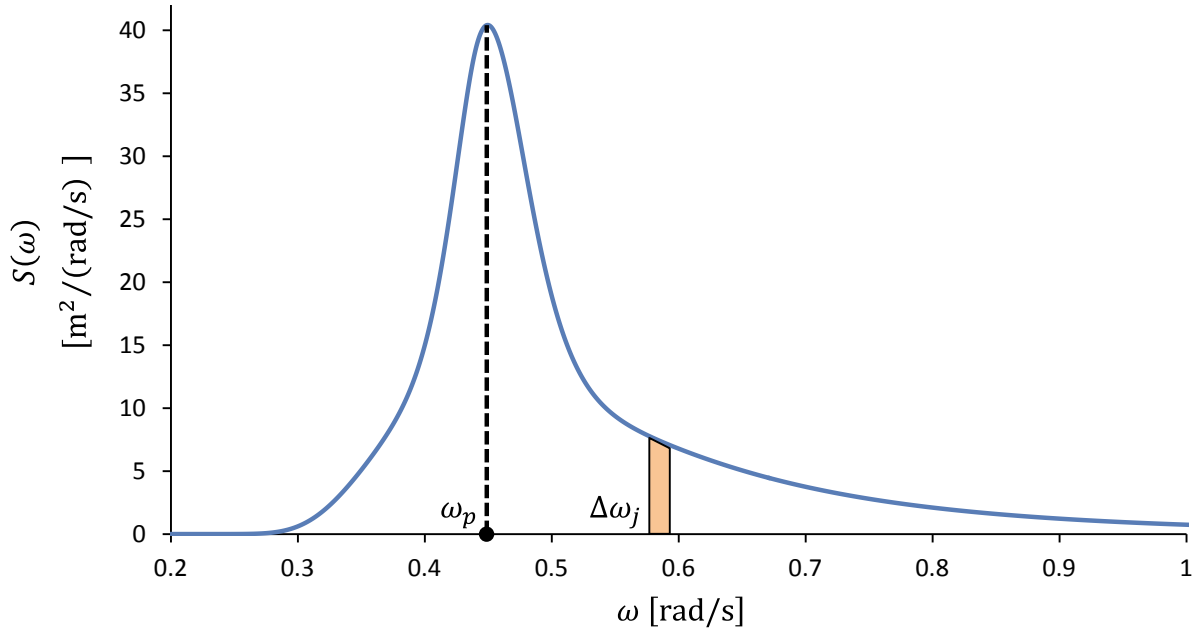

Figure 3.1: JONSWAP spectrum ($H_s = 10$ m, $T_p = 14$ s).

3.1.3 Short-term design approach

Consider a random time history of the sea surface elevation, $X(t)$ recorded at a fixed point on the mean water level. Based on the power spectrum defined above, the random surface elevation $X(t)$ can be modeled by the following formula:

$$X(t) = \sum_{j=1}^{n_s} \sqrt{2\, S(\omega_j)\Delta\omega_j}\, cos\left(\omega_j t - \varepsilon_j\right) \tag{3.4}$$

where n_s is the upper bound of summation; ω_j is the frequency within the $\Delta\omega_j$ band as shown in Figure 3.1; $S(\omega_j)$ is the average value of the PSD within this band; and ε_j are the random phase angles, which are assumed uniformly distributed on $[0, 2\pi]$ and statistically independent from each other. When n_s, is large enough, due to the central limit theorem $X(t)$ is approximately a Gaussian process. Furthermore, $X(t)$ can be considered stationary during

the sea state duration and with zero mean because of the choice of the fixed point on the mean water level. It can be also shown that the variance of $X(t)$, σ_X^2 is given by the integral of the related one-sided PSD over the positive frequency domain (Lutes & Sarkani, 2004), i.e.

$$\sigma_X^2 = \int_0^\infty S(\omega) d\omega \tag{3.5}$$

In order to obtain the short-term extreme values, the distribution of the wave crests is first derived based on the concept of *mean level upcrossing rate*, i.e the average number of times per unit time, $v_X^+(a)$ that $X(t)$ crosses the level a over the zero level $(a = 0)$ (Lin, 1967),

$$v_X^+(a) = \frac{1}{2\pi}\sqrt{\frac{m_2}{m_0}}\, exp\left(-\frac{1}{2}\frac{a^2}{\sigma_X^2}\right) \tag{3.6a}$$

$$m_j = \int_0^\infty \omega^j S(\omega) d\omega \tag{3.6b}$$

where m_j is the j-th order spectral moment, with $m_0 = \sigma_X^2$. At the zero level, $v_X^+(0)$ is called the *mean zero-upcrossing rate* and its inverse value is commonly referred to as *mean zero-upcrossing period* T_z. For a narrow band process, where there is typically only one peak between an upcrossing and the subsequent downcrossing of zero level, the distribution X_p of the wave crests can be defined by the following cumulative distribution function (CDF)

$$P(X_p > a) = \frac{v_X^+(a)}{v_X^+(0)} \;\Rightarrow\; F_{X_p}(a) = 1 - \frac{v_X^+(a)}{v_X^+(0)}, \qquad (a \geq 0) \tag{3.7}$$

By substituting Eq. (3.6a) into Eq. (3.7), it is found that the peak X_p of a zero-mean stationary Gaussian process $X(t)$ with narrow band is a Rayleigh distributed random variable, whose CDF is given by

$$F_{X_p}(a) = 1 - exp\left(-\frac{1}{2}\frac{a^2}{\sigma_X^2}\right), \qquad (a \geq 0) \tag{3.8}$$

The statistical distribution of the wave height, H, is then calculated assuming the wave crest and the subsequent wave trough having the same size, i.e. $H = 2X_p$. From Eq. (3.8), one gets

$$F_H(h) = 1 - exp\left[-\frac{1}{2}\frac{(h/2)^2}{\sigma_X^2}\right], \qquad (a \geq 0) \tag{3.9}$$

Finally, the short-term extreme values for the wave height is obtained calculating the distribution of the largest heights H_p during the storm duration T. From the order statistics theory (Arnold, Balakrishnan & Nagarja, 1992), it can be shown that

$$F_{H_p}(h) = [F_H(h)]^N \tag{3.10}$$

where N is the expected total number of zero-crossing waves during the short-term duration T, i.e. $N = \upsilon_X^+(0) \cdot T$.

Considering the JONSWAP spectrum defined above and assuming a duration period of 3 h, the variance of $X(t)$ is found to be $\sigma_X^2 = 6.25\ \mathrm{m}^2$; the value of the mean zero-upcrossing rate is $\upsilon_X^+(0) = 0.088\ \mathrm{s}^{-1}$; and $N = 950$. Given these parameters, the values of H_p can be simulated by the inverse transform sampling method (Devroye, 1986)

$$H_p = F_{H_p}^{-1}(U) = F_H^{-1}\left[(U)^{1/N}\right] \tag{3.11}$$

where U is a uniformly distributed random variable over the interval [0,1]. A set of 10^6 samples was simulated and the probability density function (PDF) of H_p was modeled as a generalized extreme value (GEV) distribution (Kotz & Nadarajah, 2000)

$$f(h;\mu,\sigma,\xi) = \frac{1}{\sigma}\left[1+\xi\left(\frac{h-\mu}{\sigma}\right)\right]^{(-1/\xi)-1} \exp\left\{-\left[1+\xi\left(\frac{h-\mu}{\sigma}\right)\right]^{-1/\xi}\right\} \tag{3.12}$$

whose parameters have been fitted using a Maximum Likelihood Estimation (MLE) method (Embrechts, Klüppelberg & Mikosch, 1997), thus leading to $\mu = 18.51$ m, $\sigma = 1.35$ m and $\xi = -0.065$.

The resulting distribution is shown in Figure 3.2, where it is compared to the Gaussian distribution of the water elevation and to the Rayleigh distribution of the wave height. The GEV distribution is shifted to the upper values of the wave heights, while its variance is lower. It can be shown that the mean value increases to infinity and the variance decreases to zero as N increases.

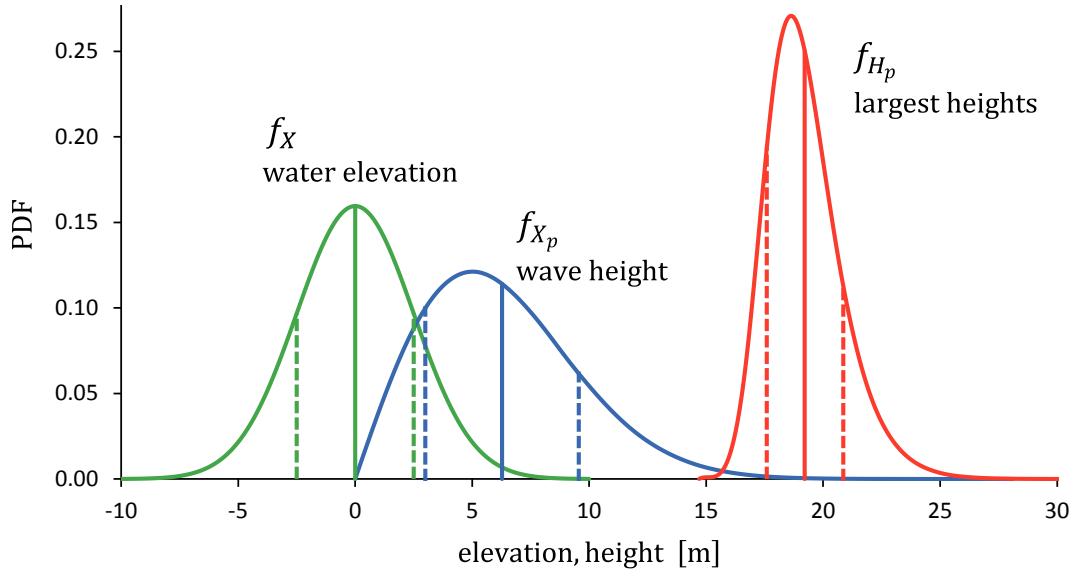

Figure 3.2: Statistical characterisation of the short-term sea state.

3.2 Structural model and load definition

The jacket-type platform shown in Figure 3.3 is considered. The structure is composed of slender cylindrical members, and the properties of the members are shown in Table 3.1. The randomness in the structural model is due to the uncertainty in the yield stress of the members, which are assumed to be uncorrelated and normally distributed.

Members are assumed to fail either in tension or compression. In the case of tension failure, the limit state equation, g_T, is given by the difference between the yield stress and the axial stress, i.e. $g_T = S_Y - S$, and a purely ductile post-failure behavior is considered, so that a residual stress $S_{res} = S_Y$ acts in the bar after the member failure. In the case of compression failure, the limit state equation, g_C, is given by the difference between the critical buckling stress and the axial stress, i.e. $g_C = S_B - S$, and the residual stress after member failure is defined according to a brittle-ductile behaviour, i.e. $S_{res} = \eta \cdot S_B$, being $\eta \in [0, 1]$. Residual stresses after tension and compression failure will be illustrated in Section 3.3 (in Figure 3.7).

In this work only the horizontal and diagonal braces of the jacket (elements with section S3, S4 and S5, see Table 3.1) are allowed to fail. This assumption seems reasonable when considering the extra strength provided by the piles inside the legs (vertical members of the jacket). It is also assumed that the members of the deck (elements with section S7 and S8, see Table 3.1) do not fail; indeed the upper part of the structure is only introduced for a more accurate evaluation of the external forces. The structure shown in Figure 3.3 is modelled as a truss. System failure is assumed to occur when the global stiffness matrix is no more definite, i.e. the structure results in a system-level failure mechanism.

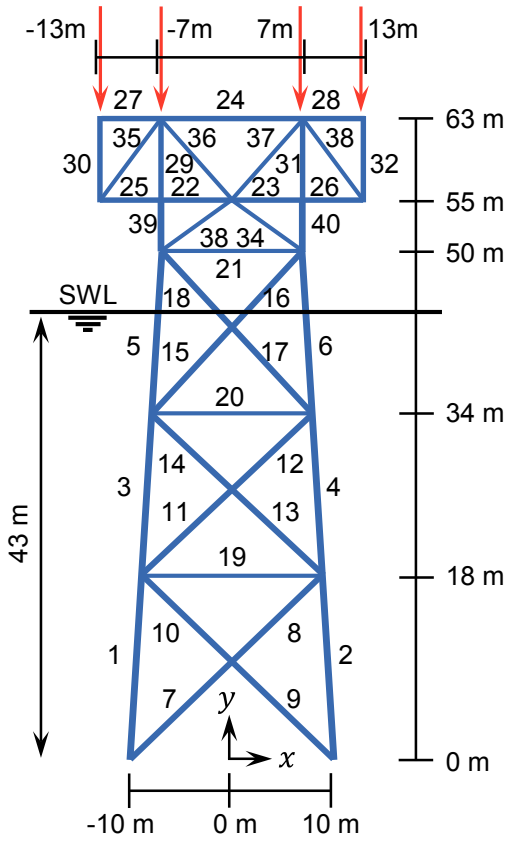

Figure 3.3: Jacket-type platform.

Table 3.1: Geometrical and material properties of members.

Section	Elements	Outside diameter [m]	Thickness [m]
S1	1, 2	0.75	0.018
S2	3 - 6	0.70	0.015
S3	19 - 21, 33, 34	0.35	0.008
S4	7 - 10	0.45	0.009
S5	11 - 18	0.45	0.008
S6	39, 40	0.60	0.013
S7	22 - 32	0.55	0.010
S8	35 - 38	0.30	0.008
Young's modulus: $E = 210$ GPa for each member Mean value of yield stress $\bar{S}_Y = 276$ MPa, CoV $= 0.08$ Correlation coefficients among member yield stresses: $\rho_{ii} = 1$ and $\rho_{ij} = 0$ for $i \neq j$.			

The following set of loading conditions is applied to the structure: wave plus current loads, self-weight and buoyancy forces in the flooded members. Moreover, four vertical forces of 5000 kN are applied on the upper hinges of the deck in order to simulate the weight of the platform modules. Among these forces, only the self-weight and the nodal forces on the deck (see Figure 3.3) are modelled deterministic. As explained below, all the other forces depend on the wave height, H_p, which is defined by the GEV distribution provided in the previous section. In particular, the combined wave-current loads are estimated by Morison's formula (Boccotti, 2000):

$$dF_k(t;\boldsymbol{x}) = \frac{1}{2}\rho C_D D(u+U)|u+U| + \rho C_M A\frac{\partial u}{\partial t} \quad \Rightarrow \quad F_k(t) = \int_0^{L_k} dF_k(t;\boldsymbol{x})dL \qquad (3.13)$$

where dF_k is the instantaneous wave force per unit of length acting at the position $\boldsymbol{x} = (x, y)$ in the direction normal to the k-th member; F_k is the total force on the k-th member of length L_k; ρ = 1025 kg/m^3 is the sea water density; D is the member diameter (including marine growth, see below); A is the cross-sectional area ($= \pi D^2/4$); u is the instantaneous velocity of the water particle, normal to the longitudinal axis of the member; U is the current velocity, which follows a normal distribution (see Table 3.2) while the current profile is uniform from the sea bed to the still water level (SWL, see Figure 3.3); and C_D and C_M are respectively the drag and mass coefficients. Experimental results indicate that such coefficients are negatively correlated ($\rho_{C_D C_M}$ = -0.9) (Thoft-Christensen & Murotsu, 1986). Moreover, a multivariate Gaussian distribution is assumed as the joint PDF of C_D and C_M (see Table 3.2), the parameters of which have been selected according to design codes (API RP2A-LRFD, 1993) for rough cylindrical members. Implicitly considered in the definition of C_D and C_M there is the marine growth, which increases wave forces by increasing member diameter and surface roughness. A marine growth thickness of 5 cm with density equal to 1400 kg/m^3 is assumed for each flooded member.

Table 3.2: Statistical properties of current speed and drag and mass coefficients.

	Mean	CoV
U	1.8 m/s	0.1
C_D	0.9	0.1
C_M	1.3	0.1

The dependence of the wave-current loads on the random wave height H_p (described in Section 3.1) is accounted for in Eq. (3.13) by the instantaneous velocity term, u, which is calculated by means of stream function theory of the 5-th order (Dean, 1974). This theory has been developed for regular waves (i.e., the period is such that each cycle has exactly the same form), whose kinematics is completely defined by the wave height, H_p, the wave period, T, and the water depth, d (= 43 m, see Figure 3.3) (see Appendix A for further details).

Among the three quantities (H_p, T, and d), only T still needs to be determined. For this purpose, the same approach adopted in (Thoft-Christensen & Murotsu, 1986) is used, in which the following deterministic relationship between H_p and T is chosen:

$$T = \alpha \cdot (H_p)^{\beta} \tag{3.14}$$

where α and β are empirical constants, which are assumed equal to 4.427 and 0.5, respectively (Thoft-Christensen & Murotsu, 1986).

Since the principal aim of the analysis is the extreme load response, the effect of the position of the wave crest relative to the central line of the platform is now investigated. To this end, Ansys-ASAS^{TM} software (ASAS User Manual, 2010) has been used to calculate the wave-current forces on the platform, where the following mean values for the input random variables have been introduced: $\bar{H}_p = 19.2\,\mathrm{m}$, $\bar{T} = 19.4\,\mathrm{s}$, $\bar{U} = 1.8\,\mathrm{m/s}$, $\bar{C}_D = 0.9$ and $\bar{C}_M = 1.3$. The trend of the resulting shear force at the base of the jacket versus the wave phase is shown in Figure 3.4, and the base shear is maximum when the wave crest is approaching approximately -2.5 m (corresponding to a wave phase of -2 deg) in front of the central line of the structure. In this way, the time dependence in Eq. (3.13) can be conservatively neglected by considering the instant with the maximum static load condition. Figure 3.5 illustrates the distributed loads due to the wave-current forces for the particular case when the wave phase is equal to -2 deg. For clarity, only the forces on the vertical elements of the jacket are displayed, however, similar distributions of forces are applied to all the members below the local water level (i.e., the diagonal and horizontal braces of the jacket and the flooded zones of the deck).

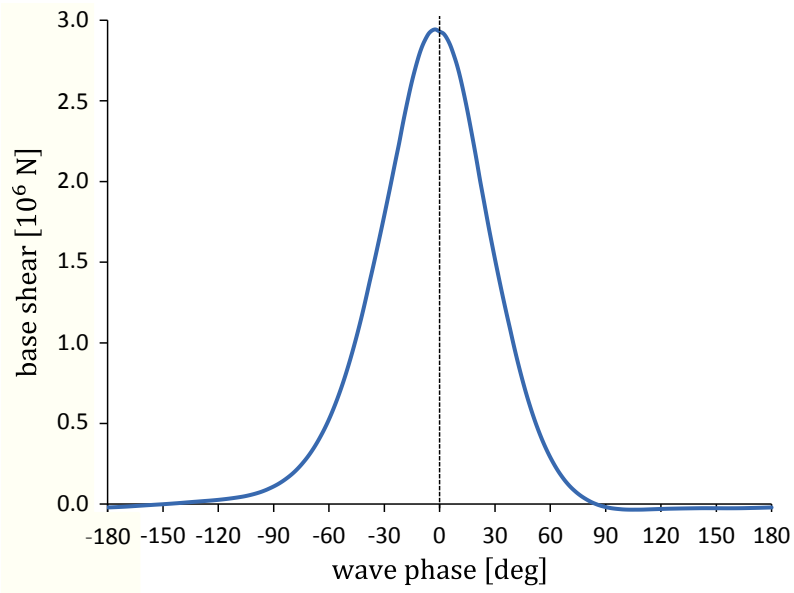

Figure 3.4: Variation of the base shear force with the wave phase.

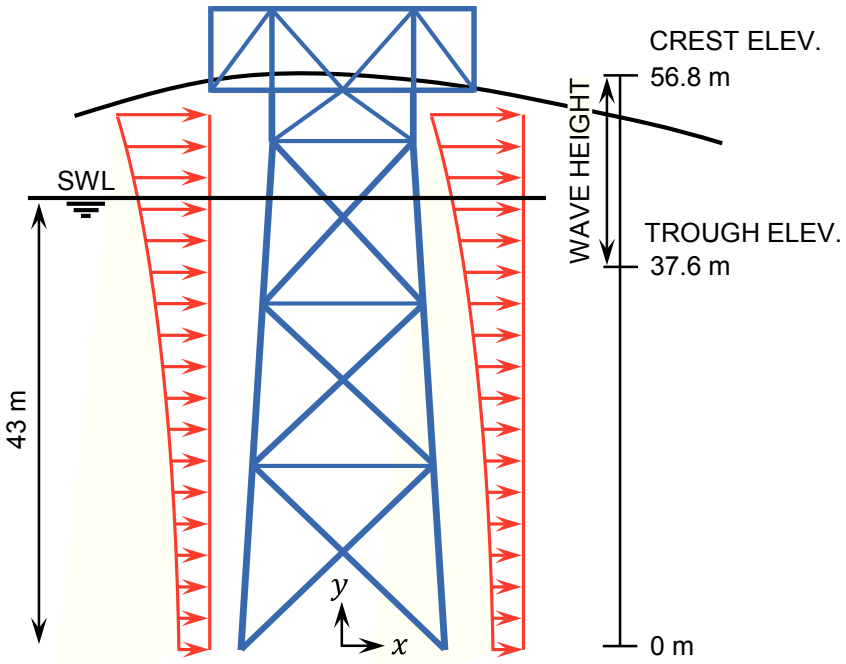

Figure 3.5: Distribution of the wave-current forces when wave phase is equal to -2 deg.

3.3 Identification of the dominant failure modes

Highly redundant systems, like the structure considered in this paper, are generally characterized by numerous failure modes, of which only some have high probabilities of occurrence and are most likely to contribute to the system reliability. Based on this observation, a new searching technique was recently proposed by Kim et al. (2013), where such dominant failure modes are rapidly and simultaneously identified by means of a genetic algorithm (GA). A brief introduction to this method is given in this section; more detailed information can be found in the reference above.

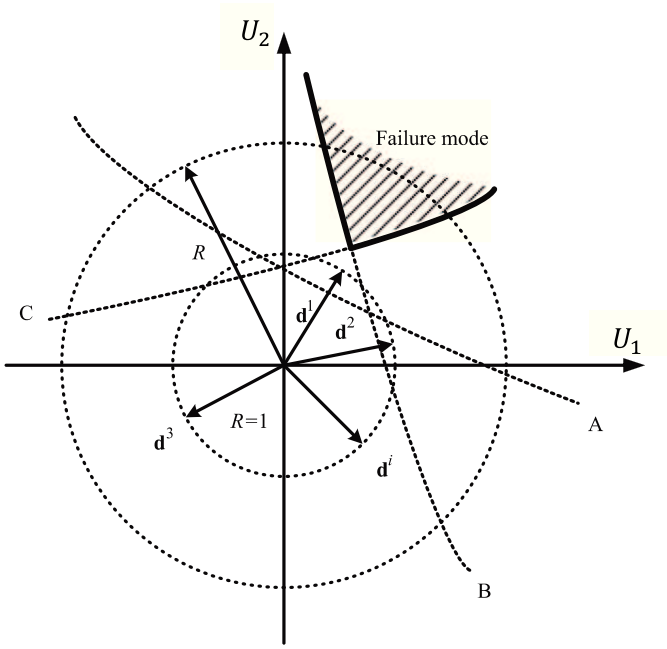

Figure 3.6: Failure mode in standard normal random variable space (Kim et al., 2013).

Let $\boldsymbol{X}$ be an n-dimensional space of random variables representing uncertain quantities in a system reliability problem. With reference to the structural model and the loading configuration proposed in Section 3.2, the random vector $\boldsymbol{X}$ is defined as $\boldsymbol{X} = (S_{Yi}, H_p, U, C_D, C_M)$, where S_{Yi}, $i = 1, \dots, 17$ are the yield stress values of the horizontal and diagonal members of the jacket (see Figure 3.3).

Consider now a nonlinear transformation (e.g., the Nataf transformation in Section 2.1.3) mapping the joint PDF of $\boldsymbol{X}$ into the corresponding space of uncorrelated standard normal variables $\boldsymbol{U}$. An example of two-dimensional standard normal space is illustrated in Figure 3.6. Here, a failure mode is defined by the joint realisation of three component failures, i.e. A, B and C, whose limit-state surfaces are represented by dotted lines and their intersection area by solid lines. In particular, the volume cut from the intersection area by the joint PDF provides the probability of the failure mode. Since the joint probability density function in the $\boldsymbol{U}$-space is determined solely by the distance from the origin, $\|\boldsymbol{u}\|$, and the

probability densities decay exponentially in both radial and tangential directions, the distance measure can be used to approximately indicate the dominance of identified failure modes. In order to identify the most dominant failure modes first, the searching method proposed by Kim et al. (2013) explores the random variable space outwardly, i.e. from the points on a hypersphere with a smaller radius (closer to the origin) to the points on a hypersphere with a larger radius (farther from the origin). Multiple dominant failure modes are then identified in the decreasing order of their likelihood and the searching process terminates as the contributions by newly identified modes become negligible. The searching procedure is implemented as follows to identify the dominant failure modes of the offshore structure considered in this work.

Step 1: A population of N_{pop} points (*chromosomes*) is randomly generated on the surface of the hypersphere with the smallest selected distance R from the origin of the $\boldsymbol{U}$-space (see Figure 3.6), i.e.

$$\boldsymbol{u}^i(R) = R \cdot \boldsymbol{d}^i = R \cdot \frac{\boldsymbol{u}^i}{\|\boldsymbol{u}^i\|}, \quad i = 1, \dots, N_{pop} \tag{3.15}$$

where R is the selected radius of the hypersphere, and $\boldsymbol{d}^i = \left[d_1^i \; d_2^i \; \cdots \; d_n^i\right]^T$ is a normalized "direction vector" that is randomly generated by Latin Hypercube Sampling (LHS) method (McKay, Beckman & Conover, 1979) or a similar sampling method.

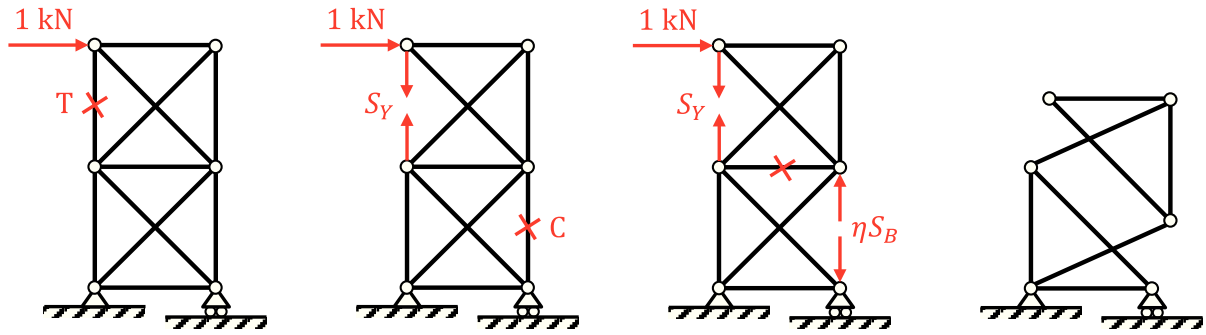

Figure 3.7: Progressive failure analysis and formation of a mechanism after redistribution of the internal load effects (T = tension failure, C = compression failure).

Step 2: A deterministic analysis is carried out for each chromosome (transformed back to the $\boldsymbol{X}$-space). The resulting stresses are used in combination with given limit state functions criteria (tension or compression failure) to check if any members have failed. In such a case, the structural model is updated on the base of a pre-established post failure behaviour (e.g., failed members with ductile behaviour are removed from the structure and replaced by their residual strength). This procedure of structural analysis and model updating is repeated until a mechanism is formed (see Figure 3.7) or load-redistributions cause no more local failures. The identified failure modes and the corresponding chromosomes are stored.

Step 3: *Crossover* and *mutation* operators (Goldberg, 1989) are introduced to generate a new offspring from previously recorded chromosomes. Generally, many failure modes are strongly correlated with each other as they share some elements and resist the same loadings. It follows that many failure modes tend to be close to each other in the random variable space. Crossover operation is then used to generate a new offspring in the vicinity of the parent population. As shown in Figure 3.8, two parent chromosomes are selected and a real value is randomly generated between 0 and 1 for each of their *genes*. If the real value is larger than a certain threshold (e.g., 0.5 in Figure 3.8), the corresponding gene of parent 1 is selected as that of the new chromosome (otherwise, the parent 2 's gene is used). The resulting chromosome is further modified by the mutation operator, where the signs of its genes can be inverted according to a *mutation probability* (e.g., 0.3 in Figure 3.8). This sign-changing operation turns the searching into the opposite direction, allowing potential failure modes located far from the identified ones to be found. Crossover and mutation operations are then repeated until a new population of N_{pop} chromosomes is generated.

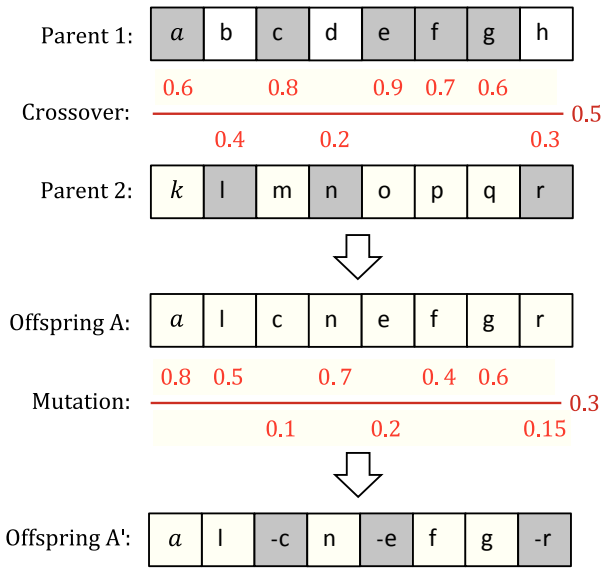

Figure 3.8: Searching operations in GA by crossover and mutation operators.

Step 4: If new failure modes are not detected over a prescribed number N_{same} of successive generations, the radius of the hypersphere, R, is increased by a small amount (e.g., 0.25 is used in this work)

Step 5: The searching process is terminated if: (*a*) the current radius is large enough (e.g., over 5, which corresponds to a failure probability in the order of $\Phi(-5) \cong 10^{-7}$), or (*b*) the probabilities of newly observed failure modes become less than a prescribed fraction (e.g., 0.1%) of the probability of the most probable failure mode identified. If both (a) and (b) are not satisfied, the procedure goes to *Step 1*.

The flowchart of the multi-point parallel search explained above is illustrated in Figure 3.9.

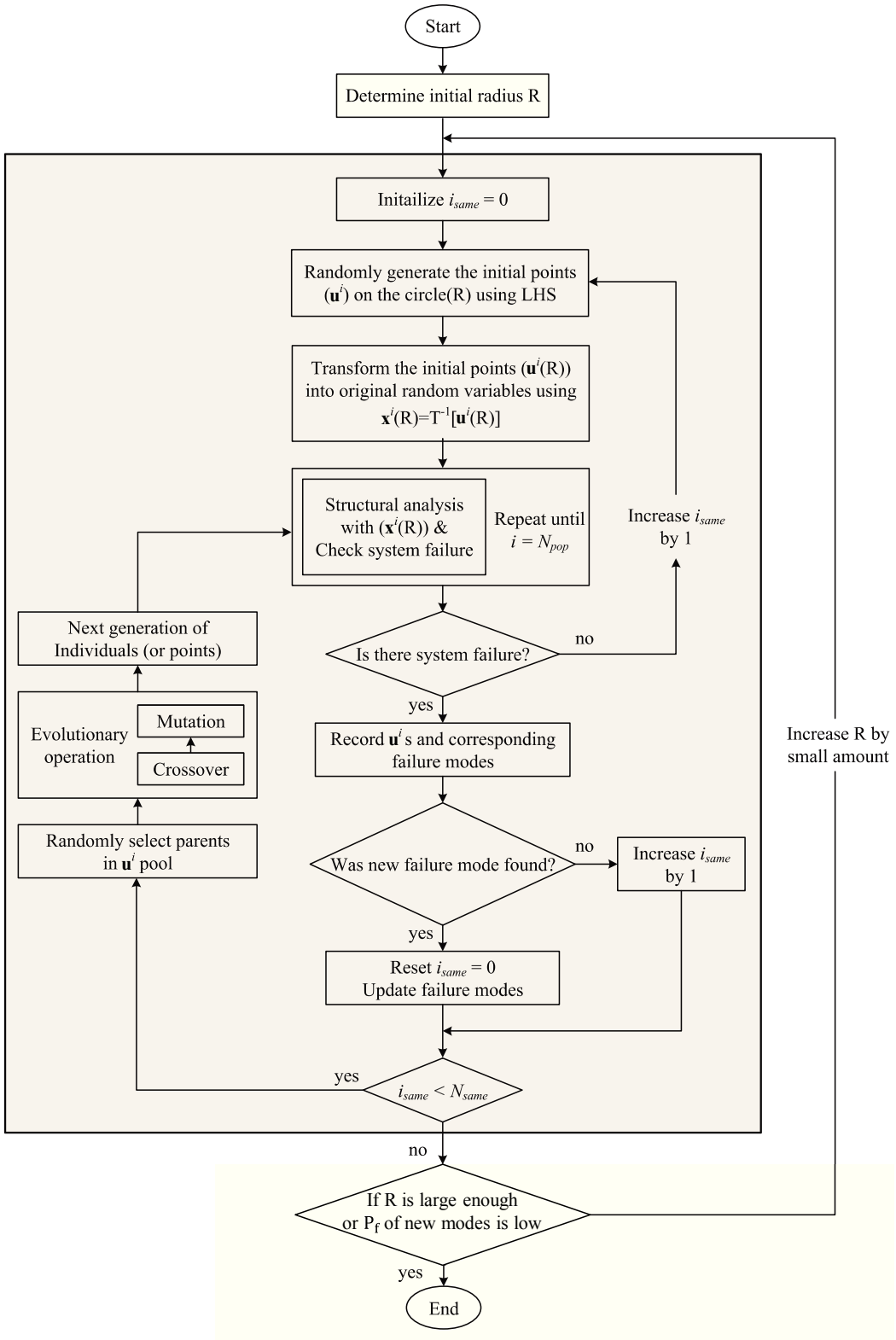

Figure 3.9: Flowchart of the multi-point parallel searching method (Kim et al., 2013).

3.4 System reliability analysis

Once the dominant failure modes are identified by the searching process described in the previous section, each of the identified modes forms a minimal cut set, C_k, $k = 1, \dots, \mathrm{N}_{cut}$ (see Section 2.2.4). The system failure event is defined by Eq. (2.79), which is here rewritten for convenience,

$$E_{sys} = \bigcup_{k=1}^{N_{cut}} C_k = \bigcup_{k=1}^{N_{cut}} \left[\bigcap_{i \in I_{C_k}} E_i \right] \tag{3.16}$$

where E_i, is the i-th component event (or member failure); and I_{C_k} is the index set of components that constitute the k-th cut set, C_k. The remaining tasks of the present analysis are summarized into the following steps:

Step 1: Estimation of the probabilities of the identified failure modes;

Step 2: Evaluation of the statistical dependence among the failure modes;

Step 3: Estimation of the probability of the system failure event.

Aside from providing inputs to the following steps, *Step 1* also helps satisfy the termination criterion (*b*) of the searching process. The calculation of the probability associated to the system failure event in Eq. (3.16) requires the use of a system reliability analysis method, because of the statistical dependence among component events (during *Step 1*), as well as among failure modes (during *Step 3*).

In order to perform these system reliability analyses with statistical dependence fully considered, Kim et al. (2013) proposed to use a multi-scale system reliability analysis framework employing the MSR method (Kang et al., 2012; Kang, Song & Gardoni, 2008; Lee et al., 2011; Nguyen, Song & Paulino, 2010, 2011; Song and Kang 2009; Song and Ok, 2010). The MSR method will be presented in the next section to provide the essential background for the comprehension of the multi-scale framework, which will be described in Section 3.4.2.

3.4.1 Matrix-based System Reliability (MSR) method

Consider the system event shown in Figure 3.10, i.e. $E_{sys} = (E_1 \cap E_2) \cup E_3$, and let the outcome e_i of E_i be defined by a Boolean variable, i.e. its value is either 1 (failure) or 0 (non-failure). The system event is characterized by $k = 3$ components, thus, the sample space can be divided into $\upsilon = 2^k = 8$ basic, mutually exclusive and collectively exhaustive (MECE, see Section 2.1.1) events, B_j, $j = 1, \dots, \upsilon$ as shown in Table 3.3.

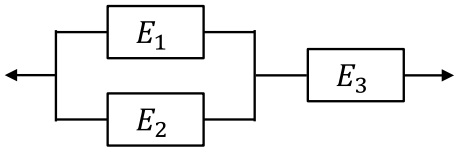

Figure 3.10: Network representation of a system event consisting of two failure modes: $(E_1\ and\ E_2)\ or\ E_3$.

Table 3.3: Basic MECE events for the three-component system in Figure 3.10.

	e_1	e_2	e_3
B_1	1	1	1
B_2	0	1	1
B_3	1	0	1
B_4	0	0	1
B_5	1	1	0
B_6	0	1	0
B_7	1	0	0
B_8	0	0	0

As a result, the probability of the system event $P(E_{sys})$ can be defined by the sum of the probabilities of basics events that belong to the system event, i.e.

$$P(E_{sys}) = \boldsymbol{c}^T \boldsymbol{p} \tag{3.17}$$

where $\boldsymbol{c}$ is the "event" vector, whose j-th element is 1 if B_j belongs to the system event and 0 otherwise; $\boldsymbol{p}$ is the "probability" vector, whose j-th element is $p_j = P(B_j), j = 1, \dots, \upsilon$. These vectors are calculated as follows. At first, the following iterative procedure is used in order to generate the binary matrix of Table 3.3:

$$\boldsymbol{C}_{[1]} = \begin{bmatrix} 1 \\ 0 \end{bmatrix}, \quad \boldsymbol{C}_{[i]} = \begin{bmatrix} \boldsymbol{C}_{[i-1]} & \boldsymbol{1} \\ \boldsymbol{C}_{[i-1]} & \boldsymbol{0} \end{bmatrix} \qquad \text{where} \quad i = 2, \dots, \mathrm{k} \tag{3.18}$$

Once the matrix is completed, its i-th column provides the event vector, $\boldsymbol{c}^{E_i}$, representing the i-th component E_i. For instance, the three columns in Table 3.3 are the event vectors $\boldsymbol{c}^{E_1}$, $\boldsymbol{c}^{E_2}$, $\boldsymbol{c}^{E_3}$. The system vector $\boldsymbol{c}$ in Eq. (3.17) can be obtained by using the following expressions for the set operations in E_{sys}:

$$\boldsymbol{c}^{\bar{E}} = \mathbf{1} - \boldsymbol{c}^{E} \tag{3.19a}$$

$$\boldsymbol{c}^{E_1 \cap \ldots \cap E_n} = \boldsymbol{c}^{E_1} .* \boldsymbol{c}^{E_2} \cdots .* \boldsymbol{c}^{E_n} \tag{3.19b}$$

$$\boldsymbol{c}^{E_1 \cup \ldots \cup E_n} = \mathbf{1} - (\mathbf{1} - \boldsymbol{c}^{E_1}) .* \cdots .* (\mathbf{1} - \boldsymbol{c}^{E_n}) \tag{3.19c}$$

where *".*"* is the element-by-element multiplication and $\bar{E}$ is the complementary event of E.

As for the probability vector $\boldsymbol{p}$ in Eq. (3.17), consider first the case of independent component events, for which the following iterative procedure is used:

$$\boldsymbol{p}_{[1]} = \begin{bmatrix} P_1 \\ \bar{P}_1 \end{bmatrix}, \quad \boldsymbol{p}_{[i]} = \begin{bmatrix} \boldsymbol{p}_{[i-1]} \cdot P_i \\ \boldsymbol{p}_{[i-1]} \cdot \bar{P}_i \end{bmatrix} \qquad \text{where} \quad i = 2, \ldots, \mathrm{k} \tag{3.20}$$

where P_i denotes the probability of the i-th component; and $\bar{P}_i = 1 - P_i$. For the example in Figure 3.10, the probability of the system event $E_{sys} = (E_1 \cap E_2) \cup E_3$ is calculated as follows:

$$\boldsymbol{c} = \boldsymbol{c}^{(E_1 \cap E_2) \cup E_3} = \mathbf{1} - (\mathbf{1} - \boldsymbol{c}^{E_1} .* \boldsymbol{c}^{E_2}) .* (\mathbf{1} - \boldsymbol{c}^{E_3}) = \{1, 1, 1, 1, 1, 0, 0, 0\}^T \tag{3.21a}$$

$$\boldsymbol{p}_{[3]} = \{P_1P_2P_3, \bar{P}_1P_2P_3, P_1\bar{P}_2P_3, \bar{P}_1\bar{P}_2P_3, P_1P_2\bar{P}_3, \bar{P}_1P_2\bar{P}_3, P_1\bar{P}_2\bar{P}_3, \bar{P}_1\bar{P}_2\bar{P}_3\}^T \tag{3.21b}$$

$$\begin{aligned} P(E_{sys}) = \boldsymbol{c}^T \boldsymbol{p}_{[3]} &= P_1P_2P_3 + \bar{P}_1P_2P_3 + P_1\bar{P}_2P_3 + \bar{P}_1\bar{P}_2P_3 + P_1P_2\bar{P}_3 \\ &= P(B_1) + P(B_2) + P(B_3) + P(B_4) + P(B_5) \end{aligned} \tag{3.21c}$$

Eq. (3.21a) indicates that E_{sys} can be seen as the union of the basic MECE events B_1, B_2, B_3, B_4 and B_5. Due to the mutual exclusivity of B_j's, the probability of the system event is the sum of the probabilities of the first five B_j's, as reported in Eq. (3.21c). The geometrical interpretation of Eq. (3.21c) is illustrated in Figure 3.11, where $P(E_{sys})$ is represented by the shaded area.

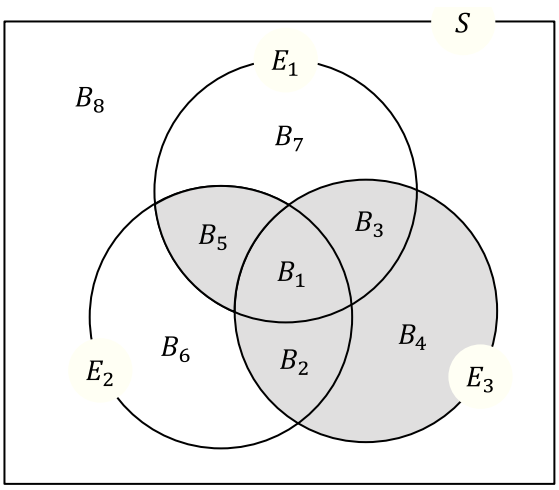

Figure 3.11: Sample space S for the three-component system in Figure 3.10.

Consider now the problem of statistically dependent component events. In such a case, the basic MECE events cannot be computed simply by products of probabilities of components and their complementary events. However, a *conditional* independence between component events can be achieved given outcomes of the random variables representing the sources of statistical dependence. For instance, let R_i, R_j and S be three independent random variables and E_i and E_j two component events defined as

$$\begin{aligned} E_i &= R_i - S \\ E_j &= R_j - S \end{aligned} \tag{3.22}$$

It follows that E_i and E_j are correlated by sharing the variable S. Such a variable is named *common source random variable* (CSRV). Only a disjoint formulation for the events E_i and E_j allows the use of the MSR method, thus, a parameterization of the cause of that dependence is needed. In other words, in the expressions of E_i and E_j the CSRV S is replaced by one of its possible outcomes s (i.e., $S = s$). Hence, the expressions in Eq. (3.22) are transformed into the following disjoint problem:

$$\begin{aligned} E_i|s &= R_i - s \\ E_j|s &= R_j - s \end{aligned} \tag{3.23}$$

When the probability of a particular system event is required (e.g., $E_{sys} = E_i \cap E_j$), all the possible outcomes s of S should be evaluated. This task is achieved by using the total probability theorem (see Section 2.1.1)

$$P(E_{sys}) = \int_s P(E_{sys}|s)\, f_S(s) ds \tag{3.24}$$

For a more general problem with m CSRVs, indicating with $\boldsymbol{S}$ the CSRVs' vector and $\boldsymbol{s}$ an outcome of $\boldsymbol{S}$, the system probability is given by

$$P(E_{sys}) = \int_{\boldsymbol{s}} P(E_{sys}|\boldsymbol{s})\, f_{\boldsymbol{S}}(\boldsymbol{s}) d\boldsymbol{s} = \boldsymbol{c}^T \int_{\boldsymbol{s}} \boldsymbol{p}(\boldsymbol{s})\, f_{\boldsymbol{S}}(\boldsymbol{s}) d\boldsymbol{s} \tag{3.25}$$

where $\boldsymbol{c}$ is obtained by the same matrix-based procedure as that in Eq. (3.18) and Eq. (3.19); and $\boldsymbol{p}(\boldsymbol{s})$ can be obtained by the iterative procedure in Eq. (3.20), where P_i is replaced by the conditional probability $P_i(\boldsymbol{s})$ because of the conditional independence of components given $\boldsymbol{S} = \boldsymbol{s}$.

The identification of CSRVs can be facilitated if the probabilities of the component events are estimated by first-order reliability method (FORM, see Section 2.1.5). Here, the failure event of the i-th component is defined by $\beta_i - Z_i \leq 0$, where β_i is the FORM reliability index and Z_i is a standard normal variable. In such a case, the correlation coefficients ρ_{ij} between Z_i and Z_j is computed by the inner product of the negative normalized gradient vectors (see Section 2.2.1), and can be fitted with a generalized Dunnett-Sobel (DS) class correlation model (Song & Kang, 2009), i.e.

$$Z_i \cong \sqrt{1 - \sum_{k=1}^{m} r_{ik}^2} \cdot Y_i + \sum_{k=1}^{m} r_{ik}\, S_k \tag{3.26}$$

where $S_k,\ k = 1, \dots, m$ and $Y_i,\ i = 1, \dots, n$ are independent standard normal variables, and r_{ik}'s are the generalized DS model coefficients, so that $\rho_{ij}^{DS} = \sum_{k=1}^{m}(r_{ik} r_{jk})$ (see Appendix B for further details). In this way, the entire common source effect is implicitly allocated in the random variables S_k and, as a consequence, the joint PDF $f_{\boldsymbol{S}}(\cdot)$ in Eq. (3.25) is replaced by $\varphi_m(\cdot)$, i.e. the m-variate uncorrelated standard normal PDF. Furthermore, the conditional probability vector $\boldsymbol{p}(\boldsymbol{s})$ in Eq. (3.25) is obtained by the matrix-based procedure in Eq. (3.20) with P_i replaced by the following conditional component probabilities:

$$P_i(\boldsymbol{s}) = P(\beta_i - Z_i \leq 0\ |\boldsymbol{s}) = \Phi\left(\frac{-\beta_i - \sum_{k=1}^{m} r_{ik}\, s_k}{\sqrt{1 - \sum_{k=1}^{m} r_{ik}^2}}\right) \tag{3.27}$$

where Φ is the CDF of the standard normal distribution. Numerical integration of Eq. (3.25) can be easily carried out when the CSRVs used to fit the DS model are not more than $m = 3$ (as in the present analysis).

3.4.2 Multi-scale system reliability analysis framework

The multi-scale system reliability analysis framework (Lim & Song, 2012; Song & Ok, 2010) is summarized into the following steps, as listed at the beginning of Section 3.4.

Step 1: First, the failure probabilities of structural members that have progressively failed in the same failure mode need to be calculated. For this purpose, first- or second-order reliability methods (FORM or SORM; see Sections 2.1.5 and 2.1.7) are performed, which also provide the correlation coefficient, ρ_{ij}, between the standard normal variables Z_i and Z_j of the component events E_i and E_j as described above. The resulting correlation matrix $R = \{\rho_{ij}\}$ is fitted with a generalized DS model $R^{DS}(\boldsymbol{r}) = \{\rho_{ij}^{DS}\}$ through a nonlinear constrained optimisation (Kang et al., 2012) (see Appendix B). The probabilities of the failure modes $P(C_k)$, $k = 1, \dots, N_{cut}$ are then evaluated by Eq. (3.25). In particular, the system vector of a parallel system, $\boldsymbol{c}^{C_k}$, resulting from the iterative procedure in Eq. (3.18) has only its first component different than zero, i.e. $\boldsymbol{c}^{C_k} = (1,0,\dots,0)^T$, so that Eq. (3.25) can be further simplified as follows:

$$P(C_k) = P\left(\bigcap_{i \in I_{C_k}} E_i\right) = \int_{\boldsymbol{s}} \left[\prod_{i \in I_{C_k}} P_i(\boldsymbol{s})\right] \cdot \varphi_m(\boldsymbol{s}; I_m) d\boldsymbol{s} \tag{3.28}$$

where $P_i(\boldsymbol{s})$ is defined by Eq. (3.27), and I_m is the $m \times m$ identity matrix.

Step 2: The statistical dependence between the identified failure modes needs to be calculated. For this purpose, the probability of the intersection of the i-th and j-th failure modes is first described by the bi-variate normal probability formula (see Eq. 2.76), i.e.

$$P(C_i \cap C_j) \cong P(C_i) \cdot P(C_j) + \int_0^{\rho_{C_i C_j}} \varphi_2(-\beta_{C_i}, -\beta_{C_i}, \rho) d\rho \tag{3.29}$$

where β_{C_k} is the generalized reliability index of the k-th failure mode defined as $\beta_{C_k} = -\Phi^{-1}[P(C_k)]$ and $\rho_{C_i C_j}$ is the unknown correlation coefficient which represents the statistical dependence between the failure modes, C_i and C_j. The joint probability in the left-hand-side of Eq. (3.29) can be calculated by MSR method in the same way as that shown in Eq (3.28), i.e.

$$P(C_i \cap C_j) = \int_{\boldsymbol{s}} \left[\prod_{k \in I_{C_i}} P_k(\boldsymbol{s})\right] \left[\prod_{k \in I_{C_j}} P_k(\boldsymbol{s})\right] \cdot \varphi_m(\boldsymbol{s}; I_m) d\boldsymbol{s} \tag{3.30}$$

where the values of $P_k(\boldsymbol{s})$ are available from the lower-scale analysis as well as the values of $P(C_i)$, $P(C_i)$, β_{C_i} and β_{C_i}. Once $P(C_i \cap C_j)$ is calculated by Eq. (3.30), Eq. (3.29) can then be numerically solved for $\rho_{C_i C_j}$.

Step 3: Given the probabilities of the identified dominant failure modes and their correlation coefficients, a higher-scale system reliability analysis can now be performed to compute the structure-level system failure probability $P(E_{sys}) = P(\cup_{k=1}^{N_{cut}} C_k)$. First, the correlation matrix of the failure modes, $R_C = \{\rho_{C_i C_j}\}$ is fitted by a generalized DS model $R_C^{DS}(\boldsymbol{r}) = \{\rho_{C_i C_j}^{DS}\}$. Finally, the system failure probability is computed by applying the De Morgan's rule to a series system

$$P(E_{sys}) = P\left(\bigcup_{k=1}^{N_{cut}} C_k\right) = 1 - P\left[\bigcap_{k=1}^{N_{cut}} \bar{C}_k\right]$$
$$= 1 - \int_{\boldsymbol{s}} \{\prod_{k=1}^{N_{cut}} [1 - P(C_k \mid \boldsymbol{s})]\} \cdot \varphi_m(\boldsymbol{s}; I_m) d\boldsymbol{s} \tag{3.31}$$

where $P(C_k \mid \boldsymbol{s})$ is computed by Eq.(3.27) introducing β_{C_i} (instead of β_i) and the coefficients of the DS model $\boldsymbol{R}_C^{DS}(\boldsymbol{r})$. More details about the procedure described above can be found in framework (Lim & Song, 2012; Song & Ok, 2010).

3.5 Results and discussion

A database of nodal forces is generated by using Ansys-ASAS software (ASAS User Manual, 2010) for the integration in Eq. (3.13). In this way, during the selective searching process, the nodal forces are simply obtained by interpolating the database for the current samples of the input random variables H_p, U, C_D and C_M. Such an approach results in huge saving on computational time since no wave theories need to be solved during the searching process.

A series of crude Monte Carlo (MCS) analyses is also performed to evaluate the accuracy and efficiency of the selective searching technique combined with the multi-scale MSR method. The convergence of MCS is achieved when the coefficient of variations (CoVs) of the system and failure mode probabilities reach 0.03 (see Appendix C for further details).

Since the computational time required by MCS varies exponentially with the system reliability, in order to speed up the MCS analysis, the thicknesses given in Table 3.1 are reduced by 50%. As a result, a weaker structure is obtained and the system failure probability is increased. Such a modification does not undermine the validity of the proposed method, which works well whether the system failure probability is low or high, as shown in Figure 3.12a where the system reliability index, β_{sys}, is plotted versus the post-buckling factor, η. The relative errors are plotted in Figure 3.12b and summarized in Table 3.4: an excellent agreement is found between the proposed method and MCS.

A further consideration about Figure 3.12 reveals the monotonically increasing trend of the system reliability index. As far as the post-failure behaviour moves from the brittle zone (lower η) to the ductile zone (higher η), the redundancy level in the structure increases. On the other hand, the system failure probability decreases with η and this increases the computational cost of MCS exponentially as shown in Figure 3.13, especially for η exceeding 0.5. Below this threshold, the number of iterations (and time) required by MCS is almost constant due to the fact that a minimum of $500{,}000$ analyses is performed to account for the transient at the beginning of the convergence process (see Section 2.1.8, Example 2.3). By contrast, the computational cost of the selective searching technique is not heavily affected by the system failure probability (or η, as shown in Figure 3.13). The number of iterations and the computational time required by this method are 1-2 orders of magnitude less than those required by MCS and this gap increases as the system failure probability decreases. It is important to note that the total time trend for the selective searching technique is not strictly related to the corresponding number of iterations trend, as in the case of MCS. This is due to the integrations performed by the MSR solver, whose computational time depends on the number of failure modes identified during the searching process. The numerical data corresponding to Figure 3.13 are summarized in Table 3.5.

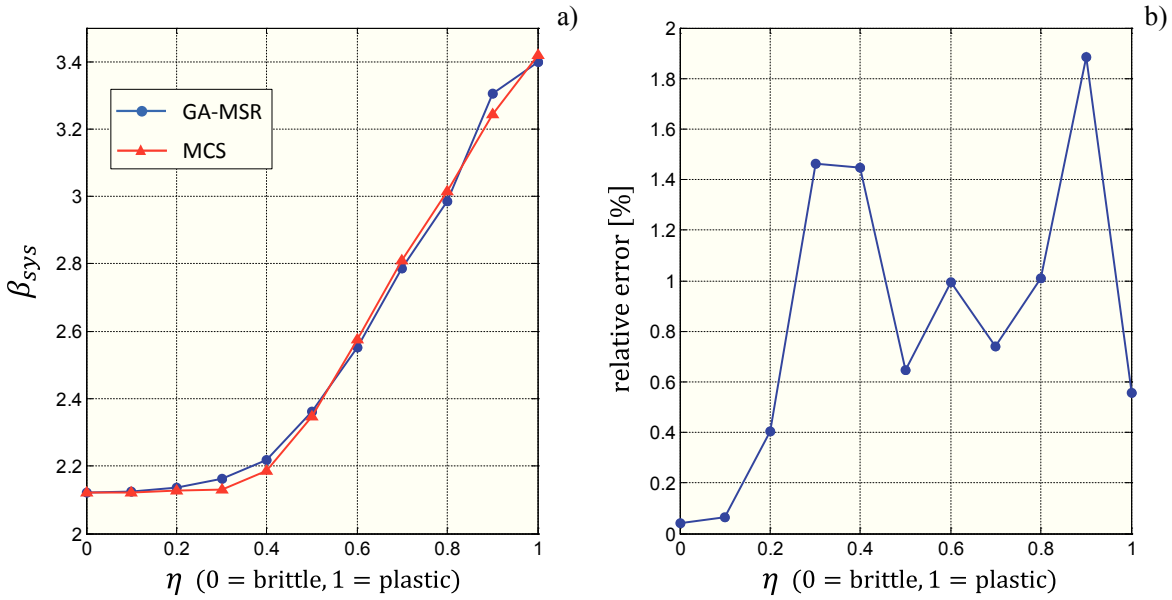

Figure 3.12: a) Influence of the post-buckling factor on the system reliability; b) relative errors between the proposed method (GA-MSR) and MCS.

Table 3.4: Results comparison between the selective searching technique and MCS.

Post-buckling Factor	Reliability Index		error [%]
	GA-MSR	MCS (CoV = 3%)	
0.00	2.1209	2.1218	0.04
0.10	2.1233	2.1219	0.07
0.20	2.1350	2.1264	0.40
0.30	2.1615	2.1303	1.46
0.40	2.2169	2.1853	1.45
0.50	2.3613	2.3461	0.65
0.60	2.5515	2.5771	0.99
0.70	2.7880	2.8088	0.74
0.80	2.9851	3.0156	1.01
0.90	3.3057	3.2445	1.89
1.00	3.3992	3.4182	0.56

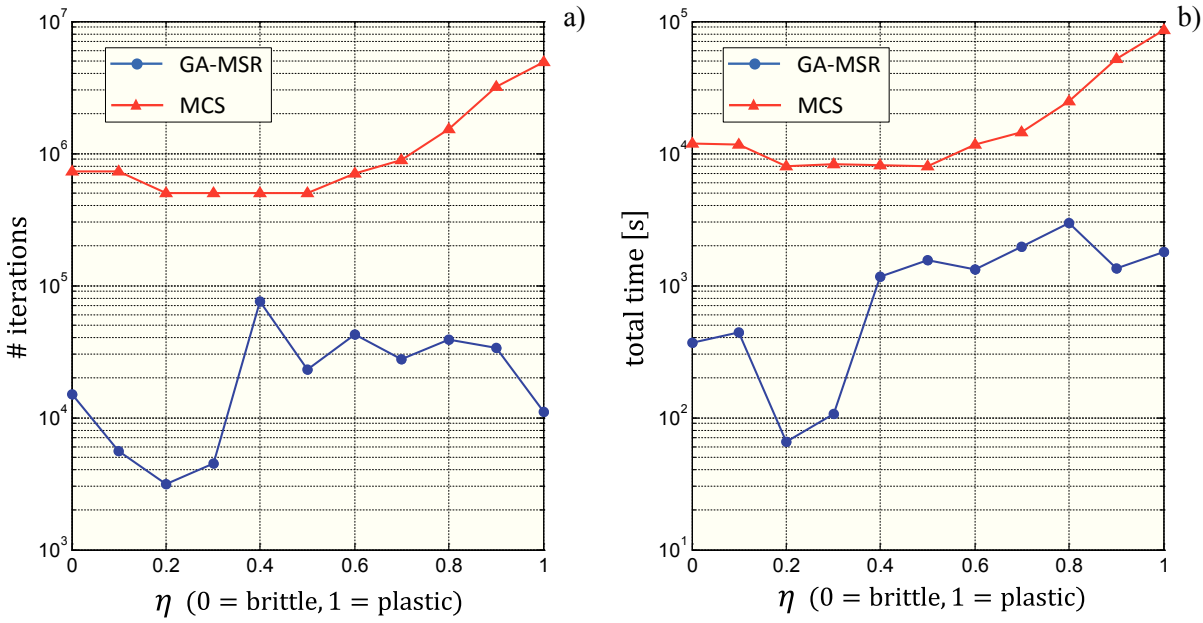

Figure 3.13: Influence of the post-buckling factor η on the computational costs of the selective searching technique and MCS in terms of a) iteration number and b) computational time.

Table 3.5: Comparison of the computational costs required by the selective searching technique and MCS.

Post-buckling factor	GA-MSR				MCS (CoV = 3%)	
	CPU time [s]			# iterations	CPU time [s]	# iterations
	Failure mode search	System reliability	Total			
0.00	201	166	367	15105	11862	730000
0.10	215	227	442	5542	11628	730000
0.20	65	0.1	65	3113	7959	500000
0.30	89	18	107	4484	8347	500000
0.40	214	950	1164	76190	8077	500000
0.50	256	1301	1557	22881	8054	500000
0.60	198	1117	1315	42256	11743	700000
0.70	345	1623	1968	27526	14462	890000
0.80	418	2536	2955	38669	25015	1530000
0.90	193	1.155	1348	33685	52203	3180000
1.00	461	1327	1788	11025	85145	4890000

Figure 3.14 illustrates the failure modes identified for $\eta = 0.5$, and their reliability indexes are reported in Table 3.6a for comparison with MCS. The failure modes are here arranged in the decreasing order of their likelihood. The following notation is used: -9 $\rightarrow$ (7,8) means, after element 9 fails in compression and the corresponding stress redistribution occurs, both elements 7 and 8 fail in tension. It is worthwhile to note the relative error increases with higher reliability indexes, especially for the last three modes. This is probably due to nonlinearities in the wave-current loads that occur for high values of the wave height, H_p. This fact can be explained by means of Figure 3.15, where the horizontal wave-current force is evaluated at two different locations, a node of the jacket (at the intersection between elements 15 and 16, see Figure 3.3) and a node of the deck (between elements 24 and 27). The load is plotted versus the wave height, H_p, while U, C_D and C_M are assumed equal to their mean values. As long as H_p is small, the wave affects the jacket only, and the response is linear. Conversely, nonlinearities are introduced in the deck nodal load for H_p exceeding 22 m, when the wave reaches the top side of the platform. So far, the results provided by MSR have been calculated performing FORM method. If SORM is used to calculate the reliability indexes in Eq. (3.27), a better accuracy of MSR can be achieved for low probability failure modes, as can be noted in Table 3.6b for the last three modes. However, for small values of H_p (or equivalently, for low reliability indexes) MSR combined with FORM method still provides a better approximation, as shown in Table 3.6a for the first three modes.

A similar behaviour is presented in Table 3.7, where the accuracy of MSR employing FORM and SORM is verified for a post-buckling factor $\eta = 0.8$. The results provided by SORM are not always more accurate to those provided by FORM, but, on average, the relative error of the first is 10% less. The minimal cut set representation of the system failure event for $\eta = 0.8$ is illustrated in Figure 3.16.

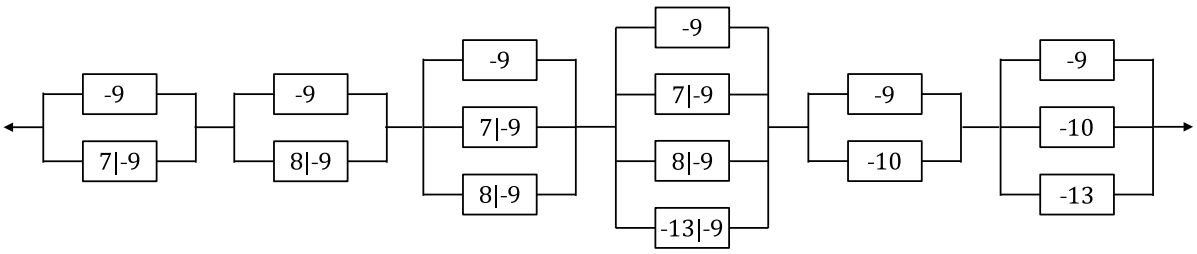

Figure 3.14: Minimal cut set representation of the system failure event for $\eta = 0.5$.

Table 3.6: Failure modes and corresponding reliability indexes for $\eta = 0.5$: a) Results provided by MSR performing FORM compared to MCS; and b) results provided by MSR performing SORM compared to MCS.

a)

	Reliability Index		
Failure modes	MSR (FORM)	MCS (CoV = 3%)	Error %
$-9 \rightarrow 7$	2.4227	2.4217	0.04
$-9 \rightarrow 8$	2.4521	2.4577	0.23
$-9 \rightarrow (7,8)$	2.5527	2.5752	0.87
$-9 \rightarrow (7,8,-13)$	3.0402	3.0777	1.22
$(-9,-10)$	3.4201	3.4923	2.07
$(-9,-10,-13)$	3.5631	3.6535	2.47

b)

	Reliability Index		
Failure modes	MSR (SORM)	MCS (CoV = 3%)	Error %
$-9 \rightarrow 7$	2.4013	2.4217	0.84
$-9 \rightarrow 8$	2.4321	2.4577	1.04
$-9 \rightarrow (7,8)$	2.5285	2.5752	1.81
$-9 \rightarrow (7,8,-13)$	3.0518	3.0777	0.84
$(-9,-10)$	3.454	3.4923	1.10
$(-9,-10,-13)$	3.5974	3.6535	1.54

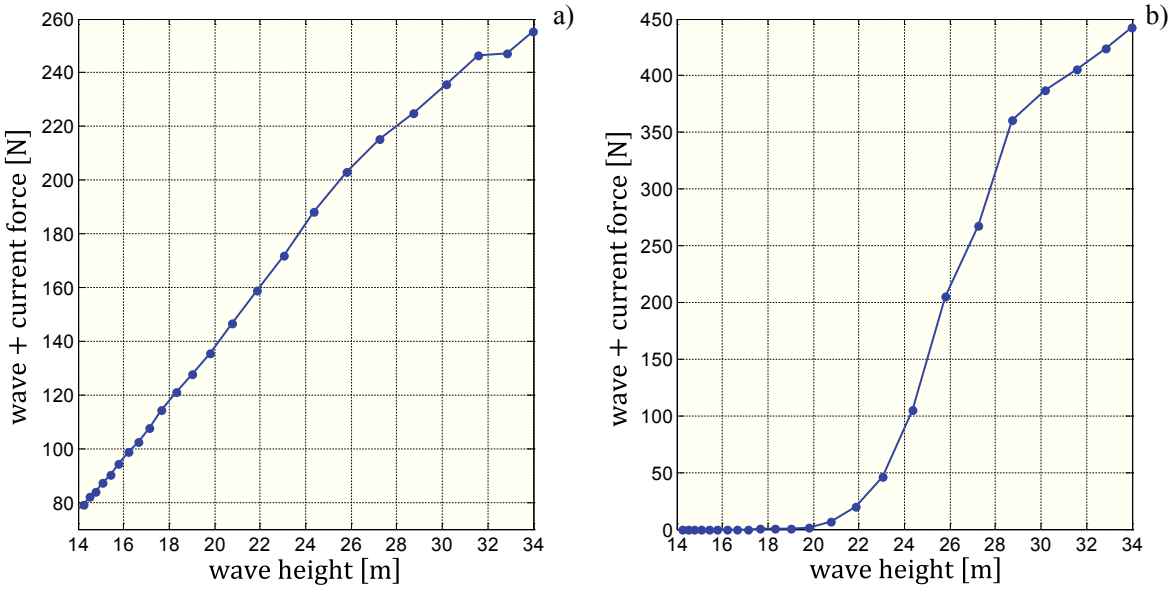

Figure 3.15: Horizontal component of wave-current load calculated at a) the node between elements 15-16 (see Figure 3.3) and b) the node between elements 24-27.

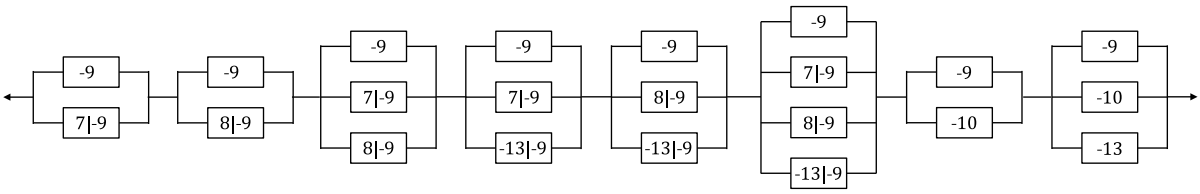

Figure 3.16: Minimal cut set representation of the system failure event for $\eta = 0.8$.

Table 3.7: Failure modes and corresponding reliability indexes for $\eta = 0.8$: a) Results provided by MSR performing FORM compared to MCS; and b) results provided by MSR performing SORM compared to MCS.

	Reliability Index		
Failure modes	MSR (FORM)	MCS (CoV = 3%)	Error %
$-9 \rightarrow 7$	3.0467	3.1018	1.78
$-9 \rightarrow 8$	3.0798	3.1347	1.75
$-9 \rightarrow (7,8)$	3.1728	3.2397	2.07
$-9 \rightarrow (7,-13)$	3.2381	3.3231	2.56
$-9 \rightarrow (8,-13)$	3.2460	3.3310	2.55
$-9 \rightarrow (7,8,-13)$	3.2658	3.3493	2.49
$(-9,-10)$	3.4201	3.4796	1.71
$(-9,-10,-13)$	3.5631	3.6419	2.16

a)

	Reliability Index		
Failure modes	MSR (SORM)	MCS (CoV = 3%)	Error %
$-9 \rightarrow 7$	3.0374	3.1018	2.08
$-9 \rightarrow 8$	3.0777	3.1347	1.82
$-9 \rightarrow (7,8)$	3.1669	3.2397	2.25
$-9 \rightarrow (7,-13)$	3.2516	3.3231	2.15
$-9 \rightarrow (8,-13)$	3.2606	3.3310	2.11
$-9 \rightarrow (7,8,-13)$	3.2795	3.3493	2.08
$(-9,-10)$	3.4494	3.4796	0.87
$(-9,-10,-13)$	3.5683	3.6419	2.02

b)

3.6 Conclusions

This chapter presents an efficient and accurate method for risk assessment of offshore structures. First, the problem of a jacket-type platform under an extreme sea state is considered. The structure is modelled as a truss and uncertainty affects the yield stress of the members, which are assumed to fail either in tension or compression. Environmental loading includes current-wave forces, self-weight, buoyancy forces and applied loads, in which the probability density function of the wave height is fitted by a generalized extreme value distribution, while the current speed and the drag and mass coefficients are assumed to be normally distributed. Then, a risk assessment framework recently developed for truss and frame structures is applied to an offshore structure. The main advantage of the approach is that the identification process of dominant failure modes is decoupled from the evaluation process of the probabilities of failure modes and the system event. As a result, the dominant failure modes of the jacket-type platform can be rapidly identified. For this purpose, a multi-point parallel search employing a genetic algorithm is used. Finally, the evaluation process is carried out by a multi-scale Matrix-based System Reliability (MSR) analysis, in which the statistical dependence among both components and failure modes is fully considered.

The accuracy and the efficiency of the proposed approach are successfully validated against crude Monte Carlo Simulation (MCS). In particular, the computational time and the number of iterations are 1-2 orders of magnitude less than those required by MCS. The effect of the post-buckling factor on structure-level failure probability is also investigated. As far as the post-failure behaviour moves away from the brittle zone (lower post-buckling factor) to the ductile zone (higher post-buckling factor) the redundancy level in the structure is enhanced and accordingly, the system reliability index increases. Moreover, while the computational time required by MCS varies exponentially with system reliability index, the time required by the proposed method is insensitive to this value.

Finally, the effect of nonlinearities in the wave-current loads on the accuracy of the results is analysed. When the wave height exceeds a certain value, even the top side of the structure (the deck) is involved in the calculation of the wave-current forces. As a consequence, a sharp nonlinear increase in wave-current forces is typically related to outer regions of the random variables space (where the wave height is higher). It follows that the probabilities estimated by MSR performing first-order reliability method (FORM) may be less accurate for failure modes that are less likely to occur. In some cases, a more accurate estimation of such failure probabilities can be obtained by coupling MSR with second-order reliability method (SORM).

In conclusion, the computational efficiency and accuracy arising from the capability to separate the failure mode identification from the probability evaluation processes first, and to rationally consider the statistical dependence among failure events then, make the proposed

approach particularly attractive to the offshore industry. Further research will investigate the applicability of this method to both design and planning of inspection, maintenance and repair strategies.

4 Simulation of the longitudinal tensile strength and damage accumulation in fibre-reinforced composites

In this chapter, system reliability theory is applied to the uncertainty quantification of the longitudinal tensile strength of fibre-reinforced composites. The damage accumulation and failure of this class of materials is governed by statistical size effects, which pose a challenge to use coupon-based experimental data for the design of large structures. In this respect, a Monte Carlo progressive failure analysis is proposed to evaluate the strength distributions of hierarchical fibre bundles, which are formed by grouping a predefined number (coordination number) of smaller-order bundles into a larger-order bundle. The present approach is firstly validated against a recent analytical model, which has been extensively validated against experimental results. Based on this model, hierarchical bundles are formed by grouping sub-bundles two by two (i.e., a coordination number equal to two is used), and their full strength distributions are derived based on given fibre-strength distribution and matrix shear-lag near fibre breaks. Furthermore, such a model allows the damage accumulation into clusters of fibre breaks to be analysed. In addition to providing the same results of the analytical model, the proposed numerical approach is also applied to higher coordination numbers, thus extending the analysis to more realistic load-sharing configurations and making this approach suitable for the stochastic analysis of fibre-reinforced composites and the associated size effects.

This chapter is organised as follows: Section 4.1 introduces the problem of size effects on the longitudinal tensile strength of fibre bundles. Then, a brief overview of the reference analytical model is presented in Section 4.2, providing the basis for the numerical implementation in Section 4.3. Results of the proposed numerical model are shown in Section 4.4, and pros and cons are discussed in Section 4.5. Finally, the main conclusions are drawn in Section 4.6.

4.1 Size effects

UniDirectional (UD) fibre-reinforced polymers (FRPs) are generally composed of millions of individual fibres all aligned in the same direction. Technical fibres, such as glass- and carbon-fibres, are characterised by micro-scale diameters ($4-7\ \mu m$), high tensile stiffness ($200-600\ GPa$), and high tensile strength ($3-7\ GPa$) (Pimenta, 2015). Nevertheless, they are usually very brittle, and their failure is governed by the statistics of defects. As a consequence, the fibre strength is a random quantity dependent on the size (length) of the fibre itself; longer fibres are associated to a higher percentage of defects and, therefore, to weaker strengths. From a reliability point of view, this is explained by the Weakest Link Theory (WLT) (Weibull, 1951), which states that chain of n elements withstands an external load only if all its elements survive the resulting stresses. This is mathematically expressed by Eq. (2.68), which is here rewritten as

$$P_f = 1 - P\left(\bigcap_{i=1}^{n}\{R_i - \sigma^{\infty} > 0\}\right) \tag{4.1}$$

where σ^{∞} is the remote applied stress, and R_i is the longitudinal tensile strength of the i-th fibre element. Let the random variables R_i be all statistically identical and independent, with $R_i = X_{\mathrm{U,r}}$, in which the subscript U indicates the uniform loading condition, and r indicates the reference length l_{r} of the element. Therefore, Eq. (4.1) becomes

$$P_f = 1 - \prod_{i=1}^{n} P\left(X_{\mathrm{U,r}} > \sigma^{\infty}\right) = 1 - \left[1 - P\left(X_{\mathrm{U,r}} \leq \sigma^{\infty}\right)\right]^{n} \tag{4.2}$$

Analogously to the notation used for the strength variables, the failure probabilities are denoted by $F_{\mathrm{U,r}}$ for the elements (length l_{r}) and $F_{\mathrm{U,n}}$ for the chain (length $l_{\mathrm{n}} = n \cdot l_{\mathrm{r}}$), so that Eq. (4.2) can be reformulated as

$$F_{\mathrm{U,n}}(\sigma^{\infty}) = 1 - \left[1 - F_{\mathrm{U,r}}(\sigma^{\infty})\right]^{l_{\mathrm{n}}/l_{\mathrm{r}}} \tag{4.3}$$

This is the expression of the WLT for length scaling of the individual fibre strength distribution. Figure 4.1 illustrates how the length scaling law operates for different ratios $l_{\mathrm{n}}/l_{\mathrm{r}}$. For any given distribution $F_{\mathrm{U,r}}$ (black curve), the output cumulative distribution function (CDF) of $F_{\mathrm{U,n}}$ shifts to lower strength values if $l_{\mathrm{n}_1} > l_{\mathrm{r}}$ (red curve); conversely, higher strength values are associated to shorter fibres, i.e. $l_{\mathrm{n}_2} < l_{\mathrm{r}}$ (green curve).

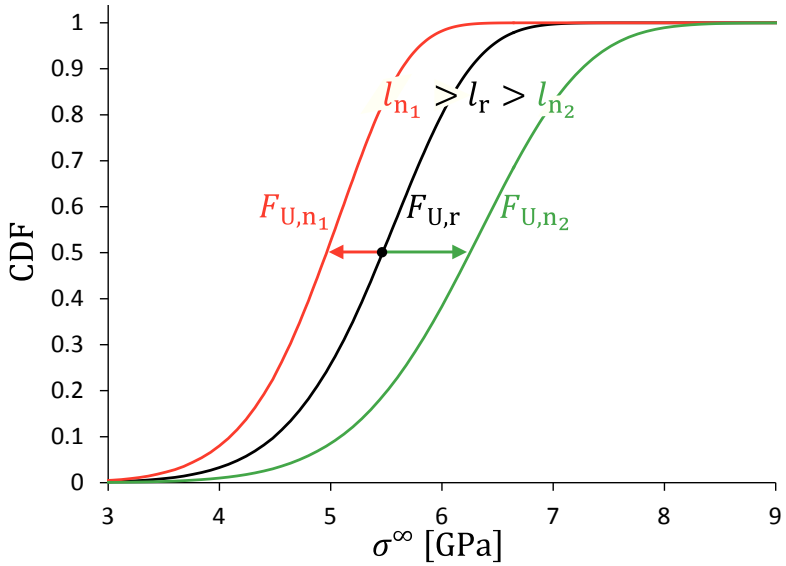

Figure 4.1: Size effects on the fibre-strength distributions.

The Weibull distribution (Weibull, 1951) is typically used to model the strength of brittle materials. In this case, the failure probability of a fibre under uniform stress σ^{∞} is

$$F_{U,n}(\sigma^{\infty}) = 1 - \exp\left[-\frac{l_n}{l_r}\left(\frac{\sigma^{\infty}}{\sigma_0}\right)^m\right] \tag{4.4}$$

where l_n is the fibre length, and m and σ_0 are respectively the shape (size independent) and scale (measured at the reference length l_r) parameters of the distribution. It should be noted that the Weibull distribution verifies Eq. (4.3), therefore Eq. (4.4) is consistent with the WLT.

At the FRP level, the presence of matrix and the load redistribution among parallel fibres result in a quasi-brittle failure. Micro-bundle (with 4 – 7 fibres) strengths have been measured by Beyerlein and Phoenix (1996) and Kazanci (2004), highlighting significant deviations from the Weibull model; in particular, some bundles resulted in higher mean strengths and lower variability than the single fibres. At the macroscopic scale (with thousands of fibres), Okabe and Takeda (2002) and Scott et al. (2011) observed several clusters of fibre breaks forming before global failure; moreover, both the mean value and the variability of strength decrease for larger specimens (Wisnom, 1999). All these observations are incompatible with the WLT applied directly to the single-fibre level (Bažant, 1999; Wisnom, 1999).

Hence, several modelling approaches have been suggested for the stochastic analysis of FRPs (Bažant, 1999; Wisnom, 1999). Fibre Bundle Models (FBMs) (Pradhan, Hansen & Chakrabarti, 2010) accurately represent the physics involved in longitudinal tensile failure and the associated size effects. This type of model focuses on calculating the strength distribution of a bundle of fibres with a given characteristic length, and the WLT is only used to scale the result for a longer chain of bundles (Curtin, 1991; Harlow & Phoenix, 1978a,b).

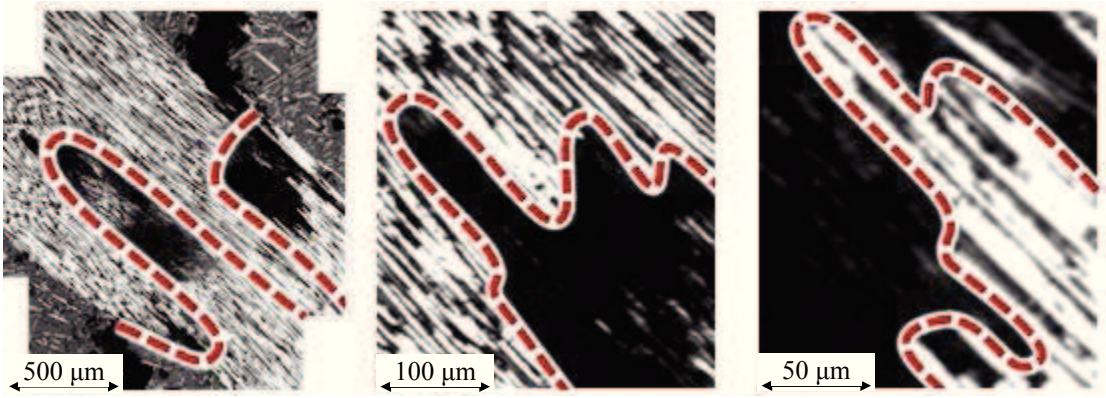

Figure 4.2: Fracture contours within a fibre bundle, at three different magnification levels (Pimenta et al., 2010).

In general, the complexity of FBMs increases with the number of fibres in the bundle's cross-section, and exact solutions are attainable for small bundles only. However, quasi-fractal fracture surfaces (i.e. fracture surfaces with similar contours at different magnification levels, see Figure 4.2) have been reported in UD laminas and fibre bundles (Laffan et al., 2010; Pimenta et al., 2010), providing experimental evidence for a hierarchical failure process. Consequently, Pimenta and Pinho (2013) recently proposed a hierarchical scaling law relating the strength distributions of consecutive bundle levels, in which the number of fibres scales by a power of two (i.e., a *coordination number* $c = 2$ is used; see Figure 4.3a).

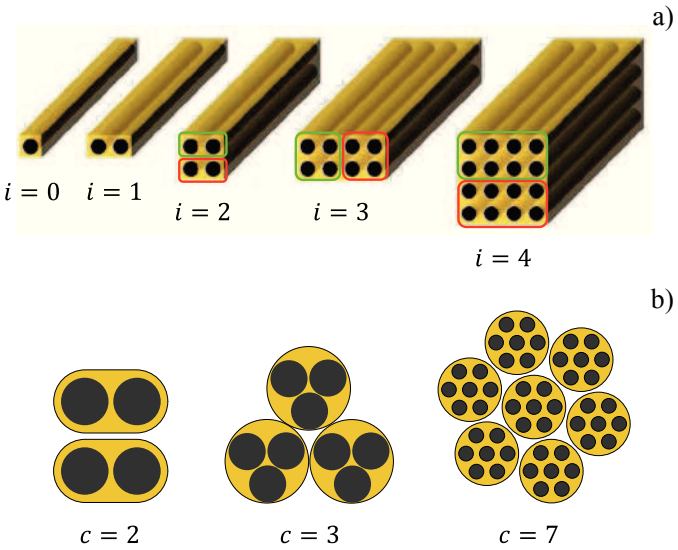

Figure 4.3: a) First 4 bundle levels with coordination number $c = 2$; b) Fibre arrangements for different coordination numbers.

Despite this approach allows a fast calculation of bundle strength distributions, imposing a coordination number c equal to 2 results in too high stress concentrations in the proximity of fibre breaks. In order to improve the model and to investigate the physics at the

base of the damage accumulation and failure processes of UD composites, the hierarchical approach is here generalised to higher values of c (see Figure 4.3b), thus extending the analysis to more realistic load-sharing configurations (of particular interest is the case of $c = 7$, which better represents the actual disposition of fibres in the bundle cross-section).

However, the number of possible bundle failure sequences becomes extremely high for $c > 2$, thus preventing the bundle strength distributions to be evaluated analytically. A new numerical approach is then proposed, where the failure events are simulated through a discrete representation of hierarchical bundles, and their distributions are evaluated by means of a Monte Carlo progressive failure analysis.

4.2 Overview of the hierarchical analytical model for composite fibre bundles

4.2.1 Hierarchical scaling law for the bundle strengths

As shown in Figure 4.3a, the analytical model (Pimenta & Pinho, 2013) assumes that hierarchical bundles are formed by pairing two individual fibres (level-[0]) into a level-[1] bundle, and sequentially grouping two level-$[i]$ bundles into one level-$[i+1]$ bundle.

Consider first a level-[1] bundle composed by two level-[0] fibres, A and B, and assume the far-field stress σ^{∞} progressively increasing until a first break occurs in the middle of fibre A (see Figure 4.4). Based on a perfectly-plastic shear-lag model, the failed fibre A recovers the remote stress σ^{∞} within the level-[0] *effective recovery length* (Pimenta & Pinho, 2013), i.e.

$$l_{\mathrm{e}}^{[0]}(\sigma^{\infty}) = 2 \cdot \frac{A^{\mathrm{f}}}{C^{[0]} \cdot \tau_{\mathrm{SL}}} \cdot \sigma^{\infty} \tag{4.5}$$

where A^{f} is the cross-sectional area of a single fibre, τ_{SL} is the matrix/interface yield stress in shear, and $C^{[0]}$ is the perimeter of the level-[0] shear-lag boundary, at which shear stresses can be transferred. From equilibrium, a linear stress concentration applies to fibre B, which reaches a stress concentration factor $k = 2$ in the proximity of the fibre break ($x = 0$).

Bundle failure requires fibre B to fail nearby the break in fibre A, so as to promote complete yielding of the matrix/interface between the two fibre-breaks (see Figure 4.5). Therefore, once fibre A fails, the level-[1] *control region* is defined as the region where a break in fibre B would lead to bundle failure, i.e.

$$l_{\mathrm{c}}^{[1]}(\sigma^{\infty}) = 2 \cdot l_{\mathrm{e}}^{[0]}(\sigma^{\infty}) \tag{4.6}$$

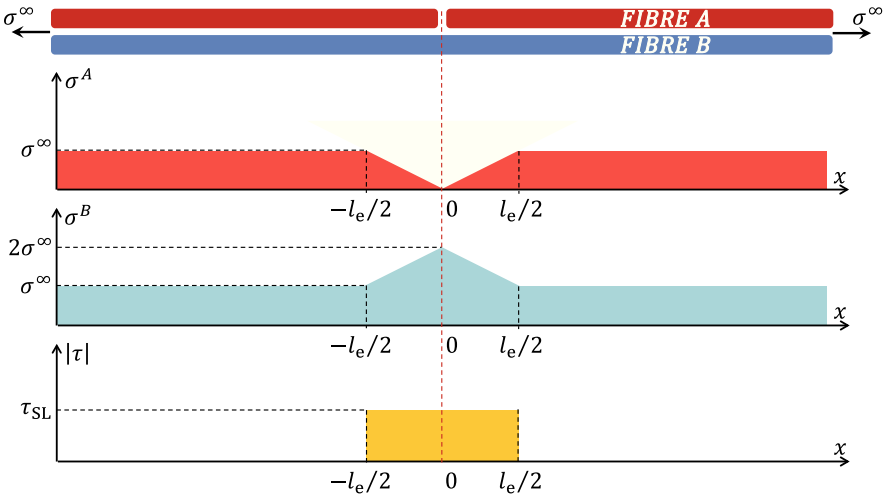

Figure 4.4: A first break occurs in the middle of fibre A, the matrix yields plastically, and a linear stress concentration applies to fibre B (Pimenta & Pinho, 2013).

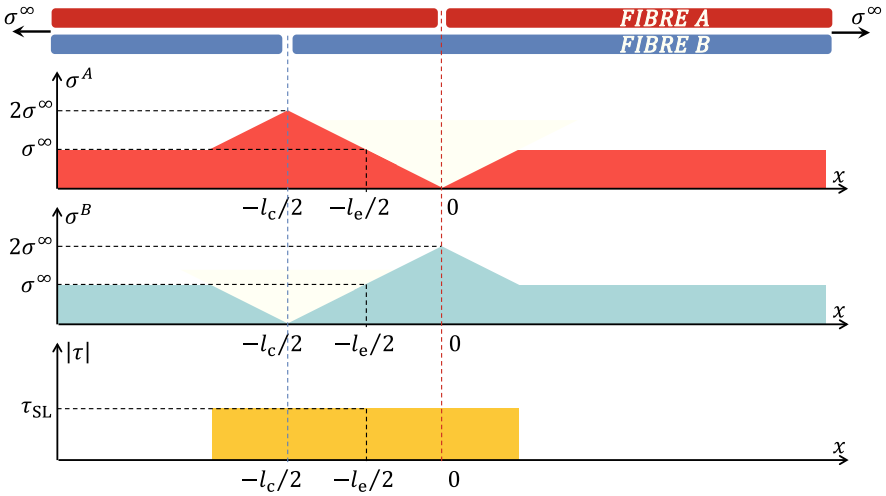

Figure 4.5: Definition of the critical distance between fibre breaks: the bundle fails if fibre B breaks at a distance smaller than $l_c/2 = l_e$ from the break in fibre A (Pimenta & Pinho, 2013).

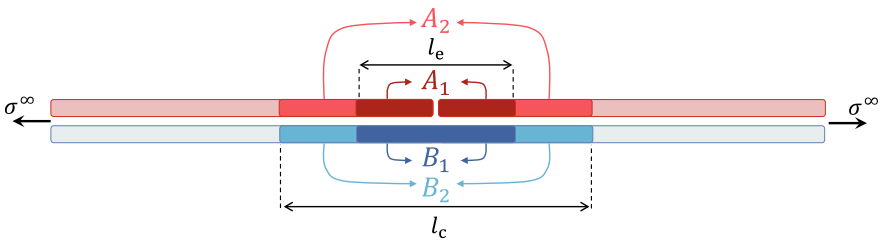

Figure 4.6: Definition of the control region and fibre segments in a level-[1] bundle (Pimenta & Pinho, 2013).

As illustrated in Figure 4.6, the control region is partitioned into 4 segments (A_1, A_2, B_1 and B_2) of equal length $l_{\mathrm{e}}^{[0]}$, and two assumptions are made:

$A(i)$ the bundle is represented by a chain of independent control regions (to avoid bundle-end effects by shifting the first fibre-break to the centre of the control region);

$A(ii)$ within a control region, each fibre can fail only once (to guarantee simple stress fields as those presented in Figure 4.5).

Based on the assumptions above, the list of sequences of events leading to bundle failure is defined as follows:

E_1: failure of segment A_1 and unstable failure (with no increase of the far-field stress) of segment B_1 due to stress concentrations;

E_2: failure of segment A_1 and stable failure (after incrementing σ^{∞}) of segment B_1 due to stress concentrations;

E_3: failure of segment A_1 and stable failure of segment B_2 due to independent fibre flaws (including growth and coalescence of matrix damage between fibre breaks).

Therefore, the total failure probability of the bundle is given by the union of events E_1, E_2 and E_3, which yields the following expression for the level-[1] bundle survival probability under uniform stress σ^{∞} within the control length $l_{\mathrm{c}}^{[1]}$ (see Appendix D):

$$S_{\mathrm{U,c}}^{[1]}(\sigma^{\infty}) = S_{\mathrm{U,e}}^{[0]}(\sigma^{\infty})^4 + 2 \cdot \left[1 - S_{\mathrm{U,e}}^{[0]}(\sigma^{\infty})^2\right] \cdot S_{\mathrm{U,e}}^{[0]}(\sigma^{\infty}) \cdot S_{\mathrm{K,e}}^{[0]}(\sigma^{\infty}) \tag{4.7}$$

where $S_{\mathrm{U,e}}^{[0]}$ and $S_{\mathrm{K,e}}^{[0]}$ are the survival probability of a single-fibre segment of length $l_{\mathrm{e}}^{[0]}$, and the subscripts U and K respectively refer to a uniform stress loading (σ^{∞}) and a linear stress profile with concentration factor $k = 2$. The level-[1] bundle strength distribution is then obtained as the complement of the level-[1] bundle survival probability, i.e. $F_{\mathrm{U,c}}^{[1]}(\sigma^{\infty}) = 1 - S_{\mathrm{U,c}}^{[1]}(\sigma^{\infty})$.

Eq. (4.7) relates the strength distribution of the level-[1] bundle to that of a single fibre, for which a Weibull distribution is used in (Pimenta & Pinho, 2013). Assuming a hierarchical failure process, Eq. (4.7) is then extended to any bundle level, so that the following recursive formula is provided:

$$S_{\mathrm{U,c}}^{[i+1]}(\sigma^{\infty}) = S_{\mathrm{U,e}}^{[i]}(\sigma^{\infty})^4 + 2 \cdot \left[1 - S_{\mathrm{U,e}}^{[i]}(\sigma^{\infty})^2\right] \cdot S_{\mathrm{U,e}}^{[i]}(\sigma^{\infty}) \cdot S_{\mathrm{K,e}}^{[i]}(\sigma^{\infty}) \tag{4.8}$$

in which the control length and the recovery length scale hierarchically too:

$$l_{\mathrm{e}}^{[i]}(\sigma^{\infty}) = 2 \cdot \frac{n^{[i]} \cdot A^{\mathrm{f}}}{C^{[i]} \cdot \tau_{\mathrm{SL}}} \cdot \sigma^{\infty} \ , \qquad l_{\mathrm{c}}^{[i+1]}(\sigma^{\infty}) = 2 \cdot l_{\mathrm{e}}^{[i]}(\sigma^{\infty}) \tag{4.9}$$

where $n^{[i]} = 2^i$ is the number fibres in the level-$[i]$ bundle, and $C^{[i]}$ is the shear-lag perimeter (see Figure 4.7), which is defined as (Pimenta & Pinho, 2013),

$$C^{[i]} = 3\pi\phi^{\mathrm{f}} + 4\left[\left(\sqrt{n^{[i]}} - 1\right)\left(\frac{\sqrt{\pi}}{2\sqrt{V^{\mathrm{f}}}} - 1\right) + \left(\sqrt{n^{[i]}} - 2\right)\frac{\pi\phi^{\mathrm{f}}}{2}\right] \tag{4.10}$$

in which ϕ^{f} indicates the fibre diameter, and V^{f} the fibre volume fraction.

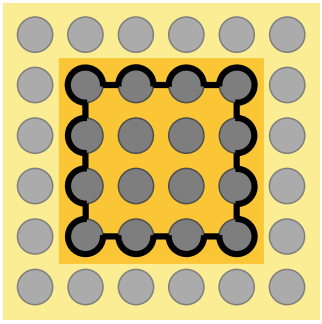

Figure 4.7: Shear-lag boundary for square fibre arrangement (Pimenta & Pinho, 2013).

Finally, the WLT can be used within any bundle level to scale the survival probability $S_{\mathrm{U,c}}^{[i]}$ to the reference length of the bundle, i.e.

$$F_{\mathrm{U,r}}^{[i]}(\sigma^{\infty}) = 1 - \left[1 - F_{\mathrm{U,c}}^{[i]}(\sigma^{\infty})\right]^{l_{\mathrm{r}}/l_{\mathrm{c}}^{[i]}} \iff S_{\mathrm{U,r}}^{[i]}(\sigma^{\infty}) = \left[S_{\mathrm{U,c}}^{[i]}(\sigma^{\infty})\right]^{l_{\mathrm{r}}/l_{\mathrm{c}}^{[i]}} \tag{4.11}$$

4.2.2 Accumulation and clustering of fibre breaks

From the last expression in Eq. (4.11), it can be noticed that the first term on the right-hand side of Eq. (4.8) corresponds to the WLT applied to the previous-level bundle. In other words, in the brittle domain, a level-$[i+1]$ bundle of length $l_{\mathrm{c}}^{[i+1]}$ behaves identically to a level-$[i]$ bundle of length $4 \cdot l_{\mathrm{e}}^{[i]}$. During brittle failure, only uniform stress applies to the bundle, so that the subscript $\mathcal{U}$ is used to indicate the brittle term of Eq. (4.8), i.e.

$$S_{\mathcal{U}}^{[i+1]}(\sigma^{\infty}) = S_{\mathrm{U,e}}^{[i]}(\sigma^{\infty})^4 \tag{4.12}$$

Conversely, the second term of Eq. (4.8) accounts for the non-brittle behaviour, i.e. the survivability of the level-$[i+1]$ bundle after one of the two level-$[i]$ bundles fails (see Figure 4.8). In this case, a linear stress concentration applies to the surviving level-$[i]$ bundle, so that the subscript $\mathcal{K}$ is used to indicate the non-brittle term of Eq. (4.8), i.e.

$$S_{\mathcal{K}}^{[i+1]}(\sigma^{\infty}) = 2 \cdot \left[1 - S_{\mathrm{U,e}}^{[i]}(\sigma^{\infty})^2\right] \cdot S_{\mathrm{U,e}}^{[i]}(\sigma^{\infty}) \cdot S_{\mathrm{K,e}}^{[i]}(\sigma^{\infty}) \tag{4.13}$$

Eq. (4.13) can then be used to determine the frequency of occurrence of level-$[i]$ clusters, which are defined considering every occurrence of a failed level-$[i]$ bundle with a surviving level-$[i]$ neighbour (see Figure 4.8). In particular, the density of level-$[i]$ clusters in any bundle of level greater than or equal to $[i+1]$ is given by (Pimenta, 2014)

$$\hat{\rho}_{\mathrm{clust}}^{[i]}(\sigma^{\infty}) = \frac{S_{\mathcal{K}}^{[i+1]}(\sigma^{\infty})}{V_{\mathrm{c}}^{[i+1]}(\sigma^{\infty})} \quad , \qquad V_{\mathrm{c}}^{[i+1]}(\sigma^{\infty}) = n^{[i+1]} \cdot A^{\mathrm{f}} \cdot l_{\mathrm{c}}^{[i+1]}(\sigma^{\infty}) \tag{4.14}$$

where $V_{\mathrm{c}}^{[i+1]}$ represents the control volume of the level-$[i+1]$ bundle.

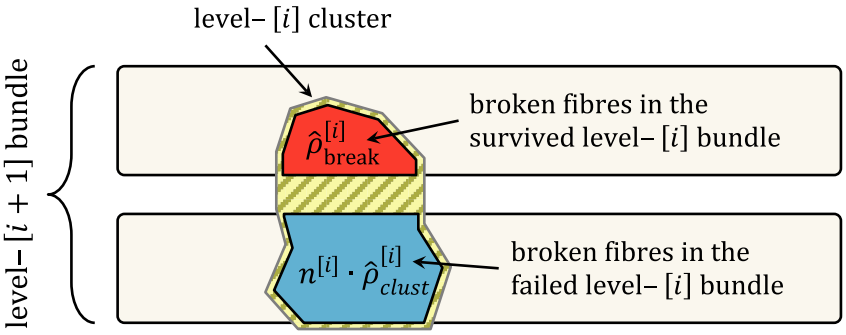

Figure 4.8: Damaged level-$[i+1]$ bundle of length $l_{\mathrm{c}}^{[i+1]}$, in which only one of the two level-$[i]$ bundles withstands the external load.

From the definition of clusters given above, the surviving level-$[i]$ bundle may still present broken fibres, whose density is denoted by $\hat{\rho}_{\mathrm{break}}^{[i]}$. With reference to Figure 4.8, the following recursive formula is provided

$$\hat{\rho}_{\mathrm{break}}^{[i+1]}(\sigma^{\infty}) = n^{[i]} \cdot \hat{\rho}_{\mathrm{clust}}^{[i]}(\sigma^{\infty}) + \hat{\rho}_{\mathrm{break}}^{[i]}(\sigma^{\infty}) \tag{4.15}$$

in which the first term represents the contribution of the broken level-$[i]$ bundle (blu area), and the second term is the contribution of the survived level-$[i]$ bundle (red area).

The total number of broken level-$[j]$ clusters and fibre breaks in a level-$[i]$ bundle of length l_{r} can be defined as

$$\widehat{N}_{\mathrm{clust}}^{[j|i]}(\sigma^{\infty}) = \hat{\rho}_{\mathrm{clust}}^{[j]}(\sigma^{\infty}) \cdot V_{\mathrm{r}}^{[i]} \quad , \qquad \forall j \in \{0, \dots, i-1\} \tag{4.16}$$

$$\widehat{N}_{\mathrm{break}}^{[i]}(\sigma^{\infty}) = \hat{\rho}_{\mathrm{break}}^{[i]}(\sigma^{\infty}) \cdot V_{\mathrm{r}}^{[i]} \quad , \qquad \text{where } V_{\mathrm{r}}^{[i]} = n^{[i]} \cdot A^{\mathrm{f}} \cdot l_{\mathrm{r}} \tag{4.17}$$

Finally, the largest cluster in a level-$[i]$ bundle is defined as the largest level $\hat{\jmath}^{[i]}_{\text{clust,max}}$ which guaranties a pre-established minimum value of $\widehat{N}^{[j|i]}_{\text{clust}}$, e.g.

$$\hat{\jmath}^{[i]}_{\text{clust,max}}(\sigma^{\infty}) = \max\left\{j \in \{0, \dots, i-1\} : \widehat{N}^{[j|i]}_{\text{clust}}(\sigma^{\infty}) \geq 0.5\right\} \tag{4.18}$$

4.3 Numerical implementation

4.3.1 Simulation of failure events in a bundle with 2 fibres

The analytical hierarchical model introduced in the previous section is here reformulated using a discrete representation of fibres and bundles. Consider first a level-[1] bundle of length $L^{[1]}$ and coordination number $c = 2$ (i.e. a 2-fibres bundle), in which each fibre is discretised into a large number of level-[0] elements of equal length $\Delta^{[0]}$. A value of strength is then generated for each fibre-element (Figure 4.9a), based on a random sampling of level-[0] strength distribution. A Weibull distribution is assumed for the individual fibres (for consistency with Pimenta and Pinho's (2013) analytical model); being l_{r} the reference length at which the Weibull parameters were measured, the distribution used in the model is then scaled to the element length $\Delta^{[0]}$ by applying the WLT,

$$F^{[0]}_{\text{U},\Delta^{[0]}}(\sigma^{\infty}) = 1 - \left[1 - F^{[0]}_{\text{U},l_{\text{r}}}(\sigma^{\infty})\right]^{\Delta^{[0]}/l_{\text{r}}} \tag{4.19}$$

where $F^{[0]}_{\text{U},l_{\text{r}}}$ and $F^{[0]}_{\text{U},\Delta^{[0]}}$ denote the Weibull distribution at length l_{r} and $\Delta^{[0]}$, respectively. Finally, the element strengths are generated by inverse transform sampling method (Devroye, 1986), applied to the level-[0] strength distribution, $F^{[0]}_{\text{U},\Delta^{[0]}}$.

Figure 4.9a illustrates a situation where the applied stress σ^{∞} overcomes the strength of elements 6 and 8 of fibre A, and of element 15 of fibre B, thus leading to local failures (highlighted in red colour). The corresponding stress field is shown in Figure 4.9b, which satisfies the equilibrium equation

$$\sigma_{A,j} + \sigma_{B,j} = 2\sigma^{\infty} \tag{4.20}$$

where the stresses $\sigma_{A,j}$ and $\sigma_{B,j}$ are evaluated at the centre of the j-th element of fibre A and B, respectively.

As shown in Figure 4.9b, the resulting stress fields can be more complex than those assumed in the analytical model (Figure 4.5). This is because the numerical implementation does not involve assumptions $A(i)$ and $A(ii)$, and the recovery regions can be here defined by superimposition of multiple stress-recovery fields (e.g., recovery region 1 in Figure 4.9b).

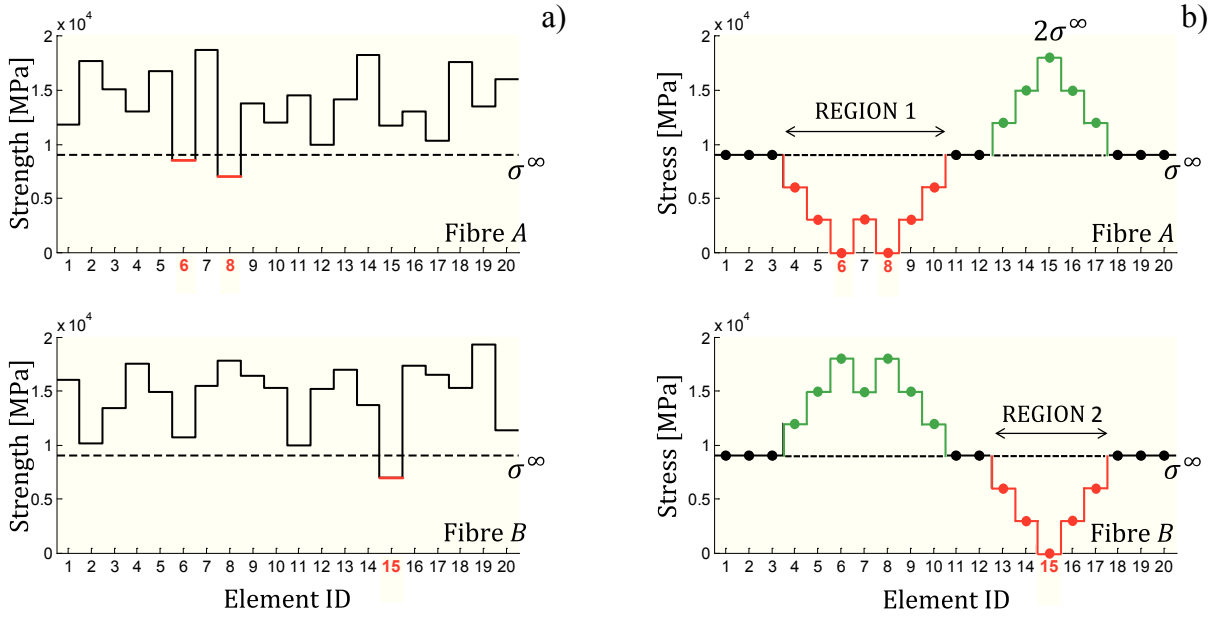

Figure 4.9: a) Elements 6 and 8 of fibre A and element 15 of fibre B fail under the uniform stress σ^∞; b) Resulting stress fields with recovery regions in red and stress concentrations in green.

However, the proposed implementation preserves the basic sequences of events leading to bundle failure, i.e. E_1, E_2 and E_3 defined in Section 4.2.1. This result is achieved by means of a progressive failure analysis, where the far-field stress σ^∞ is increased starting from the strength value of the weakest element (at which the first local failure occurs), up to the termination of the analysis once a global failure of the bundle is detected (see Figure 4.10 - Figure 4.12). Global failures occur when a recovery region in one fibre overlaps at least one recovery region in the other fibre, so that the equilibrium Eq. (4.20) cannot be satisfied. At that point, the value of the far-field stress σ^∞ is stored as an outcome of the stochastic level-[1] bundle strength, $X^{[1]}_{\mathrm{U},L^{[1]}}$. The corresponding distribution $F^{[1]}_{\mathrm{U},L^{[1]}}$ is obtained by a Monte Carlo analysis, repeating the progressive failure analysis N $(= 10^6)$ times, each time randomly sampling the element strengths from the given individual fibre strength distribution.

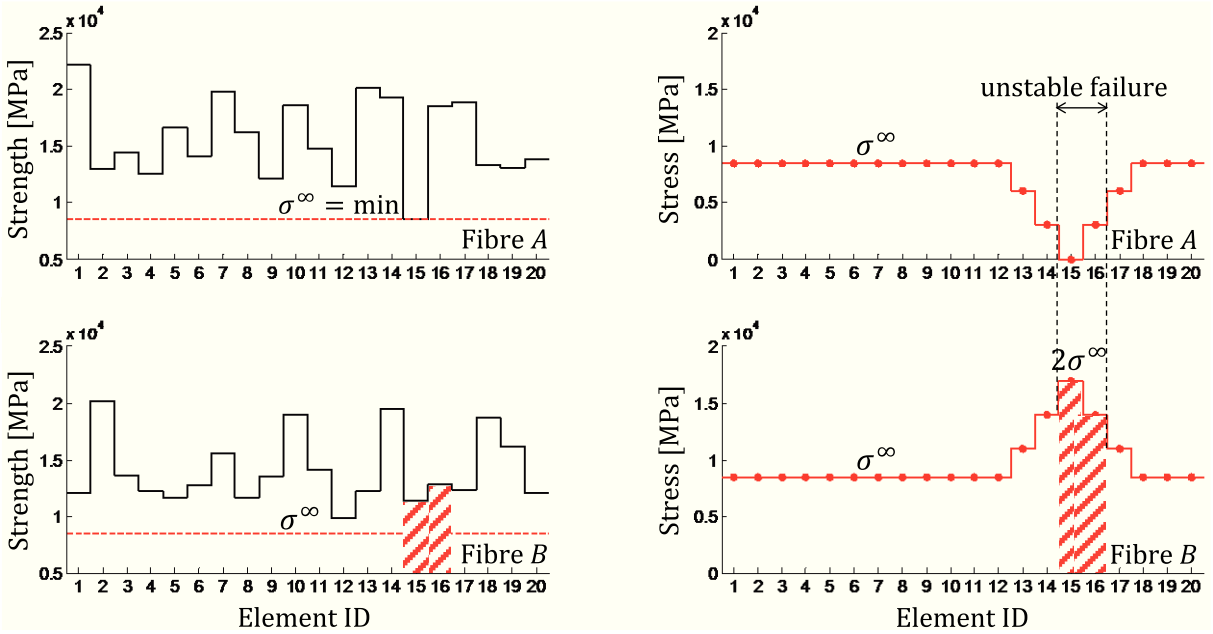

Figure 4.10: Unstable failure (event E_1); the level-[1] bundle fails at the first iteration of the progressive failure analysis when σ^∞ is equal to the strength value of the weakest element (i.e., element 15 of fibre A: after its failure, fibre B does not survive the stress concentrations in elements 15 and 16). Note the different values of strength and stress in the vertical axes.

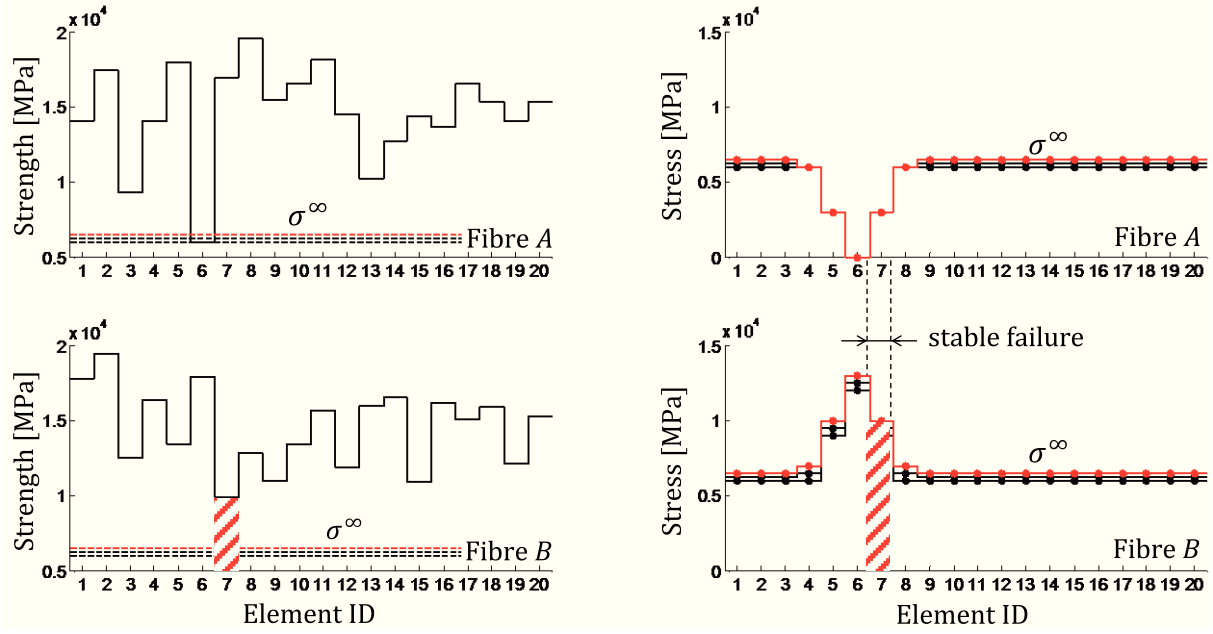

Figure 4.11: Stable failure (event E_2); the bundle fails after three iterations (the last iteration is highlighted in red colour). After element 6 of fibre A fails, fibre B survives the stress concentrations until σ^∞ reaches the strength of element 7 of fibre B. Note the different values of strength and stress in the vertical axes.

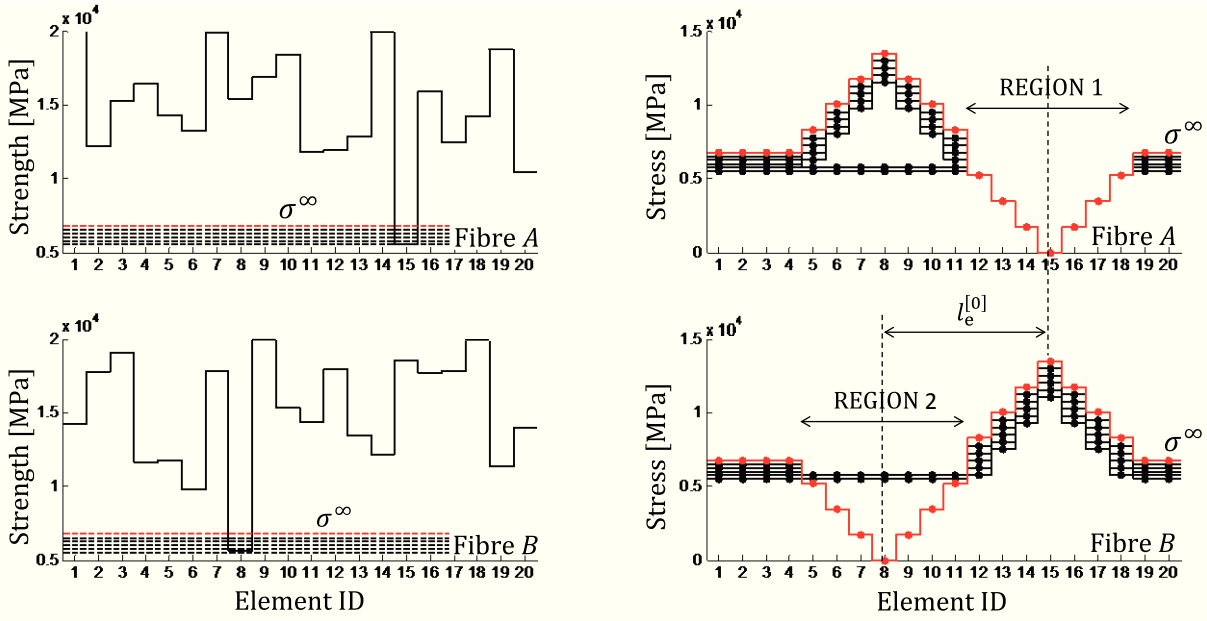

Figure 4.12: Stable failure (event E_3); the bundle fails due to growth and coalescence of the recovery regions between two previously formed breaks (in element 15 of fibre A and element 8 of fibre B). Note the different values of strength and stress in the vertical axes.

4.3.2 Simulation of larger bundles and asymptotic analysis of the strength distribution

The resulting level-[1] strength distribution is subsequently used to sample the strengths of level-[1] elements in the simulation of a level-[2] bundle (Figure 4.13). As in the previous level, the WLT is used for length scaling, so that the level-[1] bundle distribution can be evaluated at the element length $\Delta^{[1]}$:

$$F^{[1]}_{\mathrm{U},\Delta^{[1]}}(\sigma^{\infty}) = 1 - \left[1 - F^{[1]}_{\mathrm{U},L^{[1]}}(\sigma^{\infty})\right]^{\Delta^{[1]}/L^{[1]}} \tag{4.21}$$

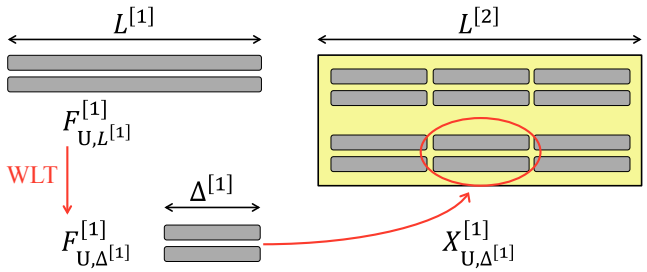

Figure 4.13: The WLT is applied to scale the bundle distribution from the full level-[1] bundle length ($L^{[1]}$) to the level-[1] element length ($\Delta^{[i]}$), so that the level-[1] element strengths can be sampled for the analysis of the level-[2] bundle.

However, the accuracy of $F^{[1]}_{\mathrm{U},L^{[1]}}$ is limited by the finite number of Monte Carlo analyses (N), as the right tail of $F^{[1]}_{\mathrm{U},L^{[1]}}$ above the $(1-1/N)$-th quantile is unavoidably rounded up to 1. Consequently, the small ratio $\Delta^{[1]}/L^{[1]}$ in Eq. (4.21) leads to the complete loss of a large portion of $F^{[1]}_{\mathrm{U},\Delta^{[1]}}$ (segment A-C in Figure 4.14), making it impossible to sample values for the element strength $X^{[1]}_{\mathrm{U},\Delta^{[1]}}$.

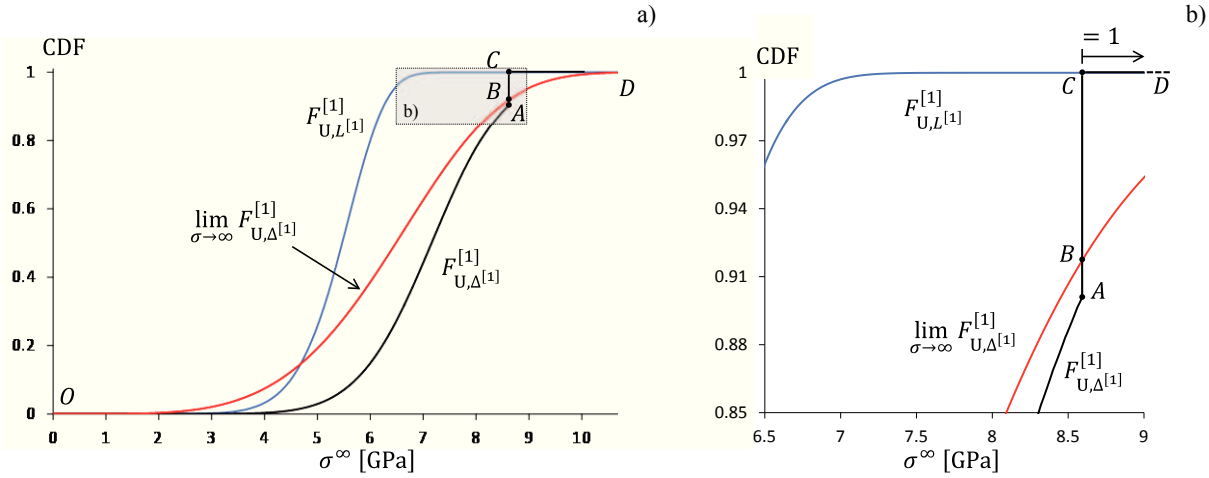

Figure 4.14: a) The limited number of Monte Carlo analyses rounds up to 1 the right tail of both the bundle strength ($F^{[1]}_{\mathrm{U},L^{[1]}}$, blue curve) and the element strength ($F^{[1]}_{\mathrm{U},\Delta^{[1]}}$, black curve) distributions; the latter is fitted with the asymptotic distribution ($\lim_{\sigma^{\infty}\to\infty} F^{[i]}_{\mathrm{U},\Delta^{[i]}}(\sigma^{\infty})$, red curve) provided by the WLT applied to the previous level bundle (Eq. (4.23)); b) region from plot a) highlighted.

This problem is circumvented by means of an asymptotic approximation of the bundle strength distributions. Pimenta and Pinho (2013) proved that if the individual fibre strength follows a Weibull distribution, then the Right Tail Asymptote (RTA) of any bundle strength distribution corresponds to the WLT applied to the single-fibre level, i.e.

$$\lim_{\sigma^{\infty}\to\infty} F^{[i]}_{\mathrm{U},\Delta^{[i]}}(\sigma^{\infty}) = 1-\left[1-F^{[0]}_{\mathrm{U},\Delta^{[i]}}(\sigma^{\infty})\right]^{c^i} \tag{4.22}$$

where c^i is the number of individual fibres in the level-$[i]$ bundle (being c the coordination number). Therefore, a level-$[i]$ bundle behaves asymptotically like an individual fibre (series system) with length c^i times the bundle length (see Figure 4.15). Moreover, since the Weibull distribution is scale-invariant, the RTA defined above is still a Weibull distribution.

However, it can be shown that as the bundle size increases (i.e., large i and/or large c), these asymptotes are valid for progressively more reduced tails (Pimenta & Pinho, 2013). A modification to the asymptotic analysis is then needed, providing asymptotes that are suitable for the fitting of the bundle strength distributions even at the macroscopic scale.

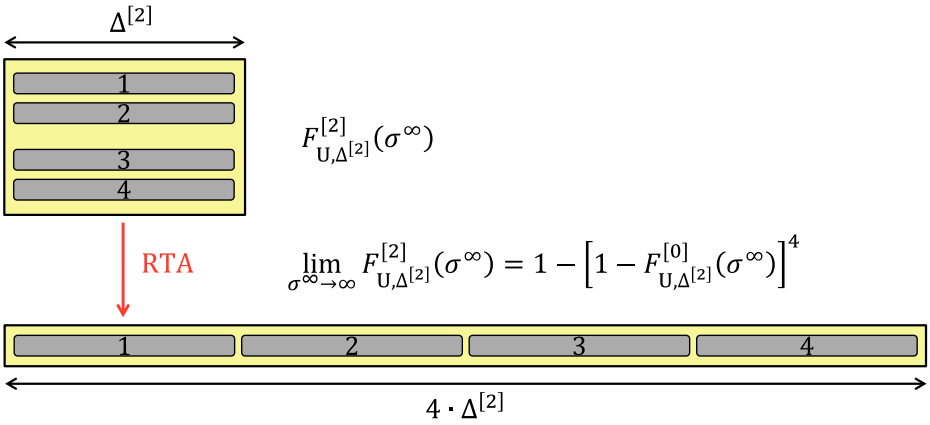

Figure 4.15: WLT applied to the single-fibre level (case for $i = c = 2$).

Since the right tail of any strength distribution falls into the domain of large stresses σ^{∞}, its shape is governed by unstable bundle failure due to stress concentrations (i.e., event E_1). In other words, the RTA of the level-$[i]$ bundle is determined by the strength of its weakest sub-bundle of level $[i-1]$. Such a consideration is consistent with the WLT applied to the previous-level bundle, so that the following model of the RTA is here proposed:

$$\lim_{\sigma^{\infty}\to\infty} F^{[i]}_{\mathrm{U},\Delta^{[i]}}(\sigma^{\infty}) = 1 - \left[1 - F^{[i-1]}_{\mathrm{U},\Delta^{[i]}}(\sigma^{\infty})\right]^{c} \tag{4.23}$$

The geometrical interpretation of Eq. (4.23) is illustrated in Figure 4.16, in which the asymptotic behaviour of a level-[2] bundle is expressed by the series of its sub-bundles of level [1].

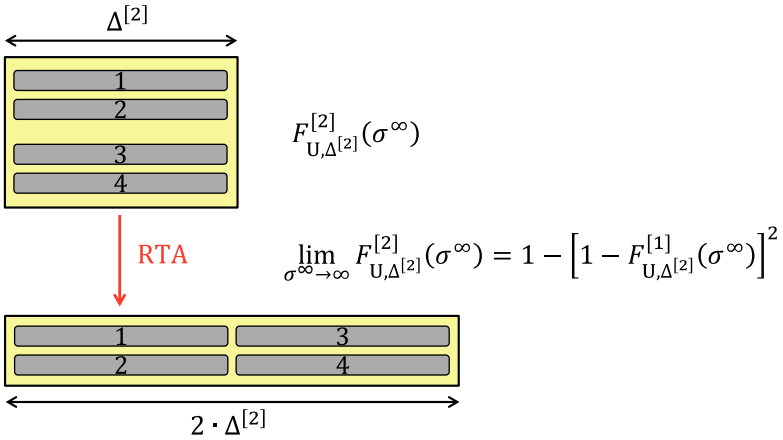

Figure 4.16: WLT applied to the previous-level bundle (case for $i = c = 2$).

Eq. (4.23) is used to fit $F^{[1]}_{\mathrm{U},\Delta^{[1]}}$ (by letting $i = 1$, and $c = 2$ in this particular case), which is then defined by the curve *O-A-B-D* (Figure 4.14). Finally, a tolerance is established for the residual gap *A-B*, which can be further reduced by increasing the ratio $\Delta^{[1]}/L^{[1]}$ to a value closer to unity.

The difference between the two asymptotic models is shown in the Weibull plot of Figure 4.17, where the Weibull distributions are represented by straight lines. The data relative to the first 3 levels are taken from the results that will be presented in Section 4.4, assuming $\Delta^{[i]} = 0.1$ mm, $i = 1, 2$ and 3.

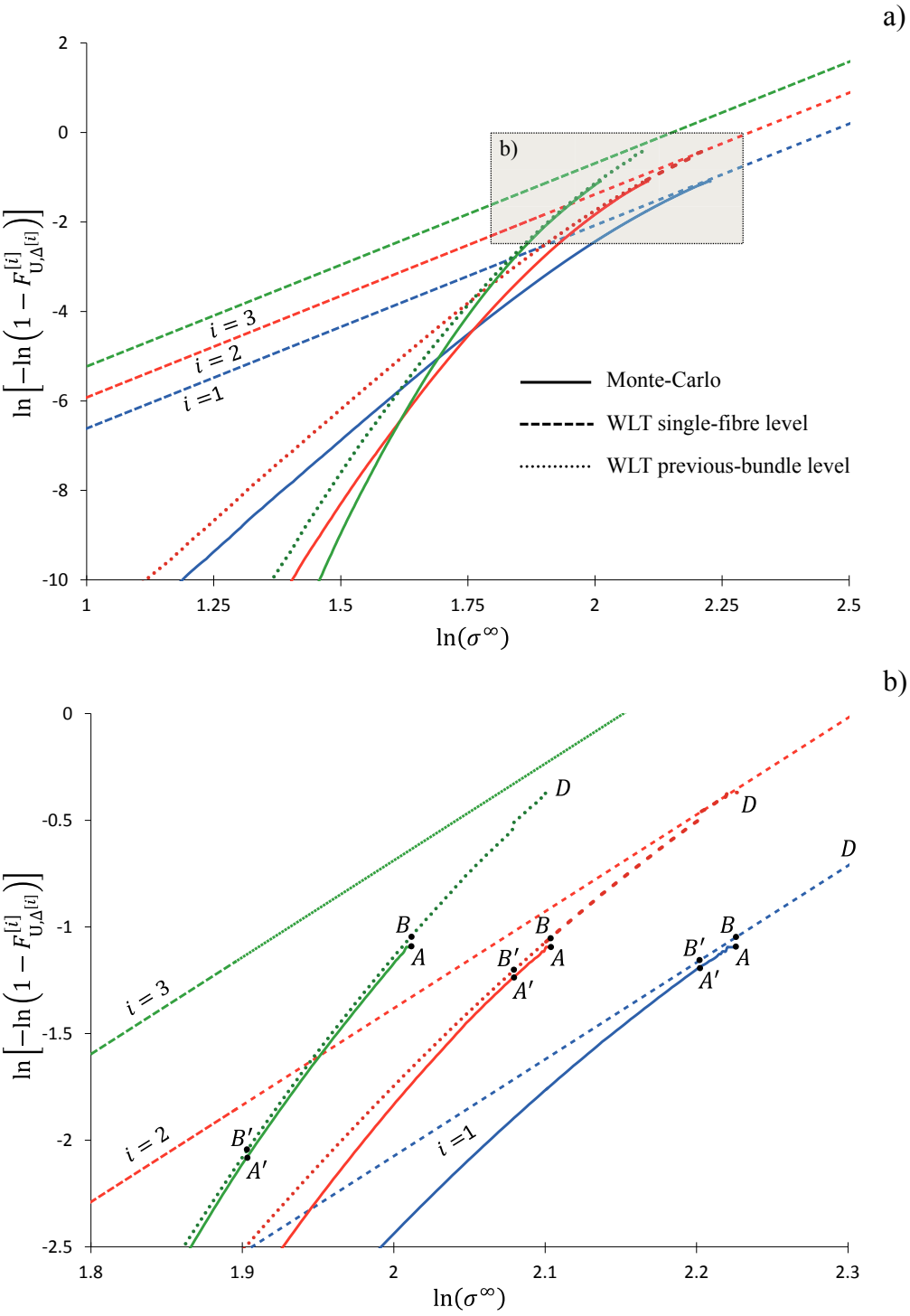

Figure 4.17: a) Asymptotic analysis of the first 3 levels using the WLT applied to the single-fibre level (dashed lines) and to the previous-bundle level (dotted lines); b) region from plot a) highlighted.

At level [1] (blue curves), the previous-bundle level corresponds to level [0] (i.e., the single-fibre level), so that both Eq. (4.22) and Eq. (4.23) provide the same RTA (dashed blue line). As shown in Figure 4.17b, numerical errors affect the last portion of $F^{[1]}_{\mathrm{U},\Delta^{[1]}}$ (solid blue line) before it is rounded up to 1 (point A). As a consequence, the fitting point is anticipated from A to A', where A' is the first point of $F^{[1]}_{\mathrm{U},\Delta^{[1]}}$ such that the vertical segment $A'B'$ satisfies the pre-established tolerance on the residual gap (e.g., 0.03). In this way, the fitted curve O-A-B-D is replaced by the more accurate curve O-A'-B'-D.

This fitting procedure is extended to higher levels (i.e., $i \geq 2$), at which the RTAs defined by Eq. (4.23) (dotted lines) depart from the Weibull distribution. It should be noted the distance between A and the Weibull asymptote (dashed lines) increases at higher levels, thereby preventing $F^{[i]}_{\mathrm{U},\Delta^{[i]}}$ to be fitted using Eq. (4.22). Conversely, the fitting point A' is progressively anticipated, suggesting full convergence of high level distributions to the WLT applied to the previous-bundle level. This fact will be proved in Section 4.4 for $i \geq 5$.

4.3.3 Extension of the numerical model to higher coordination numbers

Figure 4.18a illustrates the case of a level-[1] bundle with coordination number $c = 3$, where local failures affect elements 4 and 15 of fibre A, elements 8 and 12 of fibre B, and element 14 of fibre C. Figure 4.18b shows the corresponding stress field, which is calculated assuming the stress concentration to be equally distributed among intact elements. Therefore, indicating with $\sigma_{i,j}$ the value of stress evaluated at the j-th element of the i-th fibre it can be shown that

$$\sigma_{i,j} = \begin{cases} \left(\dfrac{l_e^{[0]}}{2 \cdot \sigma^{\infty}}\right) \cdot d_{i,j} & \text{if } j \in r_i \\ \sigma^{\infty} + \left[(c-1) \cdot \sigma^{\infty} - \displaystyle\sum_{h \neq i} \min\left(\sigma^{\infty}, \sigma_{h,j}\right)\right] \Big/ \left(c - \displaystyle\sum_{h \neq i} b_{h,j}\right) & \text{if } j \notin r_i \end{cases} \tag{4.24}$$

where $d_{i,j}$ is the positive distance from the j-th element of the i-th fibre to the closest broken element in the recovery region r_i (more than one element can fail within the same recovery region, e.g. recovery regions 1 and 2 in Figure 4.18b); and $b_{h,j}$ is a logic operator, which is 1 if the j-th element of the h-th fibre belongs to r_h and 0 otherwise. The first expression of Eq. (4.24) comes from Eq. (4.5) and defines the linear stress field in the proximity of the fibre breaks (red stresses in Figure 4.18b). In the second expression of Eq. (4.24), the term inside square brackets represents the total stress that must be added to σ^{∞} in order to guarantee the equilibrium within the elements of the j-th column. This additional stress is then equally distributed among the intact elements of the j-th column, whose number is given by the term inside round brackets. The second expression of Eq. (4.24) can also be rewritten as

$$\sigma_{i,j} = \left[1 + \frac{(c-1) - \sum_{h\neq i} \min\left(1, \frac{\sigma_{h,j}}{\sigma^{\infty}}\right)}{c - \sum_{h\neq i} b_{h,j}}\right] \cdot \sigma^{\infty} = k_{i,j} \cdot \sigma^{\infty} \qquad \text{if } j \notin r_i \tag{4.25}$$

where $k_{i,j}$ (≥ 1) represents the stress concentration factor that applies to the j-th element of the i-th fibre. It should be noted that $\sigma_{h,j}$ enters in the definition of $k_{i,j}$ only if $\sigma_{h,j} < \sigma^{\infty}$, i.e. when the j-th element of the h-th fibre ($h \neq i$) belongs to the recovery region r_h. This implies

$$\sigma_{h,j} = \left(\frac{l_e^{[0]}}{2 \cdot \sigma^{\infty}}\right) \cdot d_{h,j} \quad \text{if } j \in r_h\,, \;\; h \neq i \tag{4.26}$$

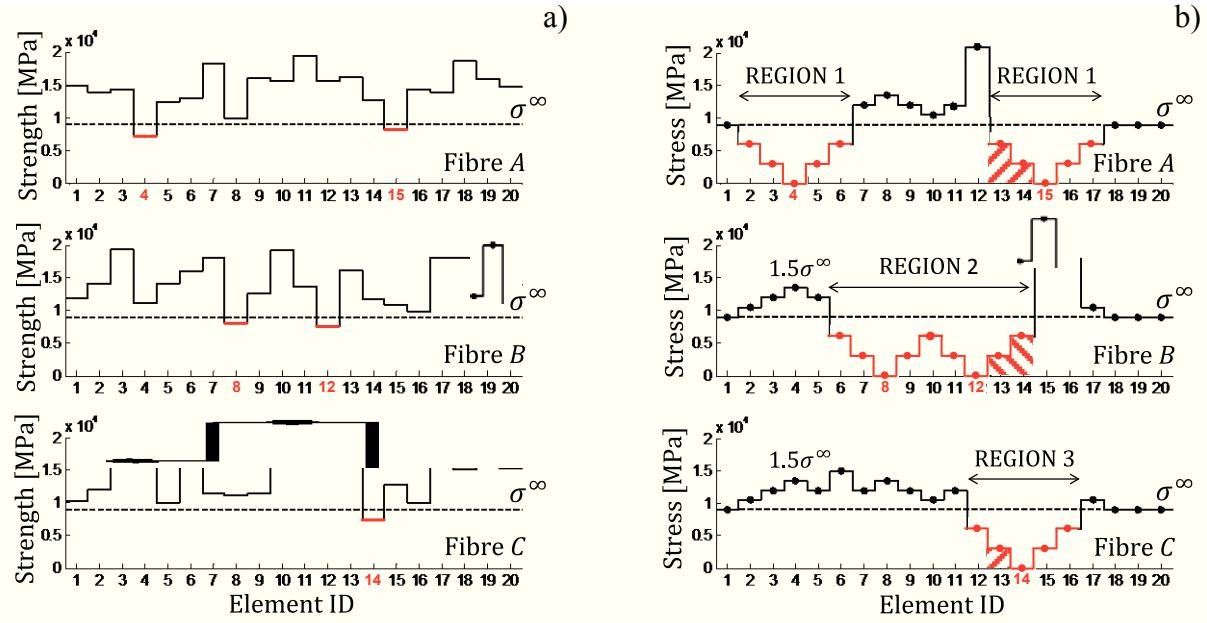

Figure 4.18: a) Elements 4 and 15 of fibre A, elements 8 and 12 of fibre B, and element 14 of fibre C fail under uniform stress loading σ^{∞}; b) The whole bundle fails due to non-equilibrium in elements 13 and 14 (dashed areas).

In order to extend the Monte Carlo progressive failure analysis to higher c's, it is here assumed that a global bundle failure occurs when all sub-bundles are broken and all recovery regions overlap in at least one element (e.g., elements $j = 13$ and $j = 14$ in Figure 4.18b). When this statement is true, the equilibrium cannot be satisfied, i.e.

$$\exists\, j: \sum_{i=1}^{c} \sigma_{i,j} < c \cdot \sigma^{\infty} \tag{4.27}$$

4.3.4 Optimal discretisation of the fibre bundles

The accuracy of the simulated strength distributions strongly depends on the ratios $\Delta^{[i-1]}/L^{[i]}$. If, on the one hand, a finer discretisation leads to more accurate estimates of the strength statistics (mean and coefficient of variation), on the other, it entails longer computation times. Therefore, the optimal values of element and bundle lengths are determined at each level $[i]$, so as to use the minimum number of elements which guarantees both efficiency and convergence of the output strength distribution.

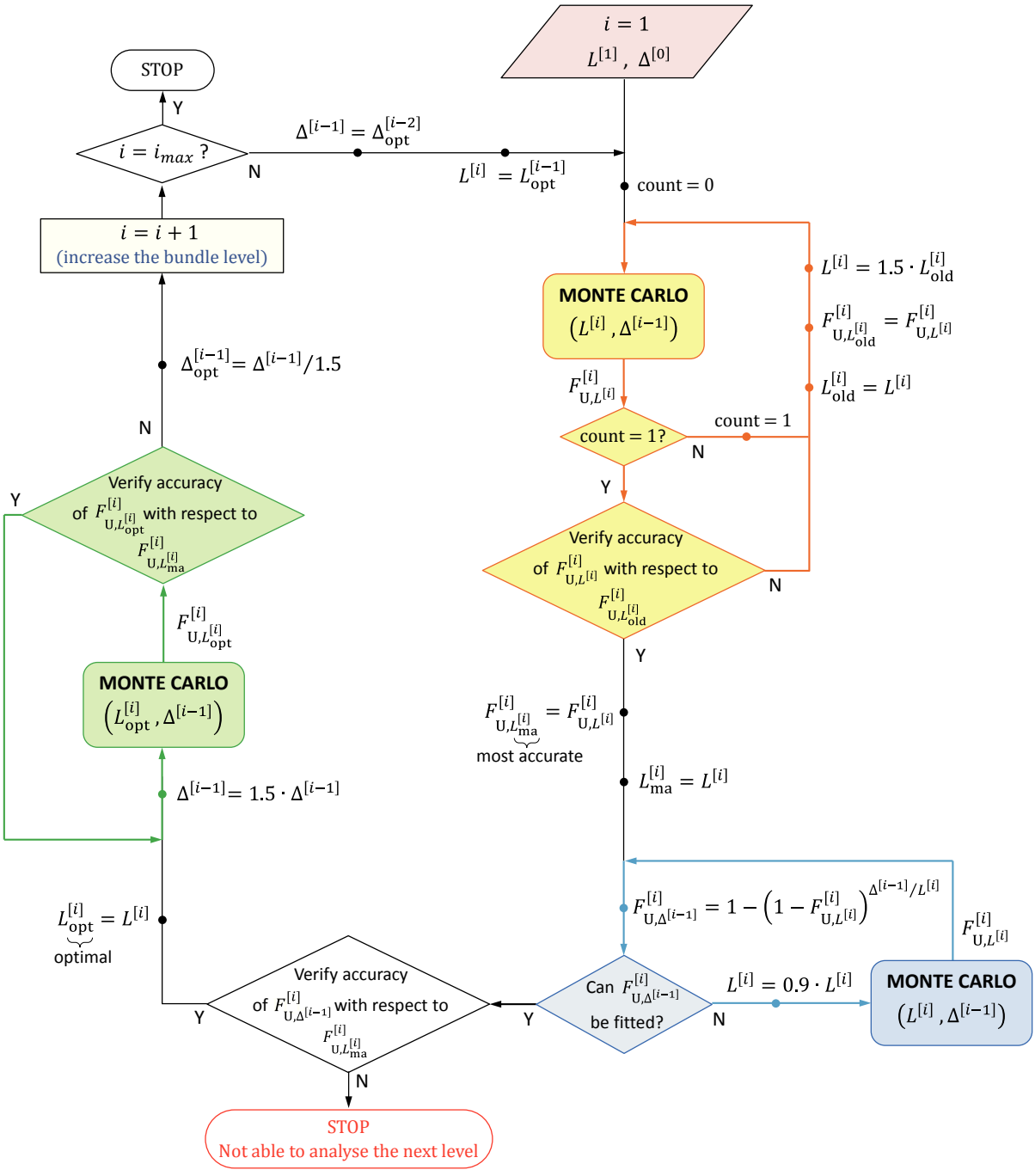

Figure 4.19: Strategy for an optimal discretisation of the fibre bundles.

The main steps of the optimisation process are illustrated in Figure 4.19 and they can be summarised as follows.

Step 1: The analysis starts at level $i = 1$ for given values of $L^{[1]}$ and $\Delta^{[0]}$. These values are chosen based on the reference length l_r of the individual fibre, e.g. $L^{[1]} = l_\mathrm{r}/10$ and $\Delta^{[0]} = L^{[1]}/1000$.

Step 2: In the first loop (yellow blocks), the length of the elements is set equal to $\Delta^{[0]}$ and their number is increased multiplying the bundle length $L^{[1]}$ by 1.5 until convergence of $F^{[1]}_{\mathrm{U},L^{[1]}}$. The latter is achieved when the relative error between the last two estimates is lower than 0.05% for the mean value and 0.5% for the coefficient of variation. The resulting distribution is stored as the most accurate estimate of the level-[1] bundle strength distribution, and it is denoted by $F^{[1]}_{\mathrm{U},L^{[1]}_\mathrm{ma}}$ (the subscript "ma" stands for "most accurate").

Step 3: In the second loop (blue blocks), the bundle length $L^{[1]}$ is decreased by 10% until the scaled distribution $F^{[1]}_{\mathrm{U},\Delta^{[0]}}$ can be fitted with the RTA defined in Eq. (4.23). However, since $L^{[1]}$ has been reduced during the last loop, the accuracy of $F^{[1]}_{\mathrm{U},\Delta^{[0]}}$ must be verified with respect to the most accurate estimate $F^{[1]}_{\mathrm{U},L^{[1]}_\mathrm{ma}}$. To this end, $F^{[1]}_{\mathrm{U},\Delta^{[0]}}$ is scaled to $L^{[1]}_\mathrm{ma}$ for the comparison with $F^{[1]}_{\mathrm{U},L^{[1]}_\mathrm{ma}}$. In this case, a threshold equal to 1% and 2% is chosen for the relative error on the mean value and the coefficient of variation, respectively. If this requirement cannot be satisfied, the analysis stops, otherwise the current value of $L^{[1]}$ is stored as the optimal length for the level-[1] bundle ($L^{[1]}_\mathrm{opt}$).

Step 4: The last loop (green blocks) searches for the optimal value of the element length, $\Delta^{[0]}_\mathrm{opt}$. Here, the initial value $\Delta^{[0]}$ is increased by 50% until the relative error between the new generated $F^{[1]}_{\mathrm{U},L^{[1]}_\mathrm{opt}}$ and $F^{[1]}_{\mathrm{U},L^{[1]}_\mathrm{ma}}$ is reduced to 0.05% and 0.5% respectively for the mean value and the coefficient of variation; the penultimate value of $\Delta^{[0]}$ is then stored as $\Delta^{[0]}_\mathrm{opt}$.

Step 5: Finally, $L^{[1]}_\mathrm{opt}$ and $\Delta^{[0]}_\mathrm{opt}$ are used to define the initial values of $L^{[2]}$ and $\Delta^{[1]}$ for the analysis of the level-[2] bundle. This choice is consistent with the evidence that higher level distributions converge to the WLT applied to the previous-bundle level (Section 4.3.2). Therefore, the contribution of the stable failure modes (in particular of event E_3, which includes growth and coalescence of matrix damage between fibre breaks) becomes progressively less important and always fewer elements (i.e., ratios $\Delta^{[i-1]}/L^{[i]}$ closer to unity) are then required to properly simulate the distributions of the bundle strengths. The optimisation process terminates when a pre-established level $[i_\mathrm{max}]$ is analysed.

4.4 Results

4.4.1 Inputs and outputs

Table 4.1 presents the list of nominal input parameters of the hypothetical material considered in the original analytical model (Pimenta & Pinho, 2013). The first four parameters refer to the Weibull distribution for the strength of individual fibres, being $X_{\mathrm{m}}^{\mathrm{f}}$ the mean value and $\mathrm{CoV}^{\mathrm{f}}$ the coefficient of variation, while σ_0^{f} and m are respectively the scale and the shape parameters. Finally, τ_{SL} is the matrix/interface yield stress, ϕ^{f} the fibre diameter, V^{f} the fibre volume fraction, and l_{r} is the reference length for the scale parameter σ_0^{f}. The progressive failure analysis is repeated $N = 10^6$ times during the Monte Carlo simulation, and the starting values $L^{[1]}$ and $\Delta^{[1]}$ of the optimisation process (Section 4.3.4) are set equal to $L^{[1]} = 1$ mm and $\Delta^{[1]} = 0.001$ mm (i.e., $L^{[1]} = l_{\mathrm{r}}/10$ and $\Delta^{[1]} = L^{[1]}/1000$).

Table 4.1: Input parameters for the numerical implementation.

Mechanical properties					Geometry		
$X_{\mathrm{m}}^{\mathrm{f}}$	CoV^{f}	σ_0^{f}	m	τ_{SL}	ϕ^{f}	V^{f}	l_{r}
(GPa)	(%)	(GPa)	(—)	(MPa)	(μm)	(%)	(mm)
4.5	25	4.93	4.54	70	5	60	10

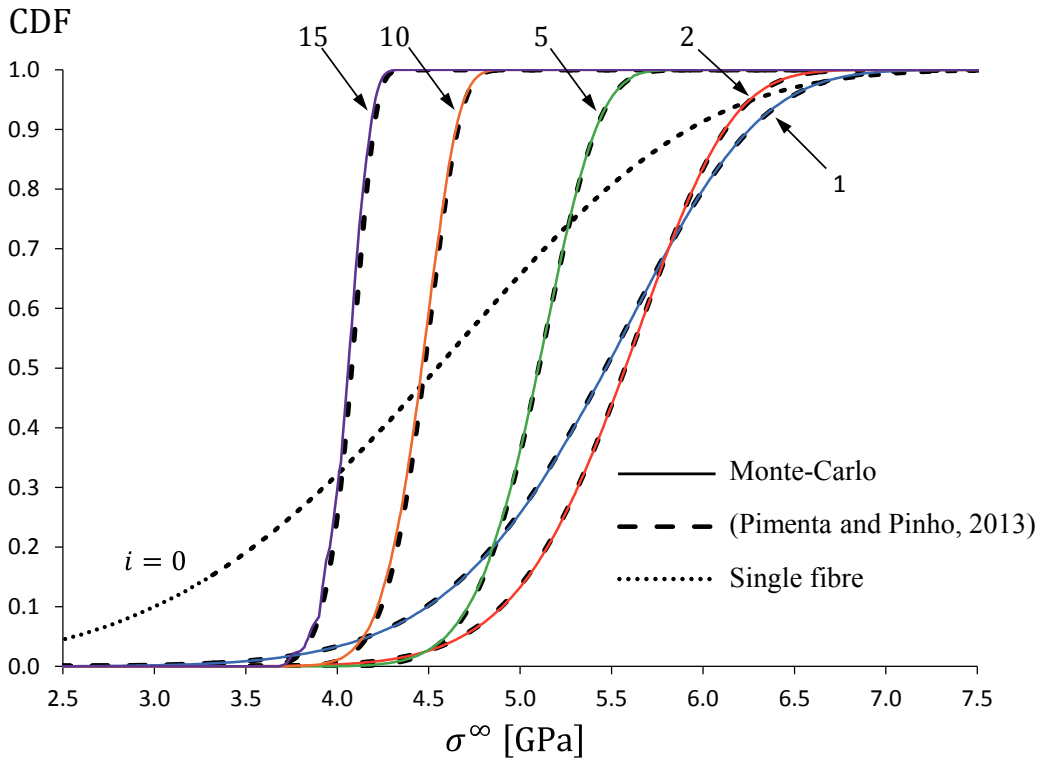

Figure 4.20: Simulated bundle strength distributions from level [1] to level [15], and comparison with Pimenta and Pinho's (2013) model.

4.4.2 Comparison between Monte Carlo analysis and the analytical model

Figure 4.20 illustrates the bundle strength distributions for $c = 2$ and a specimen length of $10\ \mathrm{mm}$. The simulated strengths (solid lines) of the first 15 levels show good agreement with Pimenta and Pinho's (2013) model (dashed lines), proving that the numerical simulation correctly models the same features as the analytical one.

4.4.3 Effects of the coordination number

Figure 4.21 describes the size effects on the statistics of the strength distributions, where the value of c ranges from 2 to 7. Both the mean value and the CoV of the strength exhibit common behaviours at different c's: after an initial strengthening and steep reduction in variability, both the mean value and the variability of tensile strength gradually decrease with increasing specimen cross-section (the number of fibres in a level-[i] bundle is calculated as c^i). In particular, for all c's, the magnitude of size effects starts decreasing for bundle levels higher than 3, as indicated by the upwards curvature of the right tail of the curves in Figure 4.21a.

As the coordination number c increases, the curves in Figure 4.21 shift to higher mean strengths and lower CoVs. This strengthening effect is mainly due to lower average stress concentration factors among intact fibres (or sub-bundles) in the proximity of fibre breaks. For instance, $k = 2$ and $k = 1.5$ are respectively applied for $c = 2$ as shown in Figure 4.9b and $c = 3$ in Figure 4.18b.

Table 4.2 reports the optimal discretisation resulting from the procedure described in Section 4.3.4. The ratio $L^{[i]}/\Delta^{[i-1]}$ corresponds to the number of elements that has been used to simulate the strength distribution of the level-[i] bundle. As expected, this number decreases at higher levels $[i]$. In particular, the ratio $L^{[i]}/\Delta^{[i-1]}$ approaches unity about level [5], at which the strength distribution converges to the WLT applied to the previous-bundle level. This means that the bundle strength distributions are completely defined by Eq. (4.23) for $i \geq 5$, so that

$$F^{[i]}_{\mathrm{U},L^{[i]}}(\sigma^{\infty}) \cong 1 - \left[1 - F^{[i-1]}_{\mathrm{U},L^{[i-1]}}(\sigma^{\infty})\right]^{\left(L^{[i]}/L^{[i-1]}\right)\cdot c}, \quad i \geq 5 \tag{4.28}$$

Furthermore, a more detailed analysis of Table 4.2 suggests a faster convergence to the WLT for larger values of c (e.g., the ratios $L^{[i]}/\Delta^{[i-1]}$ for $i = 4$ decrease for increasing values of c). However, a better understanding of this trend would be achieved increasing the number of simulations N, which strongly influences the variability of the data in Table 4.2.

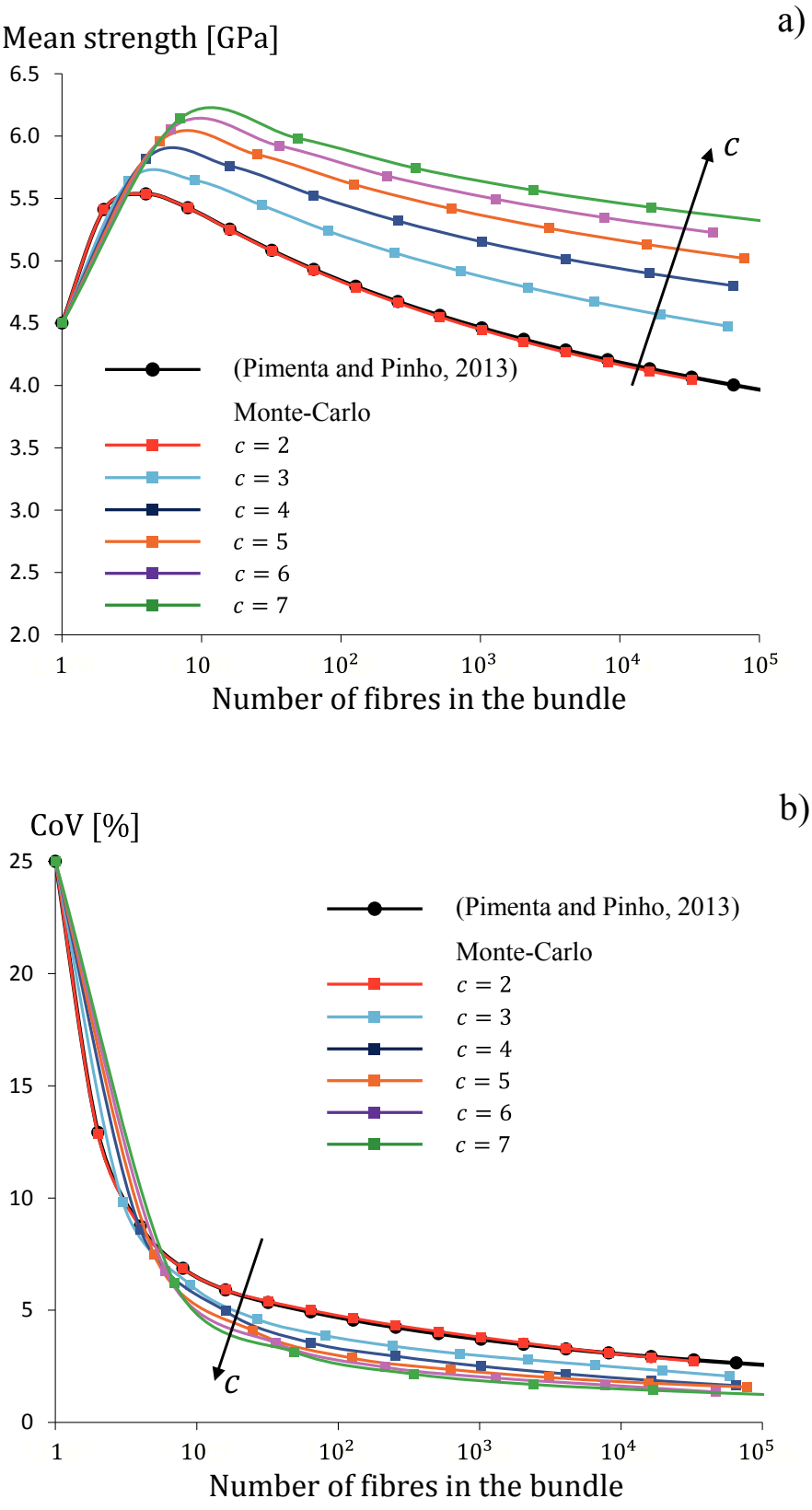

Figure 4.21: Bundle strength size effects on the mean value (a) and on the CoV (b) for coordination numbers c ranging from 2 to 7, and comparison with Pimenta and Pinho's (2013) model.

Table 4.2: Optimal discretisation of fibre bundles and convergence to the WLT for different values of the coordination number.

$c = 2$

i	1	2	3	4	5	6	7	⋯	15
$L^{[i]}$	1.5	2.25	2.25	2.25	2.25	2.25	2.25	2.25	2.25
$\Delta^{[i-1]}$	0.001	0.0114	0.0259	0.0388	0.0577	2.25	2.25	2.25	2.25
$L^{[i]}/\Delta^{[i-1]}$	1500	197	87	58	39	1	1	1	1

$c = 3$

i	1	2	3	4	5	6	⋯	10
$L^{[i]}$	3.375	3.375	3.375	3.375	3.375	3.375	3.375	3.375
$\Delta^{[i-1]}$	0.00764	0.01722	0.02576	0.05921	3.375	3.375	3.375	3.375
$L^{[i]}/\Delta^{[i-1]}$	442	196	131	57	1	1	1	1

$c = 4$

i	1	2	3	4	5	6	7	8
$L^{[i]}$	2.25	2.25	2.25	2.25	2.25	2.25	2.25	2.25
$\Delta^{[i-1]}$	0.001001	0.017176	0.025862	0.086538	2.25	2.25	2.25	2.25
$L^{[i]}/\Delta^{[i-1]}$	2248	131	87	26	1	1	1	1

$c = 5$

i	1	2	3	4	5	6	7
$L^{[i]}$	1.575	1.575	1.575	1.575	1.575	1.575	1.575
$\Delta^{[i-1]}$	0.001001	0.017120	0.025820	0.131250	0.131250	0.131250	1.575
$L^{[i]}/\Delta^{[i-1]}$	1573	92	61	12	12	12	1

$c = 6$

i	1	2	3	4	5	6
$L^{[i]}$	1.2	1.2	1.2	1.2	1.2	1.2
$\Delta^{[i-1]}$	0.001	0.001	0.0076	0.1714	1.2	1.2
$L^{[i]}/\Delta^{[i-1]}$	1200	1200	158	7	1	1

$c = 7$

i	1	2	3	4	5	6
$L^{[i]}$	1.05	1.05	1.575	1.575	3.54375	3.54375
$\Delta^{[i-1]}$	0.001	0.002253	0.039375	0.221484	3.54375	3.54375
$L^{[i]}/\Delta^{[i-1]}$	1050	466	40	7	1	1

4.4.4 Analysis of damage accumulation

Consider first the case of $c = 2$. The damage evolution into clusters of broken fibres is completely defined by the non-brittle term $S_{\mathcal{K}}$ introduced in Section 4.2.2. This term is evaluated combining Eq. (4.8) and Eq. (4.13) into the following expression

$$S_{\mathcal{K}}^{[i+1]}(\sigma^{\infty}) = S_{\mathrm{U,c}}^{[i+1]}(\sigma^{\infty}) - S_{\mathrm{U,e}}^{[i]}(\sigma^{\infty})^4 \tag{4.29}$$

where the right-hand side is recovered by scaling the simulated distributions (Figure 4.20) to the control length $l_{\mathrm{c}}^{[i+1]}$ and the recovery length $l_{\mathrm{e}}^{[i]}$.

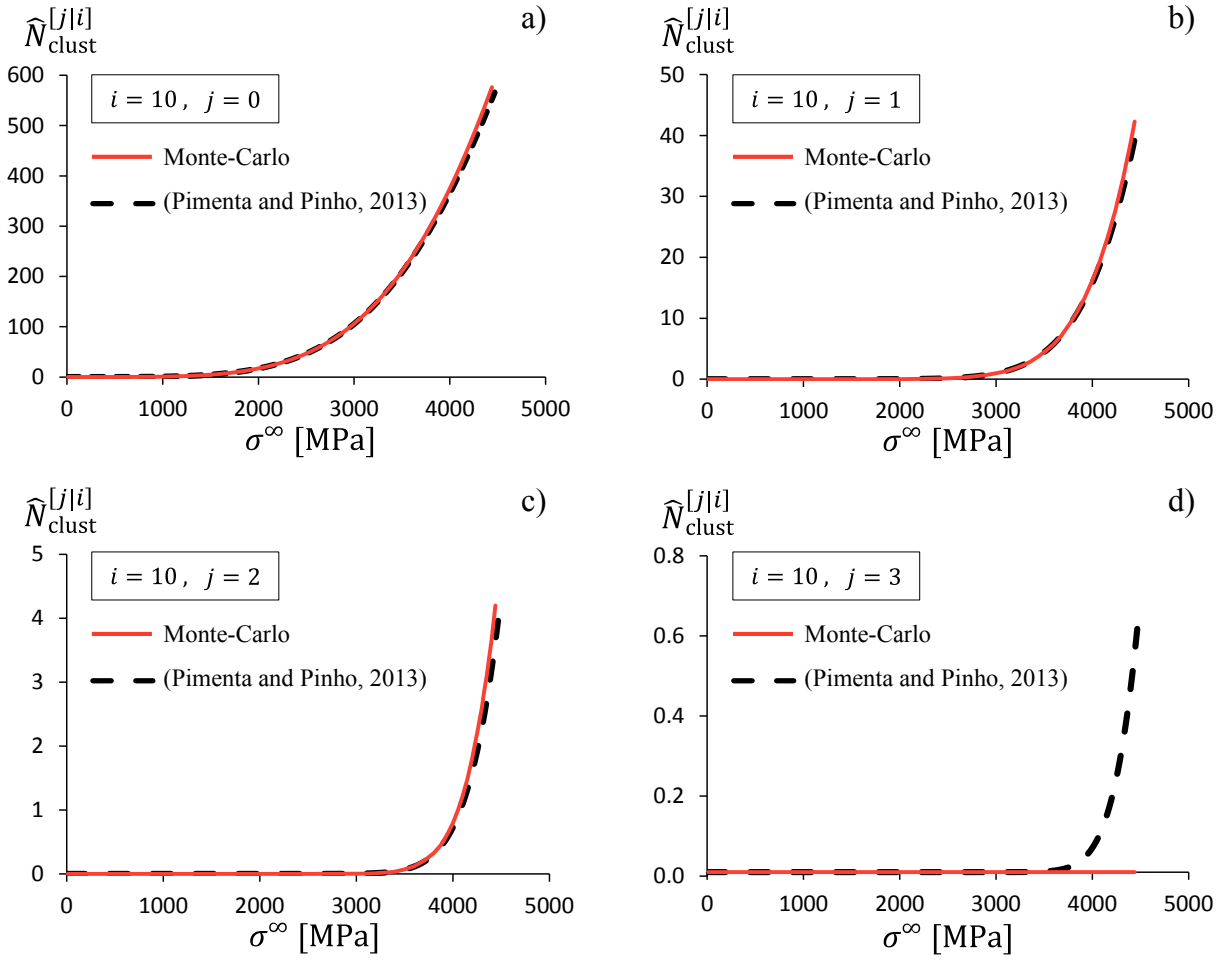

Figure 4.22: Simulated number of broken level-$[j]$ clusters in the level-[10] bundle of length $l_{\mathrm{r}} = 10$ mm, and comparison with Pimenta and Pinho's (2013) model.

Figure 4.22 illustrates the total number of broken level-$[j]$ clusters in the level-[10] bundle of length $l_{\mathrm{r}} = 10$ mm. The simulated curves (red lines) show good agreement with Pimenta and Pinho's (2013) model, with the exception of Figure 4.22d, where the limited number of analyses run by Monte Carlo leads to zero occurrences of level-[3] clusters. Fibre breaks start forming at low applied stresses; as σ^{∞} approaches the average strength of the

bundle (4446 MPa), clusters of broken fibres starts forming and growing, until the largest cluster triggers catastrophic failure of the entire bundle. These results are consistent with experimental observations (Scott et al., 2011). Similar trends are reported in Figure 4.23 for the total number of fibre breaks and the associated density.

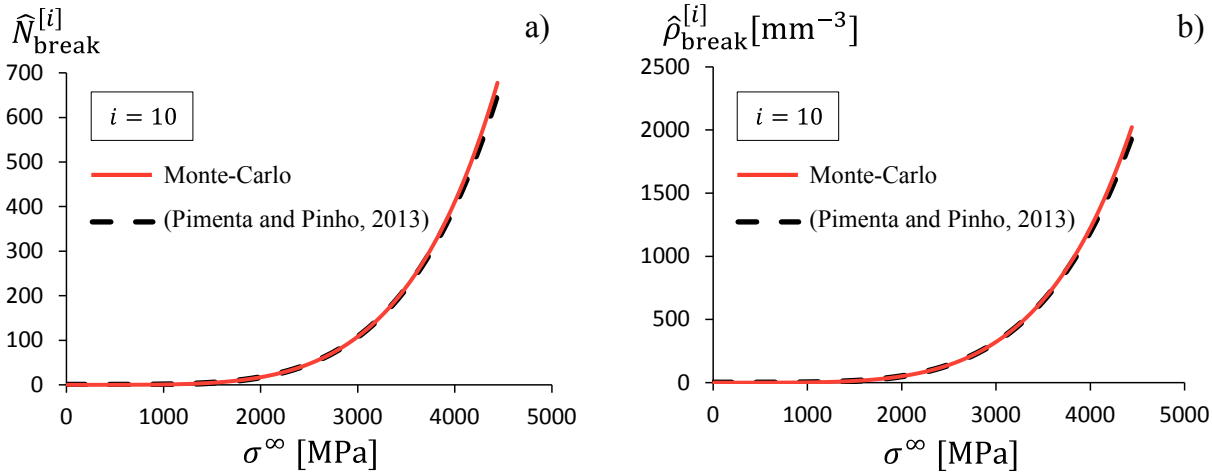

Figure 4.23: Simulated number of broken fibres (a) and associated density (b) in the level-[10] bundle of length $l_{\text{r}} = 10$ mm, and comparison with Pimenta and Pinho's (2013) model.

The total number of fibre breaks in the largest cluster can be estimated as $c\hat{\jmath}_{\text{clust,max}}^{[i]}$, where c is the coordination number ($c = 2$ in this case) and $\hat{\jmath}_{\text{clust,max}}^{[i]}$ is defined by Eq. (4.18). The corresponding curve is shown in Figure 4.24. As expected from Figure 4.22c-d, the largest cluster level is [2] (i.e, 4 broken fibres) by simulation, and [3] (i.e, 8 broken fibres) by applying Pimenta and Pinho's (2013) model.

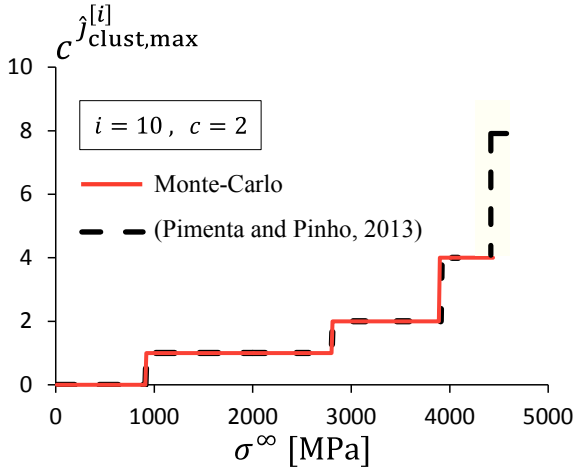

Figure 4.24: Simulated number of broken fibres in the largest cluster of the level-[10] bundle of length $l_{\text{r}} = 10$ mm, and comparison with Pimenta and Pinho's (2013) model.

Finally, the analysis of damage accumulation is extended to higher coordination numbers rewriting the brittle term $S_{\mathcal{U}}$ of Eq. (4.12) as a function of c. As stated in Section 4.2.2, in the brittle domain, the level-$[i+1]$ bundle strength converges to the WLT applied to the previous-bundle level, so that

$$S_{\mathcal{U}}^{[i+1]}(\sigma^{\infty}) = S_{\mathrm{U,c}}^{[i]}(\sigma^{\infty})^{c} = S_{\mathrm{U,e}}^{[i]}(\sigma^{\infty})^{2\cdot c} \tag{4.30}$$

Therefore, Eq. (4.29) for the non-brittle term $S_{\mathcal{K}}$ can now be generalised as

$$S_{\mathcal{K}}^{[i+1]}(\sigma^{\infty}) = S_{\mathrm{U,c}}^{[i+1]}(\sigma^{\infty}) - S_{\mathrm{U,e}}^{[i]}(\sigma^{\infty})^{2\cdot c} \tag{4.31}$$

In Figure 4.25a-b, the density of fibre breaks and the size of the largest cluster are compared with reference to three bundles with equal length $l_{\mathrm{r}} = 10$ mm and similar cross-sectional areas: two bundles are defined by 1204 ($= 2^{10}$, red line; and 4^5, green line) fibres and one bundle by 1296 ($= 6^4$, blue line) fibres. A further example is illustrated in Figure 4.25c-d considering four bundles, of which two with 256 ($= 2^8$, green line; and 4^4, red line) fibres, one with 243 ($= 3^5$, blue line) fibres, and one with 216 ($= 6^3$, grey line) fibres.

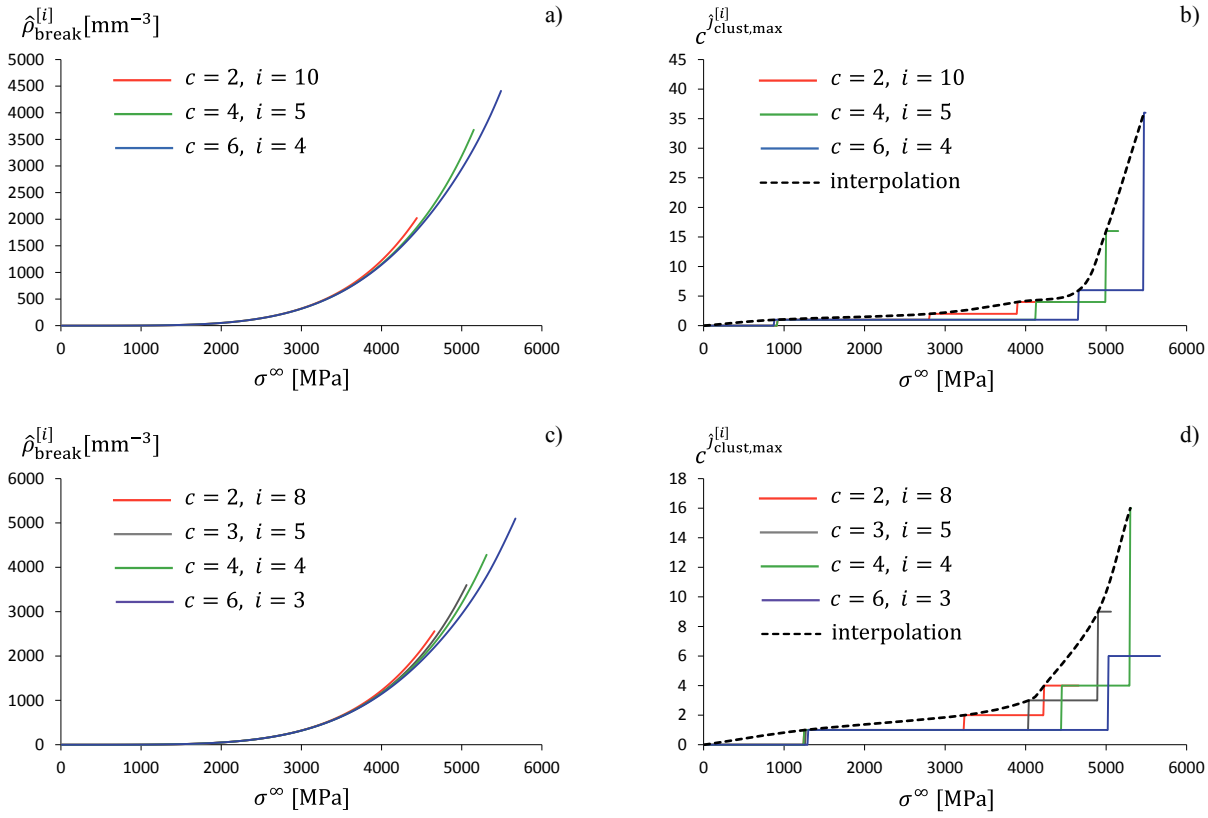

Figure 4.25: Density of fibre breaks and size of the largest cluster in bundles with equal length $l_{\mathrm{r}} = 10$ mm and similar cross-sectional areas.

Despite the coordination number c strongly influences the mean values and the coefficients of variation of the strength distributions (see Figure 4.21), the initial evolution of fibre breaks and formation of clusters are almost unaffected by different c's. Therefore, the damage accumulation at low far-field stresses weakly depends on stress concentration around fibre breaks, but it is rather due to the intrinsic variability of the fibre strength.

4.5 Discussion

4.5.1 Limitations of the present model

Computational time and convergence to the exact solution are the key factors to consider when running Monte Carlo progressive failure analysis. On the one hand, small ratios $\Delta^{[i-1]}/L^{[i]}$ must be used with low-level bundles (see Figure 4.13), where stable failure events (E_2 and E_3) are most likely to occur and need a finer discretisation of the fibres (or sub-bundles) to be accurately simulated. On the other hand, small ratios $\Delta^{[i-1]}/L^{[i]}$ compromise the RTA fitting (see Figure 4.14) and lead to large data sets slowing down the computation. Optimal ratios $\Delta^{[i-1]}/L^{[i]}$ must then be established as in Section 4.3.4 for each bundle level and for each set of mechanical and geometrical properties of the composite material.

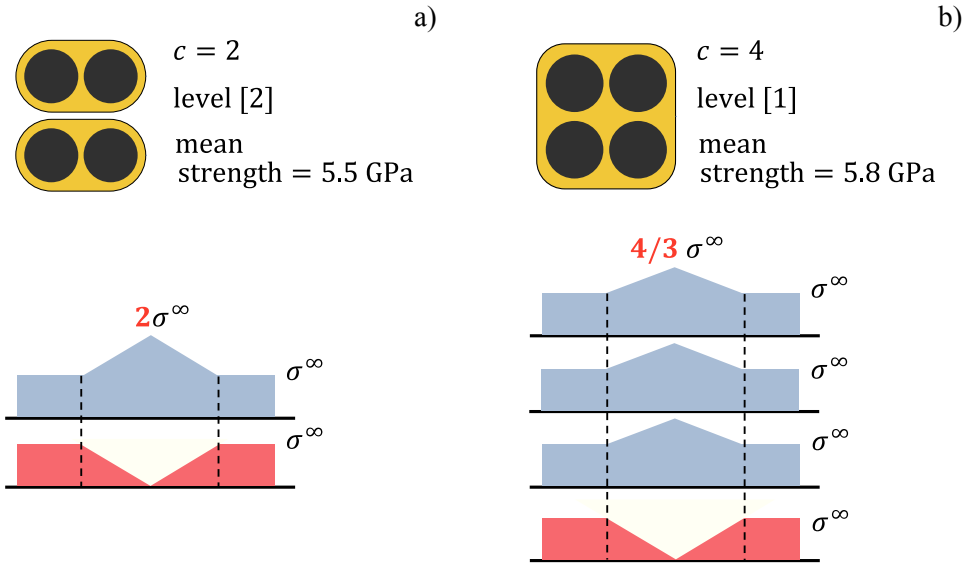

Figure 4.26: Different load-sharing configurations for a bundle with 4 fibres.

Moreover, in the present numerical implementation, bundles with identical number of fibres but higher coordination number c result in higher mean strengths. As explained in Section 4.4.3, this is mainly due to lower average stress concentration factors among intact fibres (or sub-bundles) at higher c's. Figure 4.26 illustrates the case of a bundle with 4 fibres, which is modelled both as a bundle of level [2] with $c = 2$ (Figure 4.26a) and as a bundle of

level [1] with $c = 4$ (Figure 4.26b). According to Eq. (4.25), a stress concentration factor $k = 2$ applies in the first case, and $k = 4/3$ in the second case. The lower stress concentration in the latter case leads to a higher mean value of the bundle strength.

Nevertheless, the analytical sequences of events leading to bundle failure (E_1, E_2 and E_2) are here collected into only one exhaustive global failure criterion, which is defined by the inequality in Eq. (4.27). Such a criterion may result in very high peaks in the stress profile as in the case of fibres A and B in Figure 4.18b, while, in reality, the matrix would not be able to transfer stresses so effectively without failing. Therefore, the present numerical approach leads to and overestimation of the strength for high values of the coordination number c, and this contributes to the strengthening effect observed in Figure 4.21.

4.5.2 Advantages of the present model

The numerical model copes with more complex stress fields (see Figure 4.18b) than the analytical model (Pimenta & Pinho, 2013) (see Figure 4.5), and there is no need to define a control region – and, consequently, no need to impose assumptions $A(i)$ and $A(ii)$ (see Section 4.2.1) in the former. Therefore, the good agreement between analytical and numerical results in Figure 4.20 suggests that the predictions of the analytical model are not affected by these restrictions on the control region.

The arbitrariness of the stress profiles also allows the present analysis to be easily generalised to any value of the coordination number c. Therefore, the coordination number is treated as a free parameter, and no modifications are made to the numerical implementation when dealing with different load-sharing configurations.

Finally, a user-defined input distribution (i.e., not necessarily a Weibull) can be used for the individual fibre strength. For instance, a bi-modal Weibull strength distribution has been proposed (Watanabe et al., 2014) to account for the effects of two different flaw populations in the fibres, one operating at longer gauge lengths and characterised by large variability, and another operating at shorter gauge lengths and associated with smaller strength variability. Such distribution could be introduced in the present implementation to further investigate the stochastic behaviour of fibre-reinforced composites and the related size effects.

4.6 Conclusions

A new numerical approach was developed to model size effects on the longitudinal tensile strength of composite fibre bundles. The method applies a discretisation of hierarchical bundles by grouping chains of level-$[i]$ bundles into a level-$[i+1]$ bundle, and a Monte Carlo progressive failure analysis evaluates the corresponding strength distribution.

A comparison was carried out with the analytical model developed by Pimenta and Pinho (2013) for the simple case of coordination number $c = 2$ (i.e., grouping fibres and bundles 2 by 2); the good agreement of results proved that the numerical approach is able to model the same features as the analytical one (see Figure 4.20).

Furthermore, the numerical method was generalised to any value of the coordination number c. Of particular interest is the case for $c = 7$, which better represents the actual disposition of fibres in the bundle cross-section. A series of analyses was then carried out for c ranging from 2 to 7, and a strengthening effect was observed for increasing values of c (see Figure 4.21), which is mainly due to lower average stress concentration factors among intact fibres in the proximity of fibre breaks.

The proposed method was also employed for the analysis of the damage accumulation process during progressive failure. Although the coordination number c strongly influences the mean values of the strength distributions, the evolution of clusters of broken fibres is not significantly affected by different configurations of the bundle cross-sections, but it rather depends on the intrinsic variability of the individual fibre strength.

Work is still underway to improve the global failure criterion and to validate results against experimental data available in literature. Concerning the first task, more accurate estimates of the bundle strength distributions would be achieved by redefining the recovery length to account for the total number of broken fibres in the bundle. This concept is illustrated in Figure 4.27, representing a level-$[1]$ bundle with coordination number $c = 4$ and 3 broken fibres (B, C and D); stresses are recovered within a recovery length $l_e^{[0]}$ (given by Eq. (4.5)), and a stress concentration factor equal to 4 applies to the intact fibre (A) due to the equilibrium. As a result, the stress field slope in fibre A exceeds the maximum speed (slope) at which stresses are recovered in the broken fibres (red dashed lines in Figure 4.27). In reality, the matrix would not be able to transfer stresses so effectively without failing and, therefore, the present numerical approach leads to and overestimation of the bundle strengths, which contributes in part to the strengthening effect mentioned above.

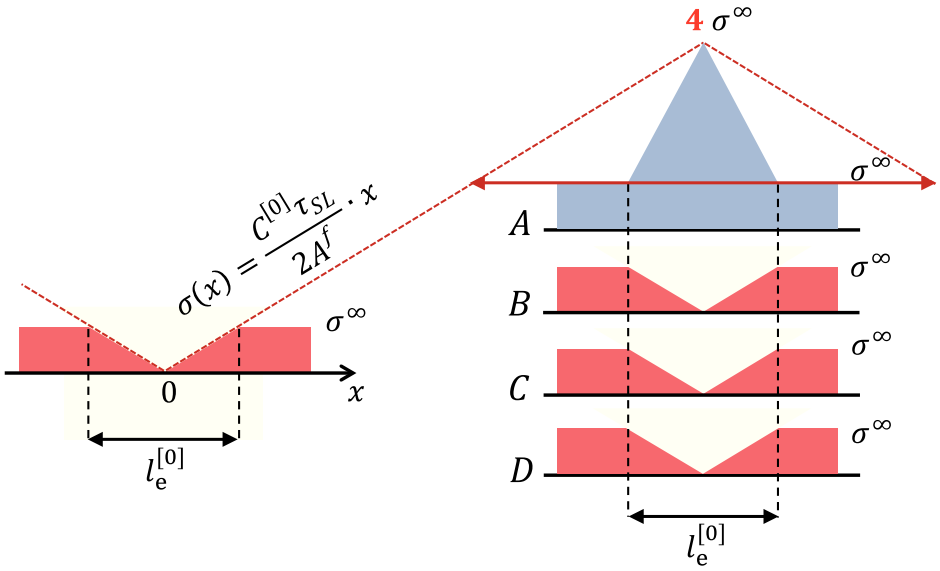

Figure 4.27: Influence of the total number of broken fibres on the recovery length.

In the present numerical implementation, the maximum slope of the stress-recovery field in the broken fibres is assumed to be dependent only on the geometrical properties of the fibres (i.e., the cross sectional area, A^f, and the shear-lag perimeter, $C^{[0]}$) and on the material properties of the matrix (i.e., the yield stress in shear, τ_{SL}). However, the same limit should also apply to the stress field in the intact fibre A, and this would increase the length of the recovery region as indicated by the red double arrow in Figure 4.27. It follows that a new definition of the recovery length is needed based on the stress concentration factor in the intact fibres (or sub-bundles), which in turn depends on the total number of broken fibres (or sub-bundles) in the bundle.

5 General conclusions

5.1 Summary of major findings

This thesis developed novel methods for reliability analysis of complex structural systems with particular focus on the risk assessment of offshore structures and the uncertainty quantification of composite fibre bundles. The overall failure of both these types of structures is characterised by a huge number of critical sequences of component failures, thus resulting in a complex system event. However, accurate and efficient evaluation of the system-level risk can be achieved retaining only the dominant failure modes, i.e. the critical failure sequences that are most likely to contribute to global structural collapse. These modes must be identified with respect to the redistribution of the internal load effects after member failures, and a system reliability analysis method is needed to account for statistical dependence among components events as well as among failure modes.

In this regard, the merits of a risk assessment framework recently developed for truss and frame structures (Kim et al., 2013) have been investigated in the first part of this work (Chapter 3), in view of its extensive application to the offshore field. To this end, the problem of a jacket-type platform under an extreme sea state was considered, and the accuracy and the efficiency of the proposed approach were successfully validated against crude Monte Carlo Simulation (MCS). In the second part of the thesis (Chapter 4), system reliability theory was applied to the uncertainty quantification of the longitudinal tensile strength of UniDirectional (UD) composites. Here, a Monte Carlo progressive failure analysis has been proposed to model the full strength distributions of fibre bundles of any size, thus allowing experimental data measured in small coupons to be used for the design of large composite structures. These studies provided the following major findings:

- In Chapter 3, a jacket-type platform was modelled as a truss structure with members failing either in tension or compression. Sources of uncertainty were considered both in the material properties (yield stress) and in the environmental loading (current-wave forces mainly). Using the risk assessment framework developed by Kim et al. (2013), the dominant failure modes of the jacket-type platform were rapidly identified by means of a multi-point parallel search employing a genetic algorithm. This searching scheme explores

regions of the random variable space that are progressively more distant from the mean of the input random vector (i.e., the point of the random space corresponding to the expected values of the yield stresses, the wave height, the current speed, and the drag and mass coefficients of the tubular members). In this way, multiple dominant failure modes are identified in the decreasing order of their likelihood so that the searching process can be terminated as the contributions by newly identified modes become negligible (without missing critical failure sequences). Then, the evaluation process of the probabilities of failure modes and the system event is carried out by a multi-scale Matrix-based System Reliability (MSR) analysis, in which the statistical dependence among both components and failure modes is fully considered through simple matrix operations. Differently from other existing approaches, the identification process is here decoupled from the probability evaluation process. This feature helps avoid component and system reliability analyses to be performed repeatedly during the search process, which otherwise would be computationally too demanding for large structures with a high level of redundancy. As a result, the proposed method guarantees an efficient estimation of the system-level risk; in particular, the number of iterations was found to be 1-2 orders of magnitude less than those required by MCS. In order to test the accuracy of the method, the effect of the post-buckling factor on structure-level failure probability was also investigated. As far as the post-failure behaviour moves away from the brittle zone (lower post-buckling factor) to the ductile zone (higher post-buckling factor) the redundancy level in the structure is enhanced and accordingly, the system reliability index increases. An excellent agreement was found between the reliability indexes estimated by the proposed method and by MCS in the entire domain of the post-buckling factor. Moreover, while the computational time required by MCS varies exponentially with system reliability index, the time required by the proposed method is insensitive to this value.

- In Chapter 4, a new numerical approach was developed to model size effects on the stochastic longitudinal tensile strength of composite fibre bundles. The method applies a discretisation of hierarchical bundles by grouping a predefined number c (termed "coordination number") of chains of level-$[i]$ bundles into a level-$[i+1]$ bundle; the corresponding strength distribution is then simulated by means of a Monte Carlo progressive failure analysis. This study extended the capabilities of the analytical model developed by Pimenta and Pinho (2013), which is limited to the simple case of coordination number $c = 2$ (i.e., bundles are grouped 2 by 2). Despite this model allows a straightforward evaluation of the bundle strengths, imposing $c = 2$ results in very high stress concentrations in the proximity of fibre breaks. In order to deal with different load-sharing configurations, the present approach treats the coordination number as a free parameter. Of particular interest is the case for $c = 7$, which better represents the actual disposition of fibres in the bundle cross-section. A series of analyses was then carried out for c ranging from 2 to 7, and a strengthening effect was observed for increasing values of c, which can be explained by lower average stress concentrations among intact fibres in the proximity of fibre breaks. The proposed method was also employed for the analysis of the damage accumulation process

during progressive failure. Although the coordination number c strongly influences the mean values of the strength distributions, the evolution of clusters of broken fibres is not significantly affected by different configurations of the bundle cross-sections, but it rather depends on the intrinsic variability of the individual fibre strength

5.2 Future research topics

In the following, some recommendations for future studies and improvements are suggested:

- Concerning the study in Chapter 3, the computational efficiency and accuracy arising from the capability to separate the failure mode identification from the probability evaluation processes first, and to rationally consider the statistical dependence among failure events then, make the proposed approach particularly attractive to the offshore industry. Further research will then investigate the applicability of this method to both design and planning of inspection, maintenance and repair strategies. Performing an inspection implies the reduction of the uncertainty associated with the knowledge of the system. This fact is reflected by an increase of the reliability index in the case of in-service inspection as well as in the case of inspection planning at the design stage. In the first case, the reliability of a structure subjected to fatigue failure can be updated based on new information obtained during non-destructive inspections (NDIs). In this context, the proposed reliability method would provide an efficient tool for assessment of lifetime extension of structures beyond their original design lives. At the design stage, this method would help estimate the time to first inspection and the interval between subsequent inspections so that a pre-established reliability level could be guaranteed.

- Concerning the study in Chapter 4, work is still underway to improve the global failure criterion of the fibre bundles and to validate results against experimental data available in literature. In the current numerical implementation, the stress field is calculated assuming the stress concentration to be equally distributed among intact elements in the proximity of fibre breaks. Such a criterion may result in very high peaks in the stress profile, while, in reality, the matrix would not be able to transfer stresses so effectively without failing. Therefore, the present numerical approach leads to and overestimation of the mean values of the bundle strength distributions, and developing a new global failure criterion would increase the accuracy of the results.

References

API RP2A-LRFD. (1993). *Recommended Practice for Planning and Constructing Fixed Offshore Platforms, Load and Resistance Factor*. (1st ed.).

Ambartzumian, R., Der Kiureghian, A., Ohanian, V., & Sukiasian, H. (1998). Multinormal probability by sequential conditioned importance sampling: theory and application. *Probabilistic Engineering Mechanics, 13*(4), 299–308.

Arnold, B. C., Balakrishnan, N., & Nagaraja, H. N. (1992). *A First Course in Order Statistics.* New York: John Wiley.

ASAS User Manual. (2010). Version 13.0. ANSYS, Inc. Southpointe 275 Technology Drive Canonsburg, PA 15317: http://www.ansys.com.

Ayala-Uraga, E., & Moan, T. (2002). System reliability issues of offshore structures considering fatigue failure and updating based on inspection. *1st International ASRANet Colloquium.* 8-10 July, 2002, Glasgow, Scotland.

Bažant, Z. P. (1999). Size effect on structural strength: a review. *Archive of Applied Mechanics, 69*, 703-725.

Beyerlein, I. J., & Phoenix, S. L. (1996). Statistics for the strength and size effects of microcomposites with four carbon fibres in epoxy resin. *Composites Science and Technology, 56*, 75-92.

Bjerager, P. (1991). Methods for structural reliability computations . In F. Casciati, & J. B. Roberts, *Reliability problems: general principles and applications in mechanics of solids and structures* (pp. 89-136). Springer-Verlag Wien.

Boccotti, P. (2000). *Wave mechanics for ocean engineering.* Elsevier Oceanography Series.

Bomel Ltd. (2002). *System-based calibration of north-west European Annex Environmental Load Factors to ISO Fixed Structures Code 19902.* Report No. C925\04\016R, Rev B.

Boole, G. (1854). *Laws of thought.* American Reprint of 1854 ed., Dover.

Bourinet, J.-M. (2010). *FERUM 4.1 User's Guide.* IFMA.

Bourinet, J.-M., Mattrand, C., & Dubourg, V. (2009). A review of recent features and improvements added to FERUM software. *Proc. of the 10th International Conference on Structural Safety and Reliability (ICOSSAR'09).* Osaka, Japan.

Boyle, P., Broadie, M., & Glasserman, P. (1997). Monte Carlo methods for security pricing. *Journal of economic dynamics and control, 21*(8), 1267-1321.

Breitung, K. (1984). Asymptotic approximations for multinormal integrals. *Journal of Engineering Mechanics, 110*(3), 357-66.

Chakrabarti, S. K. (2005). *Hanbook of offshore engineering.* Elsevier.

Cornell, C. A. (1967). Bounds on the reliability of structural systems. *Journal of structural division, ASCE, 93, ST1*, 171-200.

Curtin, W. A. (1991). Theory of mechanical properties of ceramic-matrix composites. *Journal of the American Ceramics Society, 74*, 2837-2845.

Curtin, W. A. (1999). Stochastic damage evolution and failure in fiber-reinforced composites. *Advances in Applied Mechanics, 36*, 163-253.

Dean, R. G. (1974). *Evolution and development of water wave theories for engineering application, Vol. I and II.* Fort Belvair, VA: Special Report No. 1, Coastal Engineering Research Center U.S. Army.

Der Kiureghian, A. (2005). First- and second-order reliability methods. In *Engineering design reliability handbook.* Boca Raton, FL: CRC Press.

Der Kiureghian, A., & Song, J. (2008). Multi-scale reliability analysis and updating of complex systems by use of linear programming. *Reliability Engineering and System Safety, 93*(2), 288-97.

Der Kiureghian, A., Lin, H.-Z., & Hwang, S.-L. (1987). Second-order reliability approximations. *Journal of Engineering Mechanics, 113*(8), 1208-25.

Devroye, L. (1986). *Non-Uniform Random Variate Generation.* NY: Springer-Verlag.

Ditlevsen, O. (1979). Narrow reliability bounds for structural systems. *Journal of Structural Mechanics, 7*(4), 453–472.

Ditlevsen, O., & Madsen, H. O. (2007). *Structural Reliability Methods.* Lyngby, Denmark: Technical University of Denmark.

Du, X. (2015). *Probabilistic Engineering Design, Lecture notes.* Missoury University of Science and Technology: http://web.mst.edu/~dux/repository/me360/me360.html.

Dunnet, C. W., & Sobel, M. (1955). Approximations to the probability integral and certain percentage points of a multivariate analogue of Student's t-distribution. *Biometrika, 42*, 258–60.

Embrechts, P., Klüppelberg, C., & Mikosch, T. (1997). *Modelling Extremal Events for Insurance and Finance.* New York: Springer.

Feng, Y. (1989). A method for computing structural system reliability with high accuracy. *Computers & Structures, 33*(1), 1-5.

Fishman, G. S. (1995). *Monte carlo: Concepts, algorithms, and applications.* N.Y., USA: Springer-Verlag.

Frangopol, D. M., & Maute, K. (2003). Life-cycle reliability-based optimization of civil and aerospace structures. *Computers and Structures, 81*, 397-410.

Genz, A. (1992). Numerical computation of multivariate normal probabilities. *Journal of Computational and Graphical Statistics, 1*, 141-150.

Gharaibeh, E. S., Frangopol, D. M., & Onoufriou, T. (2002). Reliability-based importance assessment of structural members with applications to complex structures. *Computers and Structures, 80*, 1113-1131.

Goldberg, G. E. (1989). *Genetic algorithms in search, optimization and machine learning.* Reading, MA: Addison-Wesley.

Goodstein, R. L. (2007). *Boolean Algebra.* Mineola, New York: Dover Publications, Inc.

Guenard, Y. F. (1984). *Application of System Reliability Analysis to Offshore Structures.* Stanford, CA: Report No. 71: John Blume Earthq. Engng. Center, Stanford University.

Haldar, A. (2006). *Recent Developments in Reliability-based Civil Engineering.* Singapore: World Scientific Publishing Company.

Haldar, M., & Mahadevan, S. (2000). *Probability, Reliability, and Statistical Methods in Engineering Design.* John Wiley.

Harlow, D. G., & Phoenix, S. L. (1978a). The chain-of-bundles probability model for the strength of fibrous materials. I: Analysis and conjectures. *Journal of Composite Materials, 12*, 195-214.

Harlow, D. G., & Phoenix, S. L. (1978b). The chain-of-bundles probability model for the strength of fibrous materials. II: A numerical study of convergence. *Journal of Composite Materials, 12*, 314-334.

Hasofer, A. M., & Lind, N. C. (1974). Exact and invariant second-moment code format. *J. Engng. Mech. Div. ASCE, 100*(EM1), 111-121.

Hohenbichler, M., & Rackwitz, R. (1983). First-order concepts in system reliability. *Structural Safety, 1*(3), 177-188.

Hohenbichler, M., & Rackwitz, R. (1988). Improvement of second-order reliability estimates by importance sampling. *Journal of Engineering Mechanics, ASCE, 114*(12), 2195-2199.

Hunter, D. (1976). An upper bound for the probability of a union. *Journal of Applied Probability, 13*, 597–603.

Kang, W. H., Lee, Y. J., Song, J., & Gencturk, B. (2012). Further development of matrix-based system reliability method and applications to structural systems. *Structure and Infrastructure Engineering: Maintenance, Management, Life-cycle Design and Performance, 8*(5), 441–57.

Kang, W.-H., Song, J., & Gardoni, P. (2008). Matrix-based system reliability method and applications to bridge networks. *Reliability Engineering & System Safety, 93*, 1584-1593.

Karamchandani, A. (1987). *Structural system reliability analysis methods.* Report no. 83. Department of Civil Engineering, Stanford University.

Karamchandani, A., Dalane, J. I., & Bjerager, P. (1992). Systems reliability approach to fatigue of structures. *Journal of Structural Engineering, 118*(3), 684-700.

Kazanci, M. (2004). Carbon fiber reinforced microcomposites in two different epoxies. *Polymer Testing, 23*, 747-753.

Kim, D.-S., Ok, S.-Y., Song, J., & Koh, H.-M. (2013). System reliability analysis using dominant failure modes identified by selective searching technique. *Reliability Engineering and System Safety, 119*, 316-331.

Kotz, S., & Nadarajah, S. (2000). *Extreme Value Distributions: Theory and Applications.* London: Imperial College Press.

Kounias, E. G. (1968). Bounds for the probability of a union, with applications. *The Annals of Mathematical Statistics, 39*(6), 2154–2158.

Kurtz, N., Song, J., Kim, D.-S., & Ok, S.-Y. (2010). Multi-scale system reliability analysis of bridge structures using dominant failure modes identified by selective searching

technique. *The Fifth International Conference on Bridge Maintenance, Safety and Management (IABMAS2010).* 2010, July 11-15, Philadelphia, PA.

Laffan, M. J., Pinho, S. T., Robinson, P., & Iannucci, L. (2010). Measurement of the in situ ply fracture toughness associated with mode I fibre tensile failure in FRP. Part II: Size and lay-up effects. *Composites Science and Technology, 70*, 614-621.

Law, A. M., & Kelton, W. D. (2000). *Simulation modeling & analysis* (3rd ed.). N.Y., USA: McGraw-Hill, Inc.

Lee, Y. J., & Song, J. (2011). Risk analysis of fatigue-induced sequential failures by branch-and-bound method employing system reliability bounds (B3 method). *ASCE Journal of Engineering Mechanics, 137*(12), 807–21.

Lee, Y. J., & Song, J. (2012). Finite-element-based system reliability analysis of fatigue-induced sequential failures. *Reliability Engineering & System Safety, 108*, 131–41.

Lee, Y.-J., Song, J., Gardoni, P., & Lim, H.-W. (2011). Post-hazard flow capacity of bridge transportation network considering structural deterioration of bridges. *Structure and Infrastructure Engineering: Maintenance, Management, Life-cycle Design and Performance, 7*(7), 509-521.

Lim, H.-W., & Song, J. (2012). Efficient risk assessment of lifeline networks under spatially correlated ground motions using selective recursive decomposition algorithm. *Earthquake Engineering and Structural Dynamics, 41*(13), 1861-1882.

Lin, Y. K. (1967). *Probabilistic theory of structural dynamics.* New York: McGraw-Hill Inc.

Liu, P.-L., & Der Kiureghian, A. (1986a). Multivariate distribution models with prescribed marginals and covariances. *Probabilistic Engineering Mechanics, 1*(2), 105-112.

Liu, P.-L., & Der Kiureghian, A. (1986b). *Optimization algorithms for structural reliability analysis.* Report UCB/SESM 86/09. Berkeley: Department of civil engineering, University of California.

Liu, P.-L., & Der Kiureghian, A. (1992). Optimization algorithms for structural reliability. *Structural Safety, 9*, 161–177.

Liu, P.-L., Lin, H.-Z., & Der Kiureghian, A. (1989). *CalREL User Manual.* Report No. UCB/SEMM-89/18. Berkeley, CA: Department of Civil and Environmental Engineering, University of California.

Lutes, L. D., & Sarkani, S. (2004). *Random Vibrations: Analysis Of Structural And Mechanical Systems.* Burlington MA: Elsevier Butterworth-Heinemann.

McKay, N. J., Beckman, R., & Conover, W. J. (1979). A comparison of three methods for selecting value of input variables in the analysis of output from a computer code. *Technometrics, 21*, 239–45.

Moan, T. (1994). Reliability and Risk Analysis for Design and Operations Planning of Offshore Structures. *Proc. 6th ICOSSAR, Structural Safety and Reliability*, (pp. 21-43.). Balkema, Rotterdam.

Moan, T. (2005). *Safety of offshore structures.* Center for Offshore Research and Engineering CORE, Report 2005-04.

Murotsu, Y., Okada, H., Taguchi, K., Grimmelt, M., & Yonezawa, M. (1984). Automatic generation of stochastically dominant failure modes of frame structures. *Structural Safety, 2*, 17–25.

Nguyen, T. H., Song, J., & Paulino, G. H. (2010). Single-loop system reliability-based design optimization using matrix-based system reliability method: theory and applications. *Journal of Mechanical Design*, ASME., 132, 011005-1~11.

Nguyen, T. H., Song, J., & Paulino, G. H. (2011). Single-loop system reliability-based topology optimization considering statistical dependence between limit states. *Structural and Multidisciplinary Optimization, 44*(5), 593-611.

Okabe, T., & Takeda, N. (2002). Size effect on tensile strength of unidirectional CFRPcomposites - experiment and simulation. *Composites Science and Technology, 62*, 2053-2064.

Pandey, M. D. (1998). An effective approximation to evaluate multinormal integrals. *Structural Safety, 20*, 51-67.

Park, S. Y. (2001). A new methodology for the rapid calculation of system reliability of complex structures. *Architectural Research, 3*(1), 71-80.

Pimenta, S. (2014). *Hierarchical scaling law for the strength, deformation and damage accumulation in unidirectional fibre-reinforced composites under tension - contribution to the Tensile Failure Exercise.* Department of Mechanical Engineering, Imperial College London, UK.

Pimenta, S. (2015). Chapter 25: Fibre failure modelling. In *Numerical Modelling of Failure in Advanced Composite Materials.* Elsevier Science and Technology.

Pimenta, S., & Pinho, S. (2013). Hierarchical scaling law for the strength of composite fibre bundles. *Journal of the Mechanics and Physics of Solids, 61*, 1337-1356.

Pimenta, S., Pinho, S. T., Robinson, P., Wong, K. H., & Pickering, S. J. (2010). Mechanical analysis and toughening mechanisms of a multiphase recycled CFRP. *Composites Science and Technology, 70*, 1713-1725.

Polak, E. (1997). *Optimization. Algorithms and Consistent Approximations* (Vol. 124 of Applied Mathematical Sciences). New York, NY: Springer Verlag.

Powell, M. J. (1969). *A method for nonlinear constraints in minimization problems.* New York: Academic Press.

Pradhan, S., Hansen, A., & Chakrabarti, B. K. (2010). Failure processes in elastic fiber bundles. *Reviews of Modern Physics, 82*, 499-555.

Rackwitz, R., & Fiessler, B. (1978). Structural reliability under combined load sequences. *Computers and Structures, 9*, 489{494.

Rice, J. (2007). *Mathematical Statistics and Data Analysis* (3rd ed.). Duxbury Press.

Rosenblatt, M. (1952). Remarks on a Multivariate Transformation. *Annals of Mathematical Statistic, 23*, 470-472.

Scott, A. E., Mavrogordato, M., Wright, P., Sinclair, I., & Spearing, S. M. (2011). Is situ fibre fracture measurement in carbon-epoxy laminates using high resolution computed tomography. *Composites Science and Technology, 71*, 1471-1477.

Sheldon, M. R. (2007). §2.4 Expectation of a random variable. In *Introduction to probability models* (9th ed., pp. 38-47). Academic Press.

Song, J., & Der Kiureghian, A. (2003). Bounds on System Reliability by Linear Programming. *Journal of Engineering Mechanics, 129*(6), 627–636.

Song, J., & Kang, W. H. (2009). System reliability and sensitivity under statistical dependence by matrix-based system reliability method. *Structural Safety, 31*(2), 148–56.

Song, J., & Kang, W.-H. (2007). Matrix-based system reliability method and applications to structural systems. *Proc. 18th Engineering Mechanics Division Conference of ASCE.* June 3-6, Blacksburg, VA.

Song, J., & Ok, S.-Y. (2010). Multi-scale system reliability analysis of lifeline networks under earthquake hazards. *Earthquake Engineering and Structural Dynamics, 39*(3), 259–79.

Srividya, A., & Ranganathan, R. (1992). Automatic generation of stochastically dominant failure modes in frame structures for reliability studies. *Reliability Engineering and System Safety, 37*, 15-23.

Tang, L. K., & Melchers, R. E. (1987). Improved approximation for multinormal integral. *Structural Safety, 4*, 81–93.

Thoft-Christensen, P. (1998). On industrial application of structural reliability theory. *Proc. IFIP 98-WG7.5.* May 11-13, Krakow, Poland.

Thoft-Christensen, P., & Murotsu, Y. (1986). *Application of structural systems reliability theory.* Berlin: Springer-Verlag.

Tvedt, L. (1983). *Two second-order approximations to the failure probability.* Oslo: Veritas Rep. RDIV/20-004083, Det norske Veritas.

Tvedt, L. (1988). Second-order reliability by an exact integral. *Proc. 2nd IFIP Working Conf. on Reliability and Optimization on Structural Systems* (pp. 377–384). New York: Springer.

Tvedt, L. (1990). Distribution of quadratic forms in the normal space - application to structural reliability. *Journal of Engineering Mechanics, ASCE, 116*(6), 1183–1197.

Watanabe, J., Tanakaa, F., Okudaa, H., & Okabe, T. (2014). Tensile strength distribution of carbon fibers at short gauge lengths. *Advanced Composite Materials, 23*(5-6), 535-550.

WAVE User Manual. (2010). Version 13.0. ANSYS, Inc. Southpointe 275 Technology Drive Canonsburg, PA 15317: http://www.ansys.com.

Weibull, G. W. (1951). A statistical distribution function of wide applicability. *Journal of Applied Mathematics*, 293-297.

Wisnom, M. R. (1999). Size effects in the testing of fibre-composite materials. *Composites Science and Technology, 59*, 1937-1957.

Wu, Y.-L., & Moan, T. (1989). A Structural System Reliability Analysis of Jacket using an Improved Truss Model. *Proc. 5th ICOSSAR* (pp. 887-894). San Francisco, New York: ASCE.

Yuan, X.-X., & Pandey, M. D. (2006). Analysis of approximations for multinormal integration in system reliability computation. *Structural Safety, 28*, 361-377.

Zhang, Y. C. (1993). High-order reliability bounds for series systems and application to structural systems. *Computers & Structures, 46*(2), 381-386.

Zhang, Y., & Der Kiureghian, A. (1997). *Finite elements reliability methods for inelastic structures.* Report UCB/SEMM - 97/05. Berkeley: Department of civil and environmental engineering, University of California.

Zwillinger, D., & Kokoska, S. (2000). *Standard Probability and Statistics Tables and Formulae.* CRC Press.

Appendix A:
Regular wave theories

The integration of Morison's formula in Eq. (3.13) requires the evaluation of the wave particle velocity, u, for which a stream function theory of the 5-th order (Dean, 1974) is implemented using Ansys-ASAS^{TM} software (ASAS User Manual, 2010). This theory has been developed for regular (periodic) waves, whose kinematics is completely defined by three parameters: the wave height, H, the wave period, T, and the water depth, d.

The simplest form of regular wave theory is the linear wave theory (or Airy theory), in which the wave profile is described in terms of a sine function (see Figure A.1),

$$\eta(x,t) = a \cdot \sin(kx - \omega t) \tag{A.1}$$

where the three constants a, ω and k respectively indicate the amplitude of the wave ($a = H/2$), the (time) frequency and the wave number (spatial frequency). Eq. (A.1) suggests that the constant wave profile moves in the horizontal direction x with a velocity

$$c = \frac{\omega}{k} = \frac{2\pi/T}{2\pi/L} = \frac{L}{T} \tag{A.2}$$

being L the wave length and T the wave period. Furthermore, a dispersion relationship relates the wave frequency ω to the wave number k,

$$\omega^2 = gk \cdot \tanh(kd) \implies L = \frac{gT^2}{2\pi}\tanh\left(\frac{2\pi}{L}d\right) \tag{A.3}$$

where g is the gravitational acceleration. Therefore, Eq. (A.3) provides a recursive approach to the determination of the wave length L given the wave period T and the water depth d (at the first iteration, tanh can be set equal to 1). Once L (and k) is determined, the wave speed c is calculated from Eq. (A.2). Then, the wave particle velocity field (v_x, v_y) is recovered from Airy theory as a linear function of the wave height H (Chakrabarti, 2005),

$$v_x = \frac{gkH}{2\omega} \cdot \frac{\cosh k(y+d)}{\cosh(kd)} \cdot \cos k(x - ct) \tag{A.4}$$

$$v_y = \frac{gkH}{2\omega} \cdot \frac{\sinh k(y+d)}{cosh(kd)} \cdot \sin k(x - ct) \tag{A.5}$$

where the coordinate system (x, y) is fixed at the still water level (SWL) as illustrated in Figure A.1.

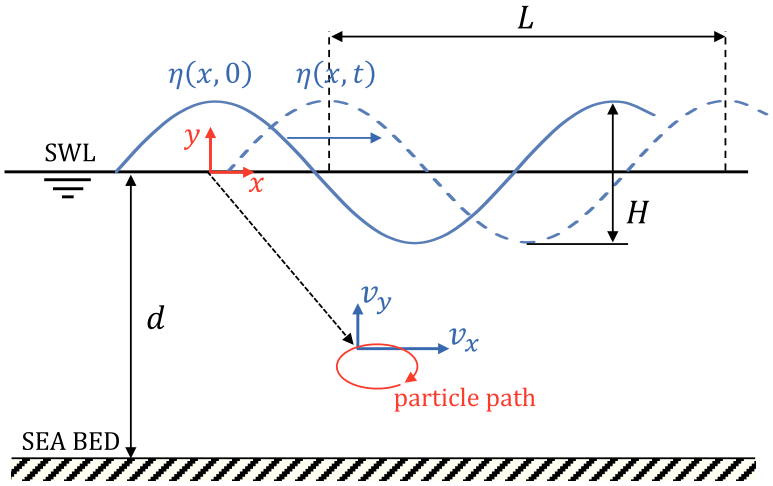

Figure A.1: 2D wave motion over flat bottom.

It should be noted that the vertical component v_y is null at the sea bed ($y = -d$) for all depths in order to satisfy the bottom boundary conditions. Conversely, the value of v_x at the bottom depends on the ratio d/L, and it becomes negligible in deep water ($d/L > 1/2$). Furthermore, the expressions in Eqs. (A.4) and (A.5) are orthogonal to each other so that when the value of v_x is maximum, the vertical component v_y is null and vice versa. As a consequence, in the linear theory, the motion of water particles is described by elliptical closed paths (see Figure A.1). However, net mass transport is generally associated to waves in the ocean, thus indicating open orbital paths. Such a motion is accounted for by the present guidelines as an additional current (e.g. 0.2 knots by API guidelines).

Higher-order theories have been developed to deal with deep-water high waves, which result in wave profiles with steeper crests and shallower troughs. In Chapter 3, a regular stream function theory is implemented (Dean, 1974). Here, the velocity field is defined by the stream function $\psi(x, y, t)$, i.e. a scalar quantity defined as

$$\frac{\partial \psi(x,y,t)}{\partial x} = -v_y \quad , \qquad \frac{\partial \psi(x,y,t)}{\partial y} = v_x \tag{A.6}$$

The dependence of ψ on time is circumvented in the stream function theory by expanding ψ in a series form in a moving coordinate system, i.e.

$$\psi(x,y) = (c-U)y + \sum_{n=1}^{N} X(n)\sinh(nky)\cos(nkx) \tag{A.7}$$

where c is speed of moving system (the same as the wave velocity), U the current velocity (in this formulation, U is negative for opposing current), and the upper limit of the summation N

determines the order of the theory. In order to select the appropriate order of the theory, the plot in Figure A.2 needs to be consulted.

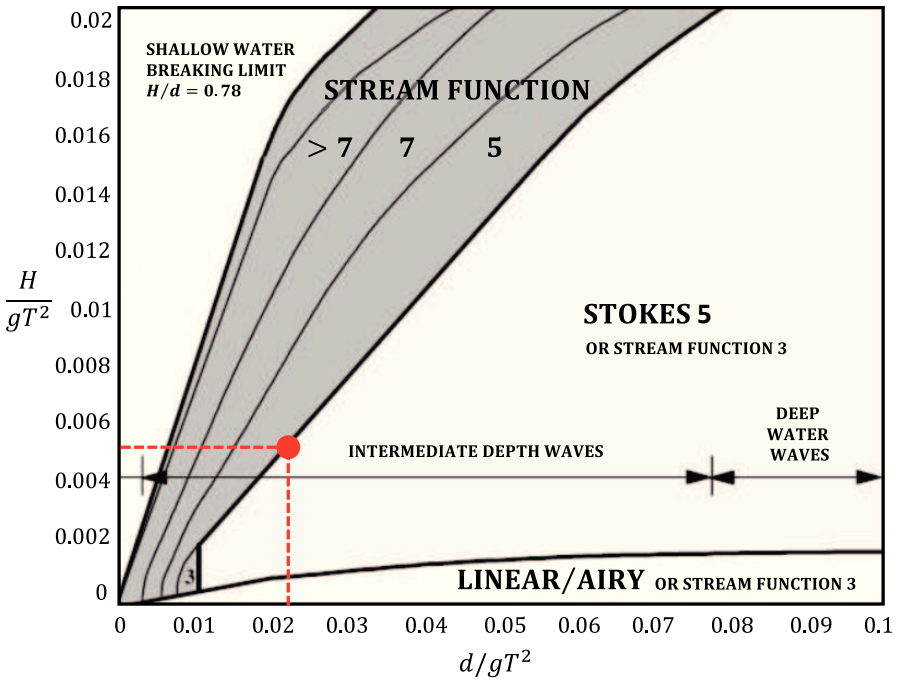

Figure A.2: The range of validity of various wave theories (WAVE User Manual, 2010).

With reference to Section 3.2, the dimensionless ratios H/gT^2 and d/gT^2 in Figure A.2 are calculated using the significant wave height, $H_s = 10$ m, the peak period, $T_p = 14$ s, and the water depth, $d = 43$ m. The resulting point (0.023,0.005) is highlighted in red colour and lies close to the region of the stream function theory of the 5-th order. Such a theory is then selected for the purposes of this work.

Appendix B:
Dunnett-Sobel class correlation model

The matrix-based procedure described in Chapter 3 (see Eq. 3.25) can be used even in the case CSRVs are not explicitly identified. One way to identify such implicit common effect is provided by Dunnett-Sobel (DS) class correlation model (Dunnet & Sobel, 1955). Suppose $\boldsymbol{Z} = (Z_1, \dots, Z_n)$ is a vector of DS class standard normal random variables. This means the correlation coefficient between Z_i and Z_j is defined by $\rho_{ij} = r_i \cdot r_j$ for $i \neq j$ and $\rho_{ii} = 1$. Then, Z_i's can be represented by $(n+1)$ independent random variables:

$$Z_i = \sqrt{1 - r_i^2} \cdot Y_i + r_i S \tag{B.1}$$

where S and $Y_i,\ i = 1, \dots, n$ are independent standard normal random variables. In this way, all the common source effect is implicitly allocated in the random variable S.

When the difference between the actual correlation matrix and the DS-fitted correlation matrix causes significant errors in the system reliability estimate, one can generalise the DS model by adding more CSRVs (Song & Kang, 2009). If m CSRVs $S_i,\ i = 1, \dots, m$ are used for accuracy, Z_i's are represented as

$$Z_i = \sqrt{1 - \sum_{k=1}^{m} r_{ik}^2} \cdot Y_i + \sum_{k=1}^{m} r_{ik} S_k \tag{B.2}$$

The correlation coefficients of this generalised DS model are determined by $\rho_{ij} = \sum_{k=1}^{m} (r_{ik} r_{jk})$, where r_{ik}'s are the generalised DS model coefficients that describe the contribution of the CSVR S_k into Z_i. The best fit to minimise the error of the DS model correlation coefficients is obtained by solving the following nonlinear constrained optimization problem (Powell, 1969)

$$\begin{cases} \min\limits_{\boldsymbol{r}} \| R - R^{DS}(\boldsymbol{r}) \| \\ \text{s.t.} \quad 1 - \sum\limits_{k=1}^{m} r_{ik}^2 > 0, \ \ \forall i \\ \qquad -1 < r_{ik} < 1, \ \ \forall i, k \end{cases} \tag{B.3}$$

where $\boldsymbol{r}$ denotes the set of $r_{ik}, i = 1, \dots, n$ and $k = 1, \dots, m$; R and R^{DS} are respectively the original correlation matrix and the DS correlation matrix; and $\|\cdot\|$ denotes the Euclidean norm of the matrix.

To illustrate the DS fitting procedure, consider a random vector $\boldsymbol{Z}$ defined by 4 standard normal variables Z_i, $i = 1, \dots, 4$ with an arbitrary correlation matrix, e.g.

$$R_{\boldsymbol{Z}} = \{\rho_{ij}\} = \begin{bmatrix} 1 & 0.9 & 0.8 & 0.7 \\ 0.9 & 1 & 0.6 & 0.5 \\ 0.8 & 0.6 & 1 & 0.4 \\ 0.7 & 0.5 & 0.4 & 1 \end{bmatrix} \tag{B.4}$$

If one CSRV is used ($m = 1$), the optimisation problem in Eq. (B.3) leads to

$$\boldsymbol{r} = \begin{bmatrix} r_{11} \\ r_{21} \\ r_{31} \\ r_{41} \end{bmatrix} = \begin{bmatrix} 1.0000 \\ 0.8558 \\ 0.7364 \\ 0.6254 \end{bmatrix} \tag{B.5}$$

$$R_{\boldsymbol{Z}}^{DS} = \boldsymbol{r} \cdot \boldsymbol{r}^{\boldsymbol{T}} = \begin{bmatrix} 1.0000 & 0.8558 & 0.7364 & 0.6254 \\ 0.8558 & 0.7324 & 0.6302 & 0.5352 \\ 0.7364 & 0.6302 & 0.5422 & 0.4605 \\ 0.6254 & 0.5352 & 0.4605 & 0.3911 \end{bmatrix} \tag{B.6}$$

The coefficients in Eq. (B.6) are pretty far from the original values in Eq. (B.4) and the objective function is $\left\| R_{\boldsymbol{Z}} - R_{\boldsymbol{Z}}^{DS}(\boldsymbol{r}) \right\| = 0.6354$. A better accuracy can be achieved using two CSRVs ($m = 2$):

$$\boldsymbol{r} = \begin{bmatrix} r_{11} & r_{12} \\ r_{21} & r_{22} \\ r_{31} & r_{32} \\ r_{41} & r_{42} \end{bmatrix} = \begin{bmatrix} 0.8846 & 0.4664 \\ 0.7891 & 0.3271 \\ 0.3983 & 0.9172 \\ 0.6400 & 0.1663 \end{bmatrix} \tag{B.7}$$

$$R_{\boldsymbol{Z}}^{DS} = \boldsymbol{r} \cdot \boldsymbol{r}^{\boldsymbol{T}} = \begin{bmatrix} 1.0000 & 0.8506 & 0.7802 & 0.6437 \\ 0.8506 & 0.7296 & 0.6144 & 0.5594 \\ 0.7802 & 0.6144 & 1.0000 & 0.4075 \\ 0.6437 & 0.5594 & 0.4075 & 0.4372 \end{bmatrix} \tag{B.8}$$

that implies $\left\| R_{\boldsymbol{Z}} - R_{\boldsymbol{Z}}^{DS}(\boldsymbol{r}) \right\| = 0.5781$. The error can be further reduced using three CSRVs ($m = 3$):

$$\boldsymbol{r} = \begin{bmatrix} r_{11} & r_{12} & r_{13} \\ r_{21} & r_{22} & r_{23} \\ r_{31} & r_{32} & r_{33} \\ r_{41} & r_{42} & r_{43} \end{bmatrix} = \begin{bmatrix} -0.6736 & -0.4732 & -0.5678 \\ -0.6882 & -0.6903 & -0.1934 \\ -0.8081 & +0.0817 & -0.5183 \\ -0.0233 & -0.4742 & -0.8101 \end{bmatrix} \tag{B.9}$$

$$R_{\boldsymbol{Z}}^{DS} = \boldsymbol{r} \cdot \boldsymbol{r}^{\boldsymbol{T}} = \begin{bmatrix} 1.0000 & 0.9000 & 0.8000 & 0.7000 \\ 0.9000 & 0.9875 & 0.6000 & 0.5000 \\ 0.8000 & 0.6000 & 0.9284 & 0.4000 \\ 0.7000 & 0.5000 & 0.4000 & 0.8817 \end{bmatrix} \tag{B.10}$$

This matrix is very close to the original correlation matrix in Eq. (B.4) and the objective function has been reduced to $\left\| R_{\boldsymbol{Z}} - R_{\boldsymbol{Z}}^{DS}(\boldsymbol{r}) \right\| = 0.1183$.

By substituting the coefficients $\boldsymbol{r}$ in Eq. (B.9) into the generalised DS model in Eq. (B.2), the standard normal random vector $\boldsymbol{Z}$ can be rewritten as

$$\boldsymbol{Z} = \begin{bmatrix} Z_1 \\ Z_2 \\ Z_3 \\ Z_4 \end{bmatrix} \cong \begin{bmatrix} 0.0000 \cdot Y_1 \\ 0.1116 \cdot Y_2 \\ 0.2677 \cdot Y_3 \\ 0.3440 \cdot Y_4 \end{bmatrix} + \begin{bmatrix} -0.6736 & -0.4732 & -0.5678 \\ -0.6882 & -0.6903 & -0.1934 \\ -0.8081 & +0.0817 & -0.5183 \\ -0.0233 & -0.4742 & -0.8101 \end{bmatrix} \cdot \begin{bmatrix} S_1 \\ S_2 \\ S_3 \end{bmatrix} \tag{B.11}$$

If a system event E_{sys} is defined as a function of $\boldsymbol{Z}$, all the common source effect is stored in the independent standard normal variables S_1, S_2 and S_3. Therefore, from the total probability theorem, it follows

$$P(E_{sys}) = \int_{s_3} \int_{s_2} \int_{s_1} P(E_{sys} | s_1, s_2, s_3)\, \varphi_3(s_1, s_2, s_3; I_3) ds_1 ds_2 ds_3 \tag{B.12}$$

where φ_3 the trivariate normal distribution with zero mean and 3×3 identity correlation matrix I_3.

Appendix C:
System reliability analysis using Monte Carlo

In Chapter 3, the accuracy of the matrix-based system reliability (MSR) method is validated against crude Monte Carlo analysis. The simulative procedure is here illustrated through the case study of the bicomponent series system shown in Figure C.1.

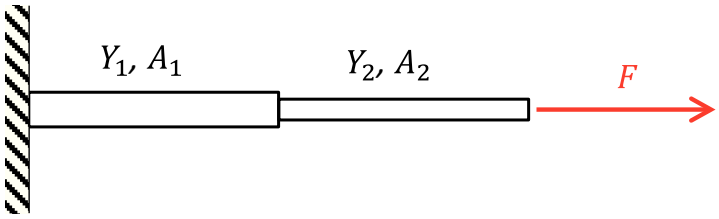

Figure C.1: Series systems consisting of two structural components.

Let the yield strengths Y_1 and Y_2 be correlated normal variables ($\mu_{Y_1} = \mu_{Y_2} =$ 100 MPa, $\sigma_{Y_1} = \sigma_{Y_2} =$ 10 MPa, $\rho_{Y_1,Y_2} = 0.5$), the external force F be an independent normal variable ($\mu_F = 5000$ N, $\sigma_F =$ 500 N), and the cross sectional areas A_1 and A_2 be respectively equal to 80 and 70 mm^2. Finally, the following system event is considered

$$E_{sys} = E_1 \cup E_2 = (g_1 \leq 0) \cup (g_2 \leq 0)$$
$$g_i(Y_i, F) = Y_i - F/A_i \quad , \quad i = 1,2 \tag{C.1}$$

Following the Monte Carlo procedure presented in Section 2.1.8, $P(E_{sys})$ is estimated by the empirical average of the indicator function $I(y_1, y_2, f)$, which is equal to 1 if the outcome (y_1, y_2, f) of the random vector (Y_1, Y_2, F) belongs to the failure domain, and 0 otherwise. In other words, $I(y_1, y_2, f)$ is equal to 1 if any of the following events is verified:

$$E_1 \cap \bar{E}_2 = \text{only the first component fails}$$
$$E_2 \cap \bar{E}_1 = \text{only the second component fails} \tag{C.2}$$
$$E_1 \cap E_2 = \text{both the components fail}$$

The union of the three basic events above is represented by the shaded area in Figure C.2, and it is equivalent to the system event defined in Eq. (C.1), i.e. $E_{sys} = E_1 \cup E_2$.

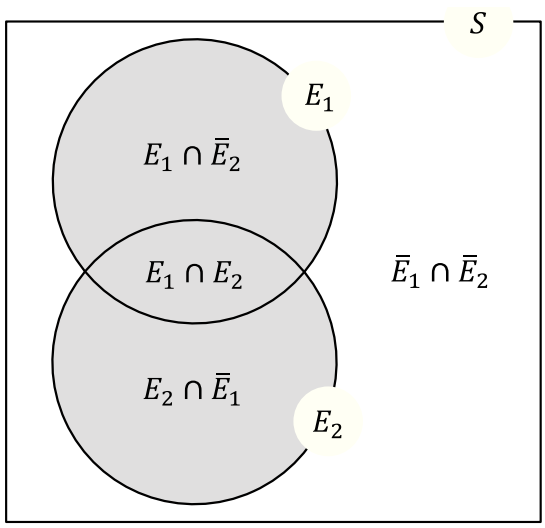

Figure C.2: Sample space S for the bicomponent system in Figure C.1.

After running $N = 6 \cdot 10^5$ analyses (the simulation terminates when $\mathrm{CoV} = 0.05$), the following frequencies are obtained by crude MCS,

$$\begin{aligned} P(E_1 \cap \bar{E}_2) &= 247/N = 4.1167 \cdot 10^{-4} \\ P(E_2 \cap \bar{E}_1) &= 5819/N = 9.6983 \cdot 10^{-3} \\ P(E_1 \cap E_2) &= 172/N = 2.8667 \cdot 10^{-4} \end{aligned} \tag{C.3}$$

Therefore,

$$\begin{aligned} P(E_{sys}) = P(E_1 \cup E_2) &= P(E_1 \cap \bar{E}_2) + P(E_2 \cap \bar{E}_1) + P(E_1 \cap E_2) \\ &= (247 + 5819 + 172)/N = 1.0397 \cdot 10^{-2} \end{aligned} \tag{C.4}$$

A post-processing of MCS results is then needed to find the failure probabilities of the dominant failure modes, i.e. $P(E_1)$ and $P(E_2)$. For this simple case study, the failure mode probabilities can be recovered from the total probability theorem (see Eq. (2.7)):

$$\begin{aligned} P(E_1) &= P(E_1|E_2)P(E_2) + P(E_1|\bar{E}_2)P(\bar{E}_2) \\ &= P(E_1 \cap E_2) + P(E_1 \cap \bar{E}_2) = 6.9833 \cdot 10^{-4} \end{aligned} \tag{C.5}$$

$$\begin{aligned} P(E_2) &= P(E_2|E_1)P(E_1) + P(E_2|\bar{E}_1)P(\bar{E}_1) \\ &= P(E_2 \cap E_1) + P(E_2 \cap \bar{E}_1) = 9.9850 \cdot 10^{-3} \end{aligned} \tag{C.6}$$

However, in general system reliability problems, more than two failure modes are involved, and the amount of data provided by MCS is not enough to calculate the total probability of the identified failure modes. Therefore, a second MCS analysis must be

performed, in which the indicator function of a given failure mode is set equal to 1 even if a different mode occurs, as long as this mode contains the first one. Hence, with reference to the previous case study, the frequency of event E_1 is updated if any of the following events is verified:

$$\begin{aligned} &E_1 \cap \bar{E}_2 = \text{only the first component fails} \\ &E_1 \cap E_2 = \text{both the components fail} \end{aligned} \tag{C.7}$$

Analogously, the frequency of event E_2 is updated when any of the following events occurs:

$$\begin{aligned} &E_2 \cap \bar{E}_1 = \text{only the second component fails} \\ &E_1 \cap E_2 = \text{both the components fail} \end{aligned} \tag{C.8}$$

In this way, the total probabilities in Eqs. (C.5) and (C.6) can be estimated directly by MCS. As in the case of the system event, the convergence to the exact values of $P(E_1)$ and $P(E_2)$ is here assumed when the CoVs of both the estimates reach the target value of 0.05. The convergence process requires $N_1 = 4.2 \cdot 10^6$ analyses for $P(E_1)$ and $N_2 = 8 \cdot 10^5$ analyses for $P(E_2)$, and the corresponding frequencies are reported below:

$$\begin{aligned} P(E_1) &= P(E_1 \cap E_2) + P(E_1 \cap \bar{E}_2) \\ &= (1345 + 1627)/N_1 = 7.0762 \cdot 10^{-4} \end{aligned} \tag{C.9}$$

$$\begin{aligned} P(E_2) &= P(E_2 \cap E_1) + P(E_2 \cap \bar{E}_1) \\ &= (275 + 7915)/N_2 = 1.0238 \cdot 10^{-2} \end{aligned} \tag{C.10}$$

These estimates are more accurate than those obtained in Eqs. (C.5) and (C.6) using the total probability theorem (which can only be used for bicomponent systems). This result is due to the convergence process of the second MCS analysis, which considers the CoVs of $P(E_1)$ and $P(E_2)$ rather than the CoV of $P(E_{sys})$.

Appendix D:
Derivation of the hierarchical scaling law

As illustrated in Figure D.1, the control region (of length $l_c^{[1]}$) is partitioned into 4 segments (A_1, A_2, B_1 and B_2) of equal length $l_e^{[0]} = l_c^{[1]}/2$, and the first fibre break is supposed to occur in the middle of segment A_1.

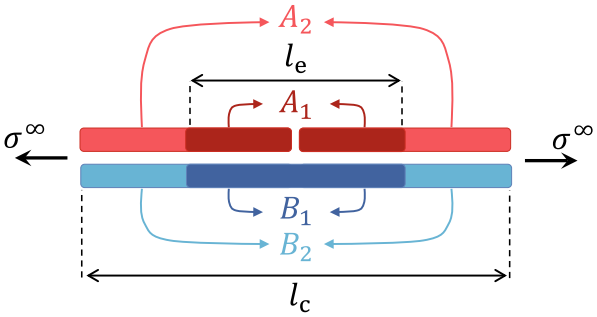

Figure D.1: Definition of fibre segments in a level-[1] bundle (Pimenta & Pinho, 2013).

The hierarchical scaling law presented in (Pimenta & Pinho, 2013) is derived using the following definition of the system failure event:

$$E_{sys} = E_1 \cup E_2 \cup E_3 \tag{D.1}$$

where E_1, E_2 and E_3 are the failure modes introduced in Section 4.2.1. This system event assumes the weakest segment is A_1, which represents only $1/4$ of the cases. Therefore, the bundle strength is given by

$$F_{U,c}^{[1]}(\sigma^\infty) = 4 \cdot [P(E_1) + P(E_2) + P(E_3)] \tag{D.2}$$

where E_1, E_2 and E_3 are assumed independent from each other. Eq. (4.7) is then recovered from the complement of Eq. (D.2), i.e. $S_{U,c}^{[1]}(\sigma^\infty) = 1 - F_{U,c}^{[1]}(\sigma^\infty)$.

In this appendix, a simpler approach is presented for the derivation of Eq. (4.7), in which the sequences of events E_1, E_2 and E_3 leading to bundle failure are reformulated in terms of safety events. Let $X_{U,e}$ and $X_{K,e}$ be the segment strengths under uniform stresses and linear stress concentrations, respectively. Then, a level-[1] bundle of length $l_c^{[1]}$ survives the remote stress if

(*i*) all the 4 segments survive the uniform stress σ^{∞}:

$$E_i = \left(X_{\mathrm{U,e}}^{A_1} > \sigma^{\infty}\right) \cap \left(X_{\mathrm{U,e}}^{A_2} > \sigma^{\infty}\right) \cap \left(X_{\mathrm{U,e}}^{A_3} > \sigma^{\infty}\right) \cap \left(X_{\mathrm{U,e}}^{A_4} > \sigma^{\infty}\right) \tag{D.3}$$

(*ii*) the weakest fibre (e.g., A) fails under σ^{∞} and the strongest fibre survives the resulting stress fields (one segment under uniform stress, and another segment under linear stress concentration):

$$E_{ii} = \left(X_{\mathrm{U,c}}^{A} \le \sigma^{\infty}\right) \cap \left(X_{\mathrm{U,e}}^{B_1 \; or \; B_2} > \sigma^{\infty}\right) \cap \left(X_{\mathrm{K,e}}^{B_2 \; or \; B_1} > \sigma^{\infty}\right) \tag{D.4}$$

The safety event E_{ii} must be counted twice to consider the case when B is the weakest fibre. Therefore, the survival probability of the level-[1] bundle is calculated as

$$S_{\mathrm{U,c}}^{[1]}(\sigma^{\infty}) = P(E_i) + 2 \cdot P(E_{ii}) \tag{D.5}$$

Since the random strengths are assumed statistically identical and independent, the following simplifications are obtained

$$P(E_i) = \left[P\left(X_{\mathrm{U,e}} > \sigma^{\infty}\right)\right]^4 = S_{\mathrm{U,e}}^{[0]}(\sigma^{\infty})^4 \tag{D.6}$$

$$\begin{aligned} P(E_{ii}) &= 2 \cdot P\left(X_{U,c} \le \sigma^{\infty}\right) \cdot P\left(X_{U,\mathrm{e}} > \sigma^{\infty}\right) \cdot P\left(X_{\mathrm{K,e}} > \sigma^{\infty}\right) \\ &= 2 \cdot \left[1 - S_{\mathrm{U,c}}^{[0]}(\sigma^{\infty})\right] \cdot S_{\mathrm{U,e}}^{[0]}(\sigma^{\infty}) \cdot S_{\mathrm{K,e}}^{[0]}(\sigma^{\infty}) \end{aligned} \tag{D.7}$$

The WLT in Eq. (4.11) is then used to scale $S_{\mathrm{U,c}}^{[0]}$ to the recovery length $l_{\mathrm{e}}^{[0]}$, so that Eq. (D.7) can be rewritten as

$$P(E_{ii}) = 2 \cdot \left[1 - S_{\mathrm{U,e}}^{[0]}(\sigma^{\infty})^2\right] \cdot S_{\mathrm{U,e}}^{[0]}(\sigma^{\infty}) \cdot S_{\mathrm{K,e}}^{[0]}(\sigma^{\infty}) \tag{D.8}$$

Finally, the hierarchical scaling law obtained by introducing Eqs. (D.6) and (D.8) into Eq. (D.5).